

The FCC-ee interaction region, design and integration of the machine elements and detectors, machine induced backgrounds and key performance indicators

Manuela Boscolo^{*1}, Fabrizio Palla^{*2}, Gherardo Ammirabile², Kevin D. J. Andre³, Giorgio Baldinelli⁴, Patricia Borges de Sousa³, Filippo Bosi², Giacomo Broggi^{1,3,5}, Roderik Bruce³, Helmut Burkhardt^{3,6}, Marco Calviani³, Silvio Candido³, Andrea Ciarma¹, Mogens Dam⁷, Brieuc Francois³, Rui Franqueira Ximenes³, Francesco Franesini¹, Alessandro Frasca^{3,8}, Andrea Gaddi³, Armin Ilg⁹, Robert Kieffer³, Michael Koratzinos¹⁰, Stefano Lauciani¹, Anton Lechner³, Giuseppe Lerner³, Giulia Nigrelli^{1,3,5}, Alexander Novokhatski¹¹, Katsunobu Oide¹², Antonio Perillo-Marcone³, Brett Parker¹³, Pantaleo Raimondi¹⁴, John T. Seeman¹¹, Cristiano Turrioni⁴, Leonard Watrelot³, Frank Zimmermann³.

¹ INFN, Laboratori Nazionali di Frascati, Italy

² INFN, Sezione di Pisa, Italy

³ CERN, Switzerland

⁴ INFN, Sezione di Perugia, Italy

⁵ University of Rome "Sapienza", Italy

⁶ University of Freiburg, Germany

⁷ Niels Bohr Institute, Denmark

⁸ University of Liverpool, UK

⁹ University of Zurich, Switzerland

¹⁰ Paul Scherrer Institute, Switzerland

¹¹ SLAC, USA

¹² University of Geneva, Switzerland

¹³ Brookhaven National Laboratory, USA

¹⁴ Fermilab National Laboratory, USA

*Corresponding authors: Manuela.Boscolo@cern.ch and Fabrizio.Palla@cern.ch

This work was partially supported by the EC HORIZON 2020 project FCC-IS, grant agreement No. 951754.

This report should be cited as:

Manuela Boscolo et al., *"The FCC-ee interaction region, design and integration of the machine elements and detectors, machine induced backgrounds and key performance indicators"*, CERN (2025), <https://doi.org/10.17181/w4kws-rne05>, edited by Manuela Boscolo and Fabrizio Palla.

This report was edited with the Overleaf.com collaborative writing and publishing system. Type-setting and final print preparation was performed using pdfTeX 3.14159265-2.6-1.40.17

March 24th, 2025

Contents

1	Interaction region overview and requirements	1
2	Interaction region optics design	2
2.1	Solenoid compensation scheme	3
2.2	IR magnet system	5
3	Central MDI region engineering design	6
3.1	Mechanical model of the beam pipe	6
3.2	IR bellows	9
3.3	Remote vacuum connection	10
3.4	Vertex Detector	10
3.5	Luminosity Calorimeter	19
3.6	Optimisation of the beam pipe material budget	22
4	Integration of the Interaction Region	24
4.1	Support tube	24
4.2	Alignment strategy	26
4.3	Global detector maintenance and opening	31
5	Simulation of the vertex detector and machine elements	34
5.1	Geometry description of the MDI region in Key4hep	34
5.2	Baseline vertex detector simulation model	36
6	Beam-induced backgrounds	37
6.1	Synchrotron Radiation backgrounds	38
6.2	Beam halo losses	39
6.3	Beam gas scattering	40
6.4	Thermal photons	41
6.5	Fast Instability	42
6.6	Injection backgrounds	45
6.7	Radiative Bhabha events	47
6.8	Beamstrahlung	47
6.9	Incoherent pairs creation	50
7	Radiation levels and energy deposition	53
7.1	Final focus quadrupoles energy deposition	53
7.2	Beamstrahlung dump	55
7.3	Radiation levels within the tunnel	56
7.4	Radiation levels in the detector	58
	References	66

This note gives an overview of the Machine Detector Interface (MDI) design performed for the Feasibility Study of the FCC-ee. A general overview of the FCC-ee interaction region (IR) is given in Section 1, where the main requirements are discussed. The IR optics design, as far as the magnetic configuration and compensation scheme is given in Section 2. The mechanical description of the FCC-ee interaction region layout is discussed in Section 3, followed by the description of its mechanical integration and alignment in Section 4. Section 5 describes the simulation framework of the machine elements and the vertex detector. Finally, the effects of the machine induced backgrounds, which have implications on the design and requirements on the electronics and detector technology, are discussed in Sections 6 and 7. Some of the material presented here can also be found in the published paper [1], although in this note a more detailed and updated description is presented.

1 Interaction region overview and requirements

The FCC-ee interaction region is designed to reach the highest luminosities at all centre-of-mass energies, from the Z pole to the $t\bar{t}$ threshold. This design is based on the crab-waist collision scheme, with nano-beams at the interaction point (IP), large horizontal crossing angle, and crab-waist sextupoles [2]. The MDI of FCC-ee has a compact and complex design [3, 4] that fulfils constraints imposed by the machine [3] and detector requirements.

The main beam parameters are recalled in Table 1, for the four main operational centre-of-mass energies. In FCC-ee, the two beams circulate in different vacuum chambers, which merge at 1.3 m from the IP. The distance between the face of the first superconducting final focus quadrupole (FFQ) and the IP (ℓ^*) is 2.2 m, well inside the detector volume. In addition to the optics constraints on the IR layout, physics considerations strongly advocate for hermetic detectors and for constraining the accelerator components within a cone of 100 mrad from the IP, along the z axis¹. These requirements demand a compact MDI design with tight space constraints.

Table 1: Key collider parameters for the FCC-ee IRs with 4 IPs [3] for the GHC lattice. The bunch length, σ_z , is different for non-colliding bunches (determined by ‘synchrotron radiation’, SR) and colliding bunches (determined by ‘beamstrahlung’, BS); σ_x^* and σ_y^* denote the bunch sizes at the IP in the (horizontal and vertical, respectively) transverse directions, while σ_δ is the relative beam energy spread.

	Z	W^+W^-	ZH	$t\bar{t}$
Beam energy (GeV)	45.6	80	120	182.5
Luminosity / IP ($10^{34} \text{ cm}^{-2}\text{s}^{-1}$)	144	20	7.5	1.45
Beam current (mA)	1 292	135	26.8	5.0
Colliding bunches / beam	11 200	1 852	300	60
Bunch spacing (ns)	27	163	1 008	4 725
σ_x^* (μm)	8.84	21.8	12.6	36.9
σ_y^* (nm)	38.1	44.7	31.6	43.0
σ_z (mm) SR / BS	5.15 / 15.2	3.46 / 5.28	3.26 / 5.59	1.91 / 2.34
σ_δ (%) SR / BS	0.039 / 0.115	0.069 / 0.105	0.102 / 0.176	0.152 / 0.186

The crab-waist scheme requires a large horizontal crossing angle of 30 mrad. The incoming beams point straight to the IP, while the outgoing beam trajectories are strongly bent from the IP, so that the beams can successfully merge back close to the opposite ring [5]. This scheme ensures that most of the synchrotron radiation (SR) generated at the IR magnetic elements does not strike the IR central beam

¹The coordinate system of the detector has the origin centred at the nominal collision point. The z axis is defined as the bisector of the axes of the incoming and outgoing beams, ideally in the direction of the axis of the experiment solenoid. The x axis is in the plane subtended by the two beams and pointing away from the centre of FCC. In this way, the positron beam is travelling towards positive values of z (mainly) and x (subordinately). Perpendicular to the (x, z) -plane, the y axis points upwards. The polar angle, θ , is then measured with respect to the z axis and the azimuthal angle, ϕ , with respect to the x axis in the (x, y) plane. The radial coordinate, $r = \sqrt{x^2 + y^2}$, is the distance from the z axis.

pipe. The intense radiation emitted during the collision in the electromagnetic field of the opposite beam, known as beamstrahlung (BS), is mostly collinear with the outgoing beams, similarly to the SR [6]. Both the BS and SR photons are stopped at about 500 m downstream of the IP, in dedicated dumps [7]. To minimise the level of SR photons that reach the detectors, the closest bending magnet is located at more than 100 m from the IP and those located up to 500 m have a SR critical energy below 100 keV.

To counteract the beam rotation and deflection that would be caused by the simultaneous effects of the detector magnetic field of 2 T and the crossing angle, a compensating solenoid delivering a magnetic field of -5 T is placed at 1.23 m from the IP, cancelling out the longitudinal magnetic field integral along the z axis from the last focusing quadrupole to the IP. Consequently, the front face of the luminosity calorimeter (LumiCal), placed in front of the compensating solenoid, is only 1 m from the IP. The LumiCal is centred around the outgoing beam direction and measures the integrated luminosity from the rate of low-angle Bhabha events, $e^+e^- \rightarrow e^+e^-$. The first layer of the vertex detector must be placed as close as possible to the IP to optimise the precision of the primary and secondary vertex position determination, with direct impact on the efficiency and purity of flavour tagging algorithms. The smallest affordable distance is set by the central beam pipe radius of 1 cm. The length of the vertex detector (1.86 m) is chosen to cover the angular region $|\cos \theta| < 0.99$. A lightweight mechanical structure is designed for its support. To avoid any material in front of the LumiCal, all other detector elements must be placed above 110 mrad with respect to the z axis.

An overall design of the interaction region is shown in Fig. 1. The next sections describe the main features of the MDI.

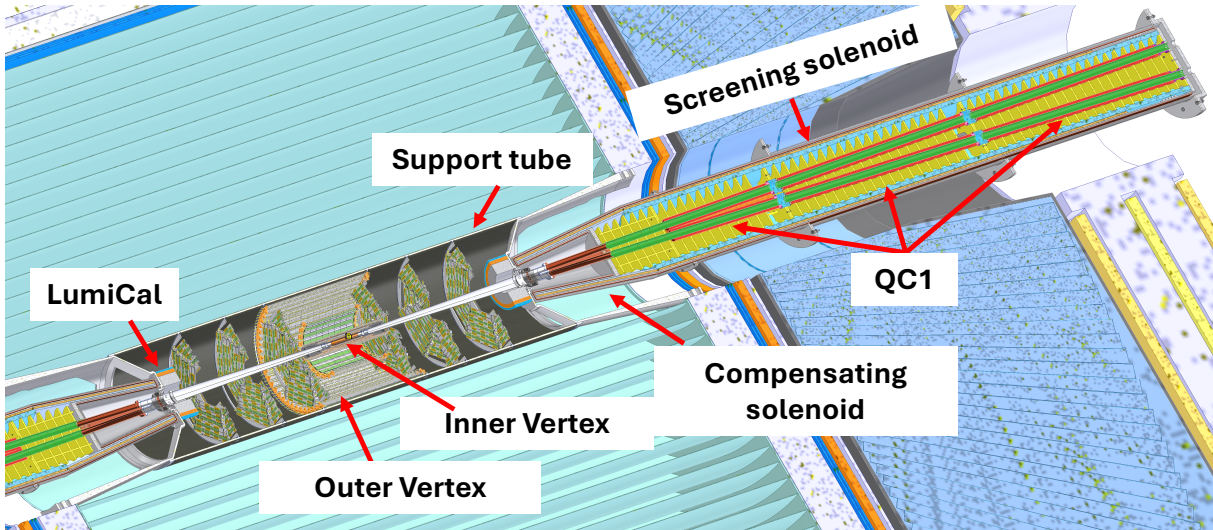


Fig. 1: Layout of the interaction region. The support tube allows the integration of the luminosity calorimeter (LumiCal) and the vertex detector. The three segments of the final focus quadrupoles (QC1) are shown with the screening and compensating solenoids.

2 Interaction region optics design

Two competing designs are under consideration for the IR optics. An asymmetric optics design, named Global Hybrid chromaticity Correction (GHC) [8], featuring virtual crab sextupoles by detuning the local vertical chromatic correction, comprises a minimum number of sextupoles. An alternative more symmetric design, named Local Chromatic Correction (LCC) optics [9], features modular horizontal and vertical chromatic correction sections and independent crab sextupoles.

The beam lines in the interaction region are separated for the two beams and there are no common quadrupoles in the IR. The final focus quadrupoles, QC1 and QC2, are modeled in two or three segments

to allow for the required flexibility in the beam energy, their field strength is in any case below 100 T/m.

The small $\beta_{x,y}^*$ necessary to reach the unprecedented high luminosities are obtained with the two FFQs comprised within 10 m from the IP, and with a distance of about 0.3 m between them. The current optics design is not compatible with two separate cryostats for QC1 and QC2, as it will be discussed in Sec. 2.2, hence giving a strong requirement on its design that will be addressed in the next phase.

The detector solenoid compensation optics is relevant for the design of the MDI region, as it defines the set of IR magnets, and the current status of the study is discussed in the next section.

2.1 Solenoid compensation scheme

The detector solenoidal field, that extends in the region of the FFQs and beyond, can significantly affect the IP beam size due to coupling and beam optics distortions.

At FCC-ee, compensating solenoids and skew quadrupoles are employed to correct the coupling and maintain a small beam size at the IP, the first ones cancel the $\int B_z dz$, while the latter provide additional fine-tuning of the beam optics. In addition, screening solenoids around the portion of the FFQ inside the detector shields the detector solenoidal field for the circulating beams.

Two compensating schemes are being studied, and are sketched on top of Fig. 2. The first one, also known as *local-scheme*, represents the baseline option. It is based on a strong "compensating" antisolenoid, 0.77 m long with a field of 5 T opposite to the solenoidal one, at $|z| = 1.23$ m in front of the first FFQ from the IP [10]. In the second scheme, named *non-local-scheme*, the antisolenoids are placed beyond the FFQs, outside of the detector region, as described in [11]. The performance studies have been conducted using MAD-X and SAD. As it is non-trivial to use the same lattices with the two codes, the two concepts have been independently developed and analysed with MAD-X and SAD, finding comparable results. The optics model developed in MAD-X is based on the LLC optics.

The choice of the solenoid compensation scheme has direct implications on the maximum allowed detector solenoidal field, as well as on the transverse polarization of the beam.

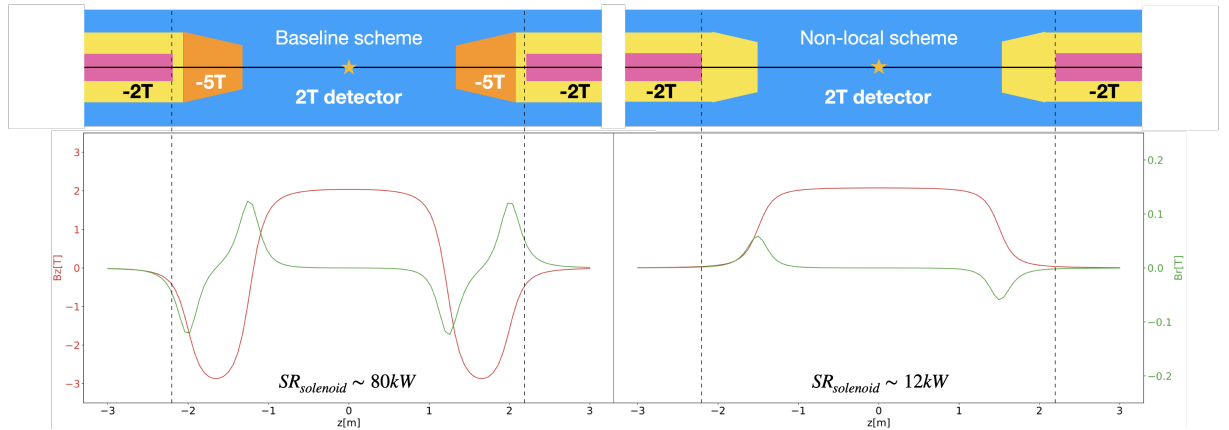


Fig. 2: Conceptual sketch of the IR, ± 3 m from the IP, with the 2 T detector field in blue, FFQ in pink, compensating solenoid in orange, and -2 T screening solenoid in yellow, for the baseline (*local-scheme*) (top left) and for the *non-local-scheme* (top right). In the bottom plots the corresponding longitudinal (red) and radial (green) magnetic field profiles along the 15 mrad axis in the IR.

The *non-local* solenoid compensation scheme uses weak IR correctors to close the orbit and small skew quadrupolar components winded around the FFQs, together with an anti-solenoid just outside the final focus quadrupoles to correct for coupling effects. The skew quadrupole components around the FFQs provide for the rotation of the beam reference axis induced by the experiment solenoidal field. The detector solenoid field at the FFQs quadrupoles is cancelled using a "screening solenoid"; its optimal

position must be as close as possible to the IP, so it starts at the end of the bellows, at about $|z| = 1.23$ m from the IP. The anti-solenoid solenoids are placed in the drift sections, before the first dipoles, at about 11 m from the IP. They are aligned with the beam such that their contribution to synchrotron radiation and emittance increase becomes negligible. In addition the space available in this region could be used to increase their length and lower the fields achieving the same compensation of $\int B_z dz$. Weak horizontal and vertical correctors in the IR are used to close the orbit bumps.

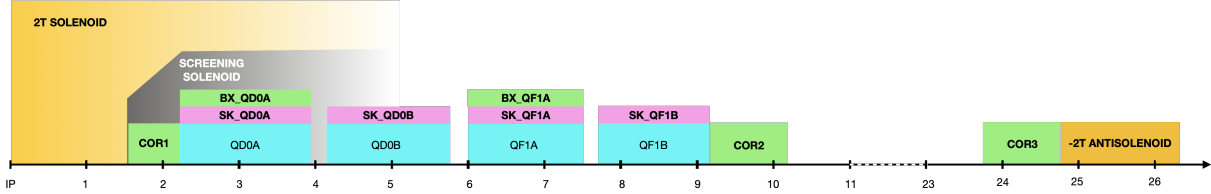


Fig. 3: Layout of the non-local solenoid compensation scheme for LCCO lattice v92.

The orbit bumps are shown in Fig. 4, with a vertical orbit bump of < 0.2 mm.

The residual beam coupling is evaluated from the vertical emittance growth calculated directly using synchrotron radiation integrals, and the most recent studies have shown a value of ≤ 100 fm.

Chromatic effects have been studied in an energy off-set up to $dE/E = \pm 4\%$ for the LCC optics at Z-pole and compared for the two compensating schemes, showing a smaller vertical emittance increase for the non-local scheme. Based on first estimates, depolarizing effects appear to be small, to be confirmed by more complete simulation.

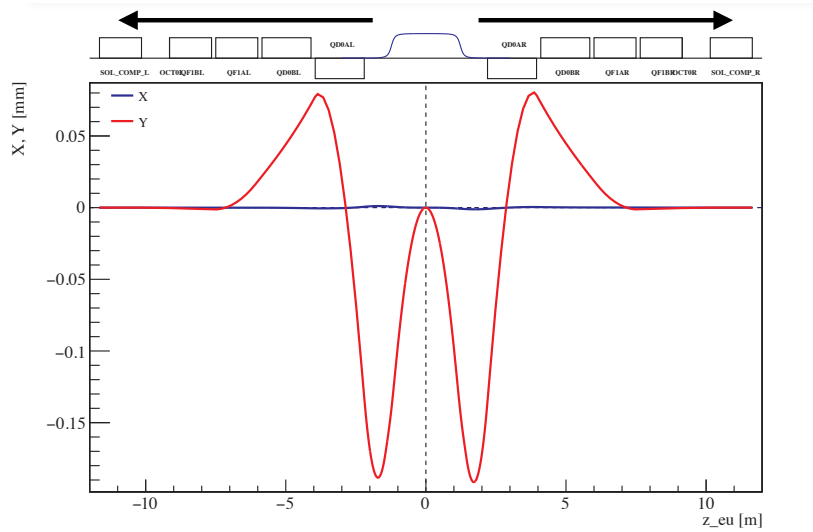


Fig. 4: Horizontal (blue) and vertical (red) orbit bump for the non-local compensation scheme. The arrows illustrate the change of position of the anti-solenoids that are now moved just outside the final-focus quadrupole region.

The different location of the anti-solenoids in the *non-local* scheme, largely reduces the amount of SR generated inside the detector, between ± 3 m from the IP. In fact, the nearly 80 kW of SR generated in the *local-scheme* are reduced to about 40 kW (~ 12 kW from the solenoid, remainder from closing the bump) for the *non-local* case. Off-momentum particle losses in the FFQ region are also expected to be reduced in this scheme.

A relevant benefit coming from an improved coupling compensation is the possibility to increase the detector solenoidal field. The possibility of an increase to a 3 T detector solenoid field has been

studied with the *non-local* scheme. As the SR generation increases proportionally to the second power of the magnetic field, it is expected to become about 90 kW for the *non-local* and as high as 180 kW for the *local-scheme*. These values have also been confirmed by simulations. The IR correctors used for the orbit and dispersion bumps, scale linearly with the detector field, remaining at acceptable values.

The optics design will continue and be finalised in the next phase of the study, to advance the engineering design of the IR magnet system, whose initial considerations are outlined in the following section.

2.2 IR magnet system

The IR magnet system includes the FFQs, the compensating and screening solenoids, the skew quadrupoles, and corrector magnets.

The FFQs design is presently based on the canted coil. A prototype conductor-in-grooves of one segment of the first final focus quadrupole was fabricated, and cold tests have been successfully performed and are presented in [12]. The IR corrector magnets are being proposed to use the BNL direct-wind method [13], successfully implemented at SuperKEKB [14]. This technology, among other advantages, optimizes space and improves field quality.

The energy deposition from beam interactions, particularly radiative Bhabha scattering, poses a risk to superconducting coils. To mitigate this, water-cooled beam pipes inside the cryostat and after the vacuum flange should be employed to handle high-energy deposition zones nearby QC1; intermediate temperature heavy metal absorbers can be integrated to reduce radiation impact on superconducting elements.

Separate cryostats for QC1 and QC2 with integrated raft allow for better spacing of cryogenic components, leads, and supports, and is the preferred configuration. Two separate cryostats will also allow for two BPMS outside the cold volume, attached to the warm beam pipe. The first one will be placed between the LumiCal and QC1. Its location demands for special care for minimising the heat load due to impedance, as described in Ref. [15]. The second one will be placed outside the second cryostat, next to QC2. We note that a single cryostat housing both final quadrupoles QC1 and QC2 would simplify the structural integration but would also pose problems in the detector opening, and the long length also has a problem in cantilever stability.

The cooling strategy depends on the total heat load to be extracted. While an estimate of the heat load produced by radiative Bhabha has been performed (see Sec. 7.1), the heat load from the wakefields and trapped modes needs to be consolidated with the latest beam parameters and evaluated at all beam energies, as well as for the synchrotron radiation that can be deposited in this area. This study will give the indication at what operating temperature the system should function.

As a general consideration, the IR magnets should share a common temperature level to reduce system complexity and to optimise efficiency. The proposed cooling temperatures range from 1.9-2.1 K for the pressurised Helium II (He II), 4.5 K for the supercritical Helium (He), or 10-20 K for forced Helium gas flow. A preliminary assessment of local heat extraction for QC1 magnets indicates that all these operating temperatures are technically feasible.

The pressurised Helium II at 1.9 K provides extremely low vibration levels and high heat extraction efficiency, but it requires a large helium cross-section and underground cryoplant infrastructure, and has a high power consumption. Even with high-temperature superconductors, this temperature may still be the preferred choice due to its superior heat extraction capabilities.

The supercritical Helium at 4.5 K is compatible with detector cryoplant, with the advantage of minimising additional infrastructure. It has a moderate temperature gradient, between 0.5 and 1 K along the cold mass. This approach provides a lower power consumption than Helium II, balancing efficiency with integration feasibility.

The third possibility of a forced Helium flow between 10 and 20 K has the lowest power consumption with compact distribution lines, at the expenses of the highest thermal gradients, in the range of 5-10 K, and potential vibrations.

Two tentative designs have been proposed for the radial build of the QC1 assembly. The first option is with a common Helium space for all magnets, quadrupoles and solenoids, with vacuum insulation and thermal shielding integrated into the cryostat. The second option is with independent helium regions for quadrupole and solenoids, with vacuum insulation and thermal shielding separating the two sections. The first option is efficient but requires precise control of the helium circulation, the second option provides an enhanced isolation but increases system complexity.

In the next phase of design the possibility of sharing the IR magnet cryogenics the same cryoplant of the detector will be considered, together with a study whether there is allocated tunnel space sufficient for a cryogenic distribution line.

3 Central MDI region engineering design

This section provides an overview of the engineered design for the elements shown in Fig. 5, which represents the very central region, between ± 1.2 m from the IP.

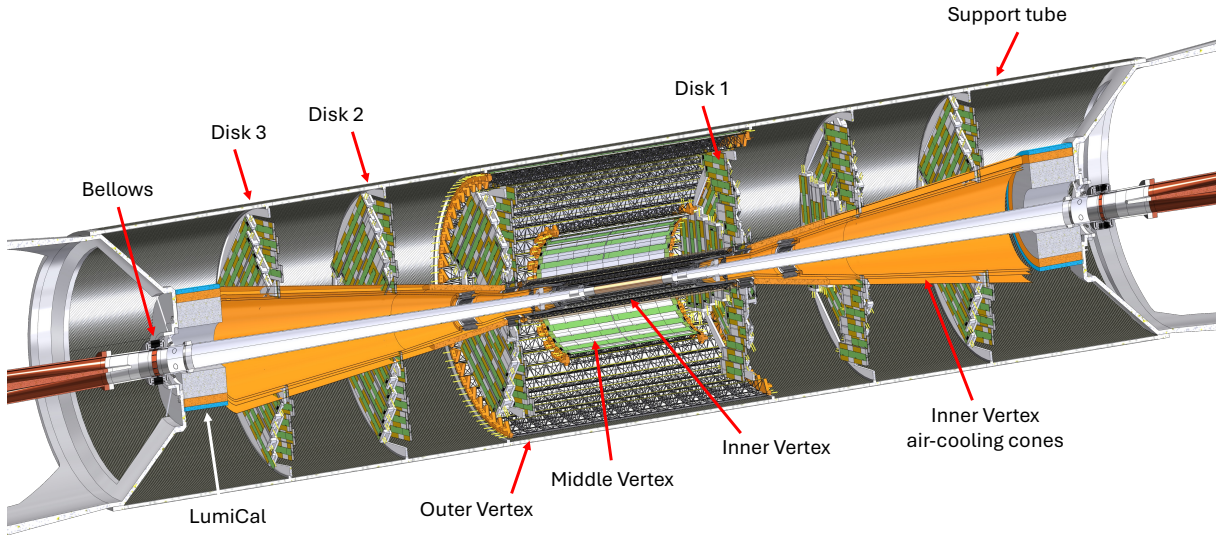


Fig. 5: Section of the MDI CAD model for about ± 1.2 m from the IP for the IDEA detector. The beam pipe, the luminosity monitor, the vertex and outer trackers, will all be supported by the support tube shown here with its endcaps.

3.1 Mechanical model of the beam pipe

The mechanical model of the IR beam pipe has to fulfill conflicting requirements. It must have a smooth shape to provide low beam impedance; it has to be as thin as possible to minimise the material budget as required by the physics performance, and at the same time be rigid enough to resist mechanical stresses. In addition, at the Z pole, the large heat load due by the beam heat loads due to the wakefields and the possible synchrotron radiation losses, require an active cooling.

The central beam pipe is a 18 cm long cylinder, with a double layer wall structure, as displayed in Fig. 6, resulting in a channel for the flow of liquid paraffin coolant, whose characteristics are reported in Table 4.

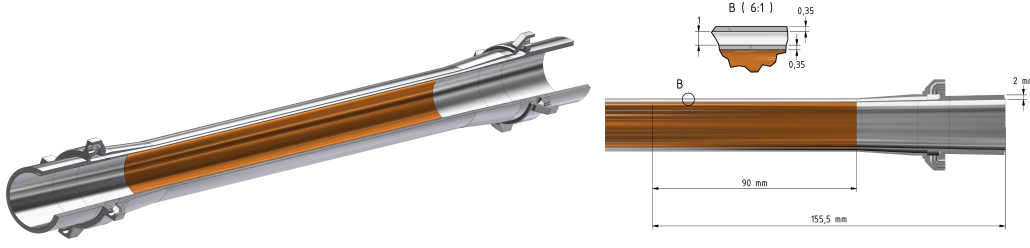


Fig. 6: Left: The central chamber in AlBeMet162 with its cooling inlets and outlets, and its internal gold coating layer. Right: Chamber cross section and zoom on the cooling channel for the paraffin flow.

The double layer structure is composed of two concentric cylinders of AlBeMet², chosen for its good mechanical properties, each one with a thickness of 0.35 mm and assembled with 1 mm gap for the paraffin flow, thus bringing its external diameter to 23.4 mm. An internal 5 μm coating layer of gold ensures a good electrical conductivity to minimise the beam heat load [16] and to shield the vertex detector from residual high energy SR photons. Table 2 reports the detailed composition and thickness. The geometry is optimized to minimise the material budget, provide mechanical stability, and to guarantee a proper coolant flow to remove the heat load.

Table 2: Composition of the central beam pipe.

Layer	Thickness [mm]	X/X0[%]
Internal gold	0.005	0.15
Inner AlBeMet layer	0.35	0.14
Liquid paraffin	1	0.18
Outer AlBeMet layer	0.35	0.14
Total	1.705	0.61

The ellipito-conical vacuum chamber, also made in AlBeMet and extending from 90 mm from the IP until the bellows, is shown in Fig. 7. After a short transition from the central chamber, the thickness of the walls remain at a constant value of 2 mm. The cooling of the chamber is guaranteed by water flowing channels welded directly on the chamber itself. To minimise the impact on the luminosity calorimeter the cooling channels on the beam pipe are asymmetrical, and shaped as to be below of a cone of 50 mrad with respect to the direction of the outgoing beam, as shown in Fig. 7.

²AlBeMet162 is an alloy of commercially pure beryllium and aluminium, 62 % and 38 % in weight, respectively, whose properties are listed in Table 3.

Table 3: Properties of AlBeMet162, that contains 62 wt% commercially pure beryllium and 38 wt% commercially pure aluminum.

Property	Value	Unit
Density	2.10	g/cm^3
Modulus	193	GPa
Poisson's ratio	0.17	
CTE 25°C	13.9	$\text{ppm}/^\circ\text{C}$
Thermal conductivity	210	W/m K
Specific Heat 20°C	1465	J/kgK
Electrical Conductivity 20 °C	49	% IACS
Fracture Toughness K_{1c}	11-23	$\text{MPa } \sqrt{\text{m}}$

Table 4: Liquid paraffin ($C_{10}H_{22}$) physical properties.

Property	Value
Density 25°C	0.734 g/cm ³
Specific Heat	2.21 J/gK
Thermal conductivity	0.34 W/m °C
Kinematic viscosity	1.1 mm ² /s
Dynamic viscosity	0.92 mPa·s
Melting point	-27.9 °C
Boiling point	174.1 °C
Auto-ignition temperature	210 °C
Flash point	51 °C

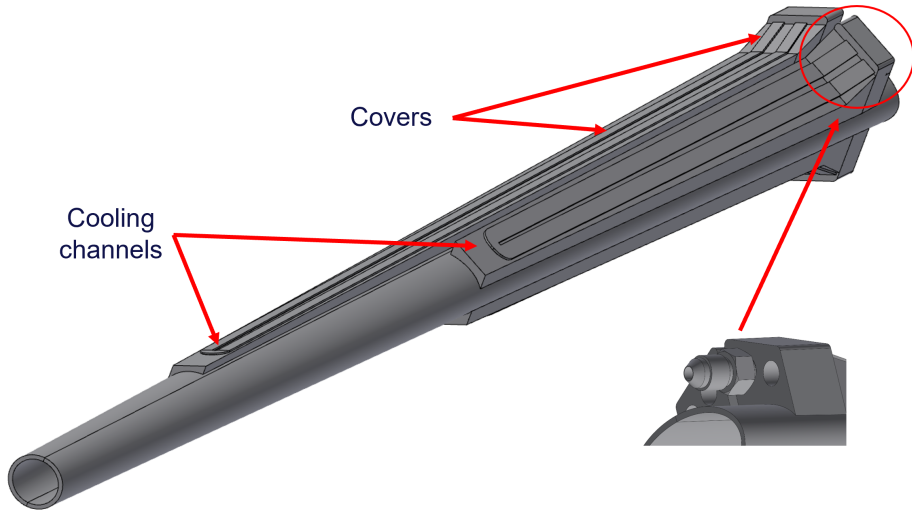


Fig. 7: AlBeMet162 vacuum chamber from 90 mm from the IP to the bellows, named conical chamber for its shape, with asymmetrical cooling channels.

The ellipto-conical chamber bifurcates into two symmetrical beam pipes of 15 mm radius at 1.28 m from the IP. This point is also known as *crotch*. The impedance was minimised by carefully designing the smooth transition from the circular shape of the central beam pipe to an elliptical shape for the lateral one, as discussed in Ref. [17]; in addition, the crotch shape has been carefully studied in order to minimise the effects of the wakefields and high-order modes.

A thermo-structural analysis has been performed to calculate the temperature distribution, stress, strain and displacement, using as input the characteristics for paraffin and water flow reported in Table 5, in the hypothesis of a deposited power of 54 W over the central chamber and 130 W over the conical one, assuming a perfect thermal contact between the materials, and initial beam pipes temperatures of 20 °C. The structural analysis has been performed considering the cantilevered-simply configuration.

The resulting temperature distribution for the two chambers is shown in Fig. 8. The highest temperature of the central chamber is expected to reach 29 °C, and 50 °C for the ellipto-conical chamber, with a temperature increase of 2.5 °C and 2° C for the paraffin and water, respectively.

The structural analysis takes in account the effects of the earth gravity, the vacuum load, the weight of the inner vertex detector that is anchored to the ellipto-conical chamber, together with the resulting temperature distribution from the thermal simulation. The results are summarised in Table 6. The maximum stress is ten times lower than the AlBeMet162 yield strength (193 MPa), and the maximum displacement is acceptable. The buckling behaviour is more critical than the static one, therefore some

Table 5: Cooling system boundary conditions, used as input for the thermo-structural analysis of the vacuum chamber.

	Paraffin	Water
Flow rate [kg/s]	0.015	0.01
Section [mm ²]	68.17	12.25
Velocity [m/s]	0.3	1
Inlet temperature [°C]	18	16
Convective coefficient[W/m ² K]	900	1200

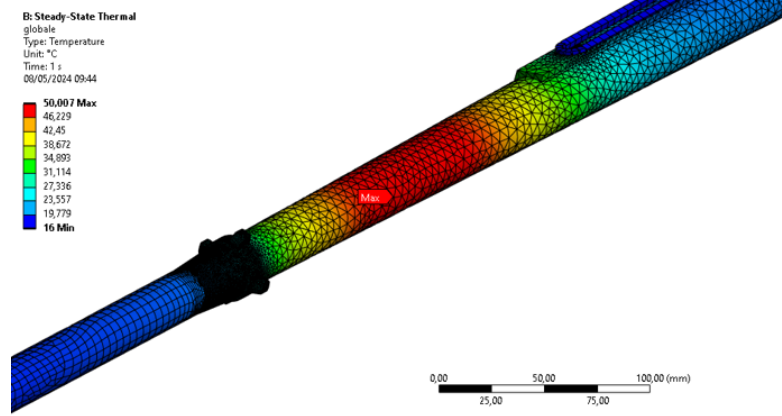


Fig. 8: ANSYS [18] simulation of the temperature distribution along the conical chamber for about 50 W of deposited power over the central chamber and 130 W over the conical chamber.

experimental tests are in progress to benchmark these results.

The cooling system can tolerate an increase of about 15% of heat load, by adapting the flow rate of the coolant without compromising the mechanical stability.

Table 6: Structural analysis results. See text for explanation.

Case	Max Von Mises [MPa]	Max displacement [mm]
Cantilevered, simply supported	20	0.5

3.2 IR bellows

The design of the IR bellows is inspired to the ones developed and successfully implemented in the ESRF-EBS storage ring [19]. The continuity of the beam pipe is restored by electrically shielding the bellows with RF fingers made of copper-beryllium (CuBe₂) blades lying around the elliptical shape of vacuum chamber and the desired electrical contact is obtained by a blade pusher.

The bellows will be attached on one side to the conical chamber and on the other side to the remote vacuum flange, close to the superconducting IR magnet system. The bellows have to be as compact as possible, due to the limited space available in that area, with the function to absorb chamber-to-chamber misalignment and to compensate for thermal expansion.

From the study of the electromagnetic interactions of the bellows with the beam [15] it has emerged the needs of Higher Order Modes (HOM) absorbers to be put inside and a cooling system to remove it at the Z pole, as shown in Fig. 9.

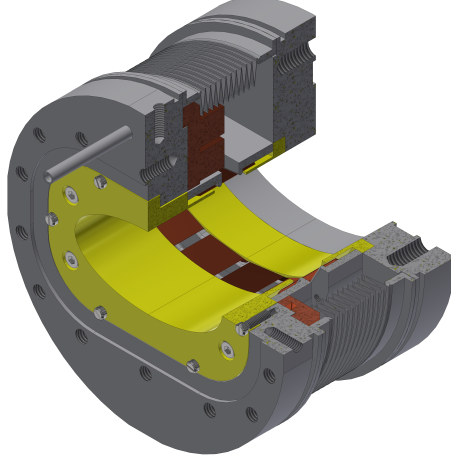


Fig. 9: Proposed IR bellows with RF fingers made of copper-beryllium blades lying around the elliptical shape of vacuum chamber and the desired electrical contact is obtained by a blade pusher; on the top there is the volume for the insertion of the Higher Order Modes absorber, and a cooling pipe.

Further studies to evaluate the impedance of the whole IR beam pipe including the bellows, the BPM, and the remote vacuum connection are foreseen to consolidate the present estimates, and are essential to finalise the design.

3.3 Remote vacuum connection

The remote vacuum connection (RVC) system is a critical component in the MDI, necessary to provide vacuum sealing between the central beam pipes and those inside the cryostat. The RVC is located side in the non accessible region inside the cryostat at about 1.3 m from the IP. The RVC mechanism would allow to avoid damaging the delicate beam pipe infrastructure in case of vacuum failure or misalignment. Two possibilities are being considered. The first one is based on shape memory alloy (SMA) materials, chosen for the interesting property to return to a pre-defined shape upon heating after being deformed at a lower temperature (shape memory effects), to undergo large strains and recover its original shape when unloaded, without requiring heating (pseudoelasticity), and being radiation resistant [20] [21]. A second approach will consider a mechanism similar to the one designed and produced at DESY for SuperKEKB [22] using a remote manipulation system.

3.4 Vertex Detector

The IDEA silicon vertex detector features two main subsystems, whose active elements are based on 50 μm thick monolithic active pixel sensors (MAPS):

- an inner vertex detector, located close to the beam pipe, at radii between 13.7 and 35 mm, covering an angular acceptance of about $|\cos(\theta)| < 0.99$;
- an outer vertex detector, located at larger radii between 13 and 31.5 cm, composed of a barrel section and forward disks.

Two alternative layouts are being explored for the inner vertex detector. The first layout uses a traditional approach, in which modules are mounted on a carbon fiber support, with overlapping structures

to allow full coverage and alignment. The second, less advanced, layout is based on curved detectors, using a concept similar to the ALICE ITS3 [23].

The baseline vertex detector layout is illustrated in Fig. 10.

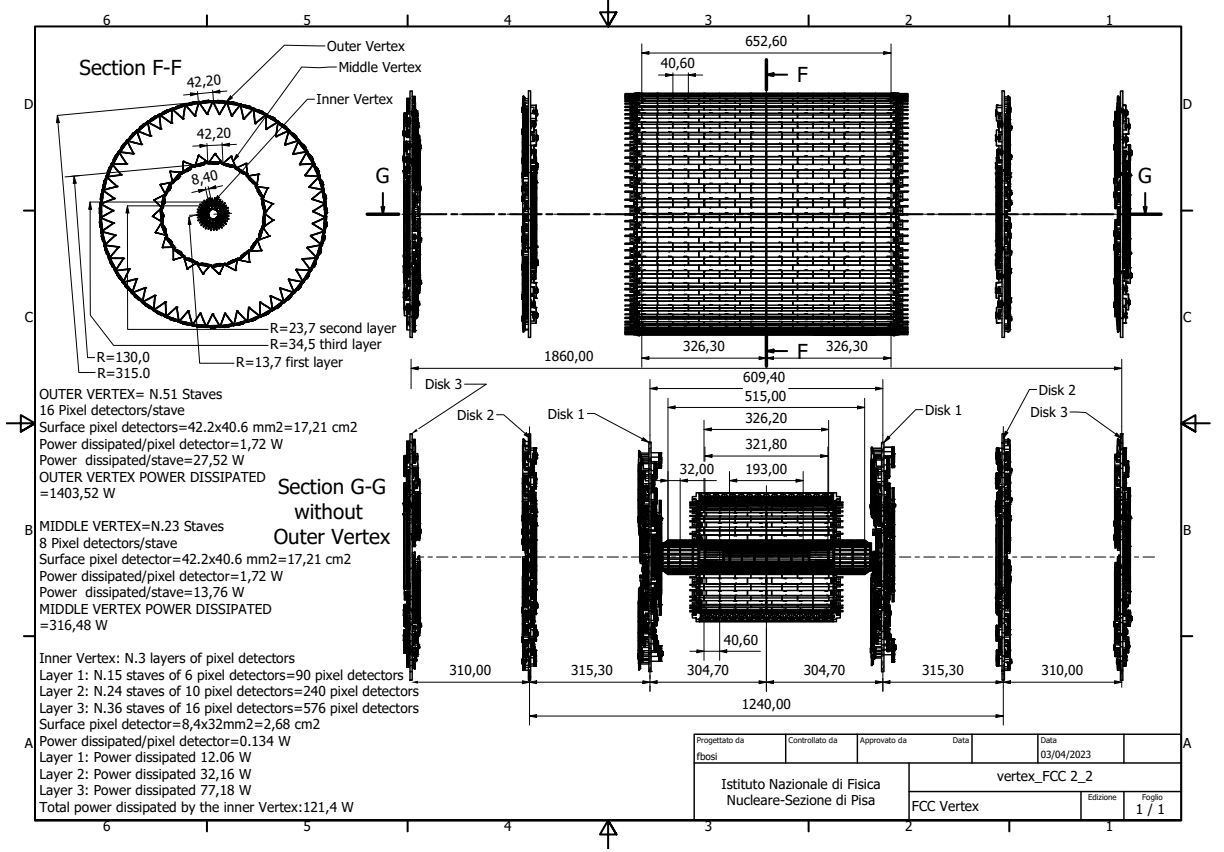


Fig. 10: Engineered layout and main characteristics of the baseline vertex detector. Dimensions are given in mm. Top left: cross sectional view showing the barrel layers; top right: longitudinal view showing the outer barrel and disks; bottom right: longitudinal view with the inner and middle barrels and disks. The left panel reports the main elements for the outer, middle and inner barrel detectors together with the power dissipated.

Baseline inner vertex detector

The inner vertex detector is composed of three concentric barrel layers mounted on carbon fiber support structures. The elementary unit is a module of dimensions $32(z) \times 8.4(r-\phi)$ mm 2 . Each module has two chips abutted in z inspired by the ARCADIA INFN R&D program [24]. The active area is made of $640(z) \times 256(r-\phi)$ pixels of 25×25 μ m 2 size. A 2 mm inactive space is envisaged in $r-\phi$, which contains the periphery of the chip. The power consumption of the current ARCADIA prototype, read out at 100 MHz/cm 2 , is measured to be about 30 mW/cm 2 , and considering the higher expected FCC-ee data rate and time resolution, 50 mW/cm 2 has been conservatively assumed. To allow 2 mm radial clearance for its insertion, the first layer is located at a radius of 13.7 mm. The length is constrained by the central beam pipe cooling manifolds. The first layer comprises 15 staves of 6 modules each along z , as shown in Fig. 11. The staves overlap in ϕ , to allow internal alignment. A lightweight support on each ladder provides rigidity and allows the mounting of the MAPS. The structure is made of thin carbon fiber walls interleaved with Rohacell, which holds the sensors (facing the beamline) and two buses (one for data and another for power) 1.8 mm wide each on the opposite side. The thickness of the bus comprises

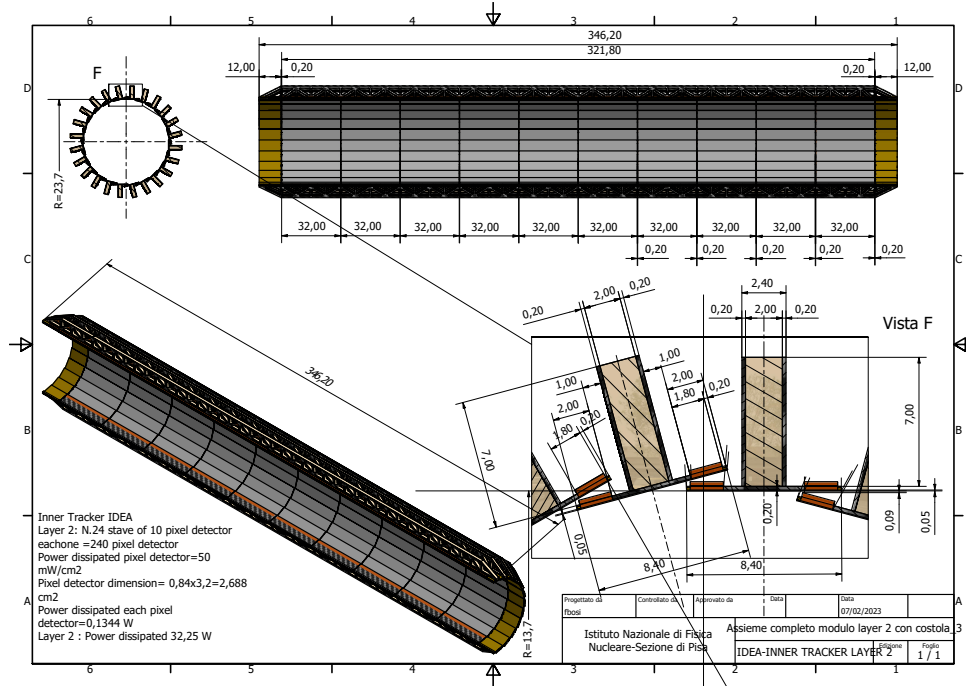


Fig. 12: Second layer of the baseline inner vertex detector. The top drawings show the transverse (left) and longitudinal (right) cross sections of the assembly, shown in three dimensions on the bottom left drawing. An enlarged view showing the overlaps and the different structures is given in the bottom right drawing. All measures are in mm. MAPS sensors of $50\text{ }\mu\text{m}$ thickness are facing the centre of the structure. The brown structures are the buses, while the gold parts are the electronic hybrid circuits for readout.

The power dissipated by each layer is reported in Table 7, and necessitates an active cooling system. Given the need to minimise the material budget, a system based on the forced convection of a gas inside the detector has been chosen. Both air and helium gas are being considered.

A system of carbon fiber cones is used to force gas convection inside the detector volume, also used to support power and readout cables, as shown in Fig. 14. The gas is channeled through the conical carbon fiber support structure, at the top of every stave.

The air cooling performance is analysed by means of Computational Fluid Dynamics (CFD) simulations, adapting the full CAD model of the vertex detector. In fact, due to the high complexity of this model, the simulation only considered an azimuthal sector, the largest allowed by the computational power available and the level of details needed by the physics of the simulation. Appropriate adiabatic boundary conditions have been set to the cut edges, to include the effects of the missing parts. The steps in the procedure are sketched in Fig. 15.

In order to set the conjugate heat transfer model, the fluid domain is also added to the model, and it is calculated as the negative part of the solid domain inside the sector. Both the solid and fluid domains are solved at same time. Inlets and outlets for the fluid domain were respectively given at the two endcaps. Although every layer has dedicated inlets and outlets, a radial crossflow of air between layers is possible due to small air gaps between staves, and this phenomenon is also reproduced with the model. About 40 million elements are needed to properly model the system. The longitudinal inlet air flow in all layers establishes a temperature gradient on the structure from inlet to outlet, shown in Fig. 16, and the highest sensor temperature at the outlet provides a good indicator of the thermal performance of the cooling system.

Figure 17 shows the temperature distribution on the three layers. The maximum temperature

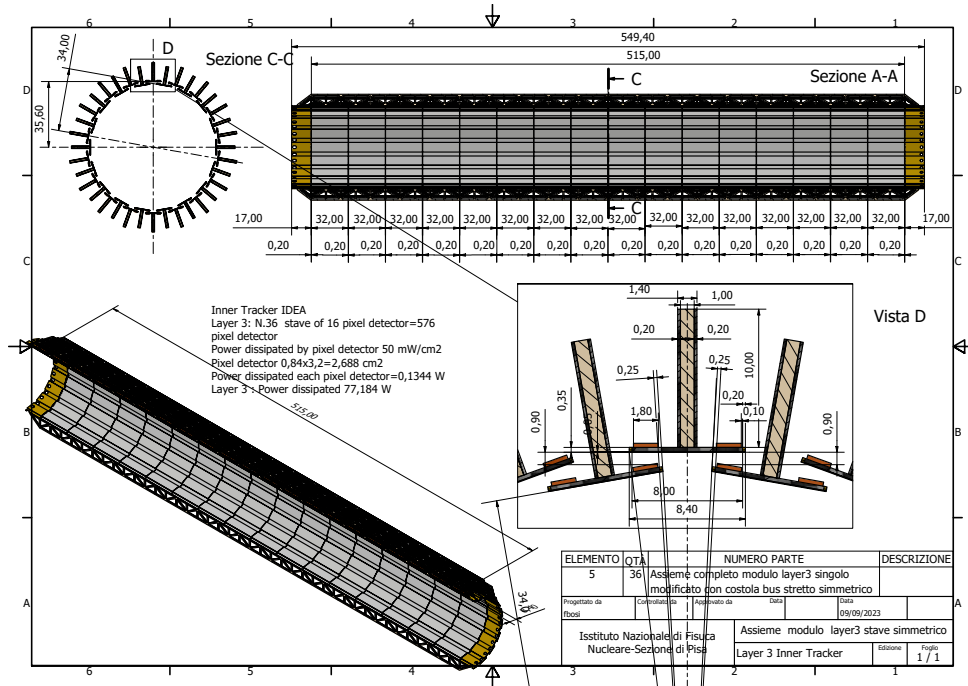


Fig. 13: Third layer of the baseline inner vertex detector. The top drawings show the transverse (left) and longitudinal (right) cross sections of the assembly, shown in three dimensions on the bottom left drawing. An enlarged view showing the overlaps and the different structures is given in the bottom right drawing. All measures are in mm. MAPS sensors of 50 μm thickness are facing the centre of the structure. The brown structures are the buses, while the gold parts are the electronic hybrid circuits for readout.

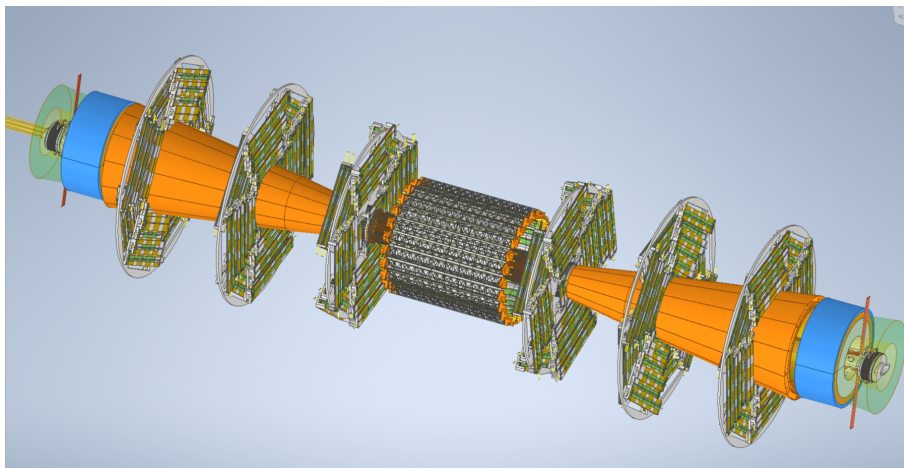


Fig. 14: View of the vertex detector middle barrel and disks together with the cooling cones. The blue parts are the two luminosity detector calorimeters.

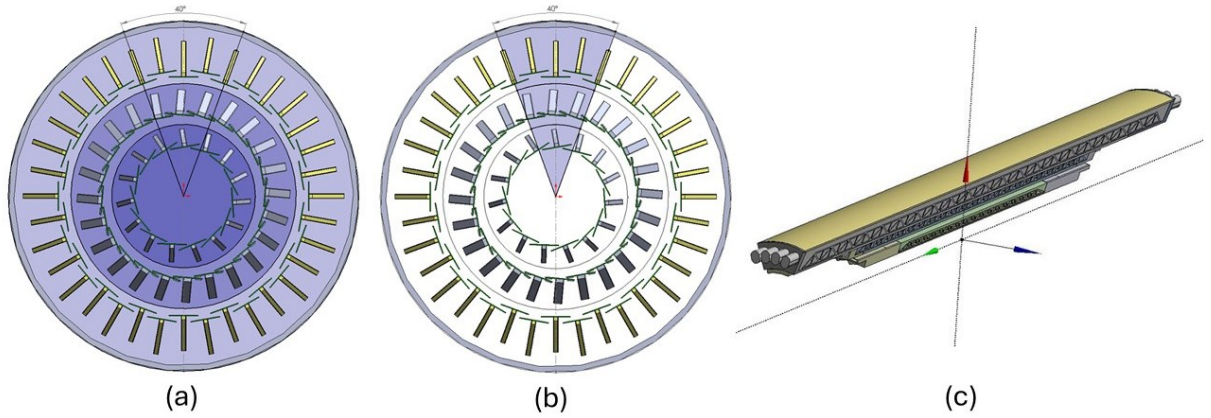


Fig. 15: Steps which have been done to simplify the geometry. Starting from the full geometry of the three layers (a), a slice of approximately 40° was extracted (b) and just the portion of model included inside was taken for simulations, with the addition of the air fluid domain (c).

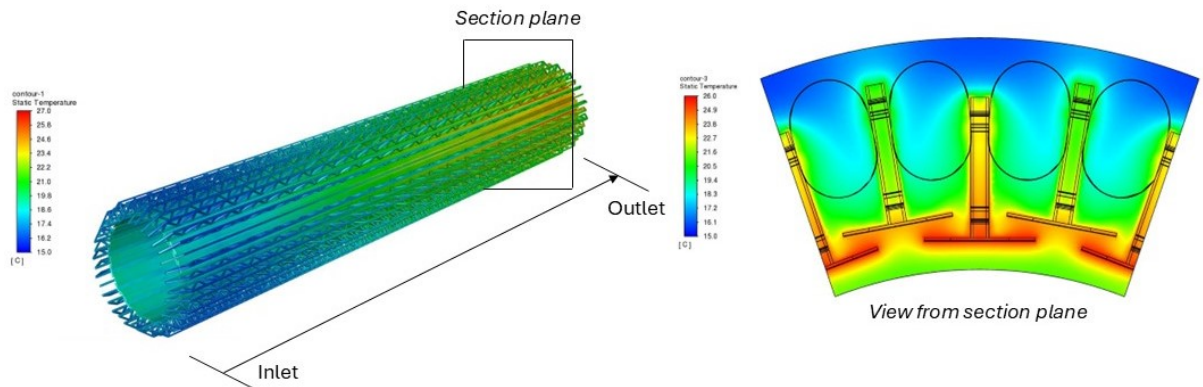


Fig. 16: Simulation of the temperature behaviour of the vertex detector layer 3, as seen in a three-dimensional view (left) and in the transverse view (right) indicated by the section near the outlet shown on the left side.

difference between the hottest sensors and the inlet air temperature in layers 2 and 3 is about 15°C for an air velocity of 10 m/s . The simulation also shows that layer 1 is not optimised, since the dimensioning of the holes is not sufficient to obtain the same cooling as for the other layers.

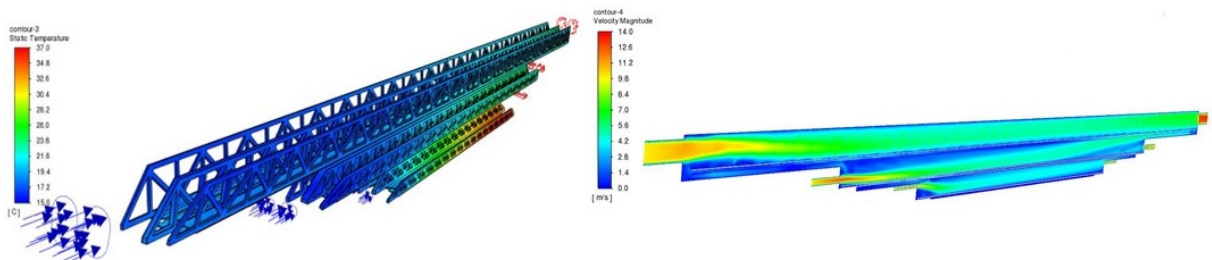


Fig. 17: In the left picture, the temperature field on the three layers, highlighting the warmer region at the end of layer 3. Looking at the velocity field (picture on the right), an ascending flow of air is detected towards the outlet, which could disadvantage the innermost region.

The behaviour of the maximum temperature of the sensors of Layer 3 as a function of the flow is

shown in Fig. 18, for air and gas flows for a hole diameter of 6 mm. The best behaviour of the helium is due to its higher thermal conductivity.

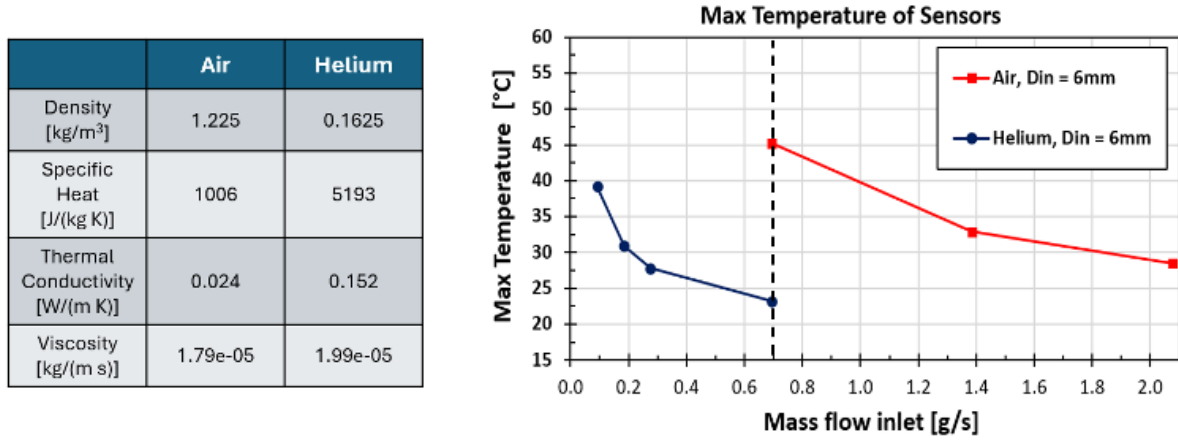


Fig. 18: Left: Thermal properties of air and helium. Right: layer 3 maximum sensor temperature as a function of the mass flow of air and helium, for a inlet air temperature of 15 °C and holes diameter of 6 mm.

A mechanical-vibrational analysis has also been performed. using the Finite Element Analysis (FAE) in the ANSYS software suite. The simplified solid domain used in the CFD studies has been exported to the FEA as shown in Fig. 19.

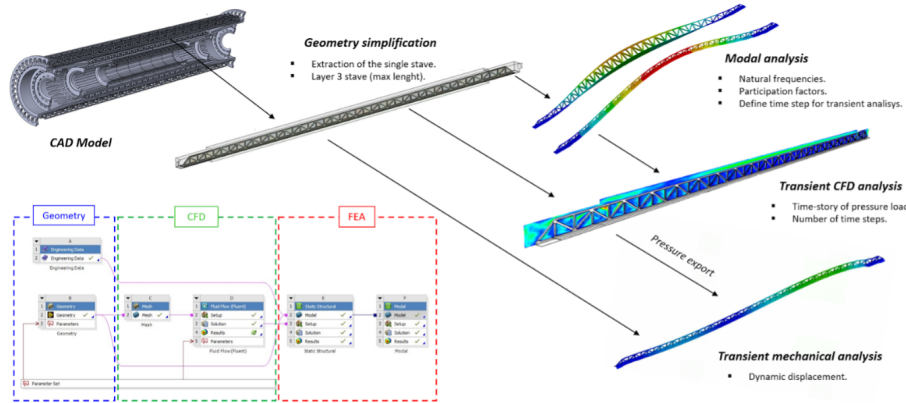


Fig. 19: An approach to investigate fluid-induced vibration in structures through the Ansys software.

The natural frequencies and vibrational modes of a single stave of layer 3 are shown in Fig. 20. The first mode frequency is about 120 Hz, corresponding to the the torsional vibration of the stave. Other higher order modes are shown in the same figure.

The natural frequencies have used to define the time-step for the CFD transient analysis, defined as $\Delta t < \frac{1}{10f_{\max}}$.

The CFD transient analyses, implemented by means of a Large Eddy Simulation (LES) model, allowed to define the time-dependent pressure field along the stave, to be used as an input of mechanical transient analysis. The results of the latter are reported in Fig. 21. The magnitude of the maximum displacement is of about 1.5 μm in radial direction, mainly due to the first flexural mode, indicating the need of stiffening the fixation of the stave to the support cone.

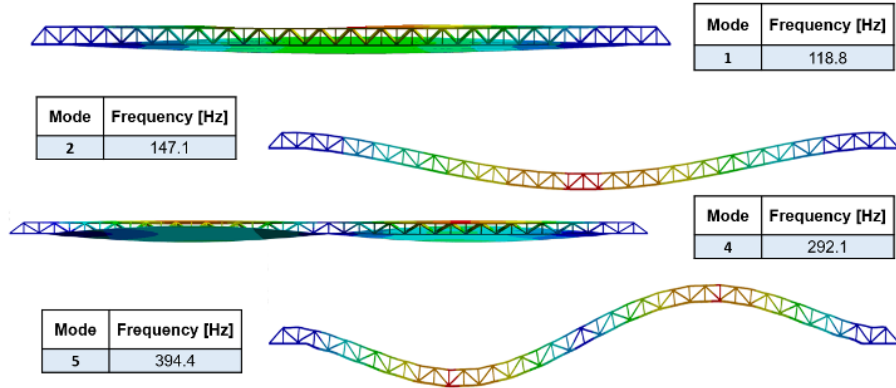


Fig. 20: Natural frequencies of the stave.

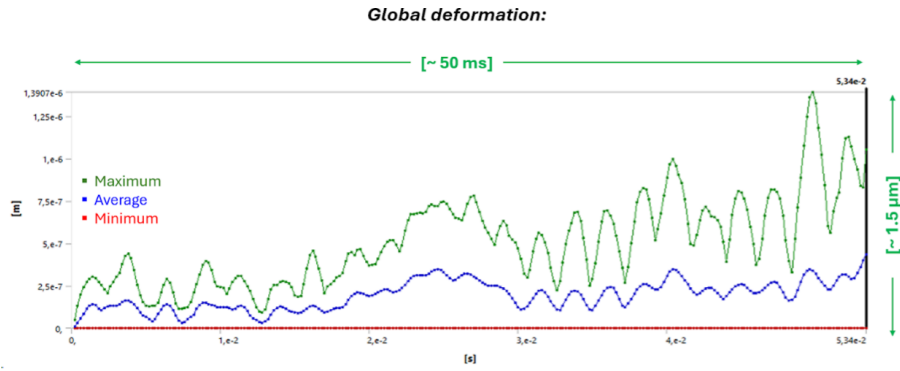


Fig. 21: Overall time dependent deformation of the stave due to air turbulence. In green the module of the maximum deformation in the three axes, while in blue the average over all the elements.

Ultra-light inner vertex detector concept

An alternative layout for the inner vertex is also explored, based on a similar concept of the ALICE ITS3 curved sensors technology [23], which allows a self-supporting structure with almost only silicon sensors in the acceptance, thus resulting in an ultra-light vertex layout. ITS3 uses the stitching technique to form wafer-scale sensors from multiple repeated sensor units (RSUs). Each ITS3 layer comprises two half-cylindrical sensors featuring ten RSUs in z and three, four, or five in ϕ for the first, second, and third layers. Unlike ITS3, the vertex detector at FCC-ee must cover the largest polar angle possible for all detection layers. The layers cover more or less the same angular acceptance to fulfill this requirement. To reach the small radius of 13.7 mm, the first layer only uses two rows in ϕ of 10 RSU in z as listed in Table 8. It is supported only by two carbon foam longerons and rings. The spacing between the two half-shells is 1.25 mm, thus leaving a gap in the ϕ acceptance, which is partially compensated by the second layer which is rotated in ϕ with respect to the first layer. It features one more row of RSUs in ϕ and 13 RSUs along z . The first two layers are read out and powered by either side. For the third and fourth layers, using two sensors in z per half-layer is foreseen to circumvent the limitation of the 12-inch wafer diameter. The third (fourth) layer uses 8 (10) layers on the $-z$ side and 10 (8) on the $+z$ side. In this manner, the gap in acceptance in z in one layer is covered by the other. For these layers, the readout only occurs on the far z sides.

Figure 22 shows the layout of this ultra-light vertex detector concept. Integration studies are ongoing to validate the technical feasibility of such a layout.

The material budget of such a solution is very much reduced with respect to the one using a classic design, as shown in Fig. 23 c. A single layer contributes to about 0.075% of X_0 at normal incidence, and

Table 8: Main parameters of the ultra-light inner vertex detector.

Layer	Sensors	Radius [mm]	RSUs in ϕ	RSUs in z	Length [mm]	Coverage
1	2	13.7	2	10	108.3	$ \cos(\theta) < 0.992$
2	2	20.35	3	13	140.8	$ \cos(\theta) < 0.990$
3	4	27	4	$8(-z)/10(+z)$	199.5	$ \cos(\theta) < 0.990$
4	4	33.65	5	$10(-z)/8(+z)$	199.5	$ \cos(\theta) < 0.986$

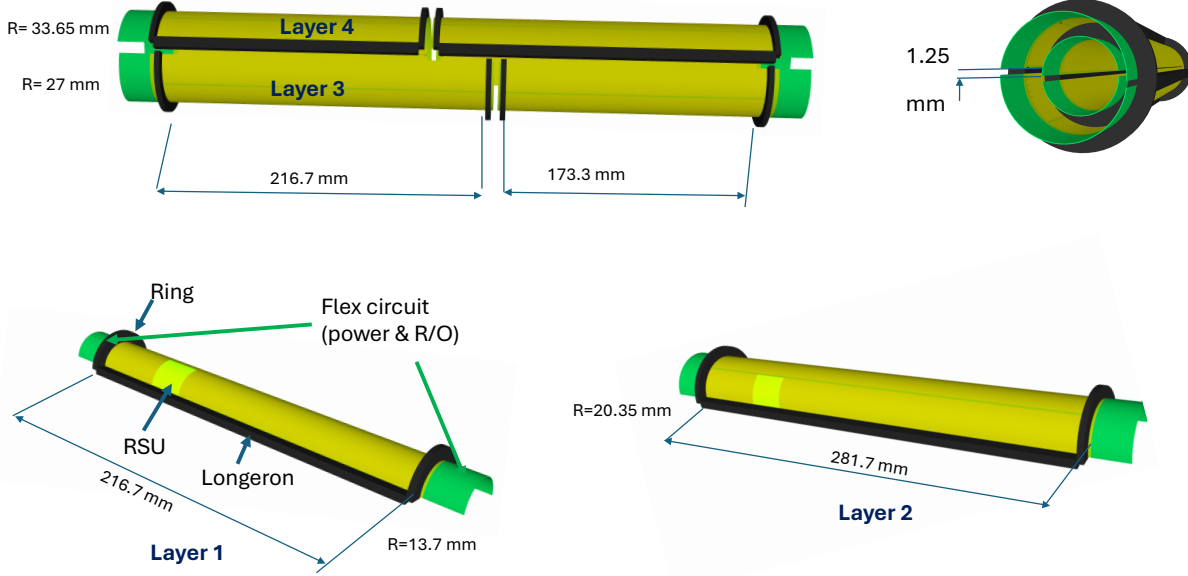


Fig. 22: Ultra-light inner vertex detector layout (see text for detailed explanation). The four half-layers are shown separately. On the top right hand side an assembled view of the first two layers is shown.

the material budget is more uniformly distributed in ϕ due to the absence of overlapping structures in the same layer as shown in Fig. 23 d.

Outer vertex detector and disks

The outer vertex detector is composed of two barrel layers and three disks on either side of the IP. The elementary unit is a module of dimensions $40.6(z) \times 42.2(r - \phi)$ mm². Each module has four hybrid pixel sensors inspired by the ATLASpix3 design [25]. The active area of the chip consists of 132 columns of 372 pixels each, with square pixels of 150×50 μ m². The sensor thickness of the modules is 50 μ m and their power consumption is assumed to be 100 mW/cm², half of the level observed at the current stage of development, but still too high (by at least a factor of two) to be handled by air cooling.

The same module type is used for the barrel layers and the disks. One barrel layer is placed at 13 cm radius (middle barrel) and is made of 22 ladders, each with 8 modules, as shown in Fig. 24a.

The outermost layer (outer barrel) is placed at 31.5 cm and is composed of 51 ladders of 16 modules each. The outer layer is supported by a flange that is attached to the external support tube. The flange also supports the middle barrel as well as the first disks.

The modules are placed on top of a lightweight triangular truss structure. The staves are mechanical structures holding the modules. Each stave is composed of a carbon fibre multilayered structure, comprising 120 μ m thick carbon fibre KDU13, and two carbon fleeces of 65 μ m in total, to support two polyamide tubes of 2.2 mm diameter and 90 μ m thick, in which demineralised water will be circulating. An electronic bus, bringing the power distribution and the readout and control signals, runs along the en-

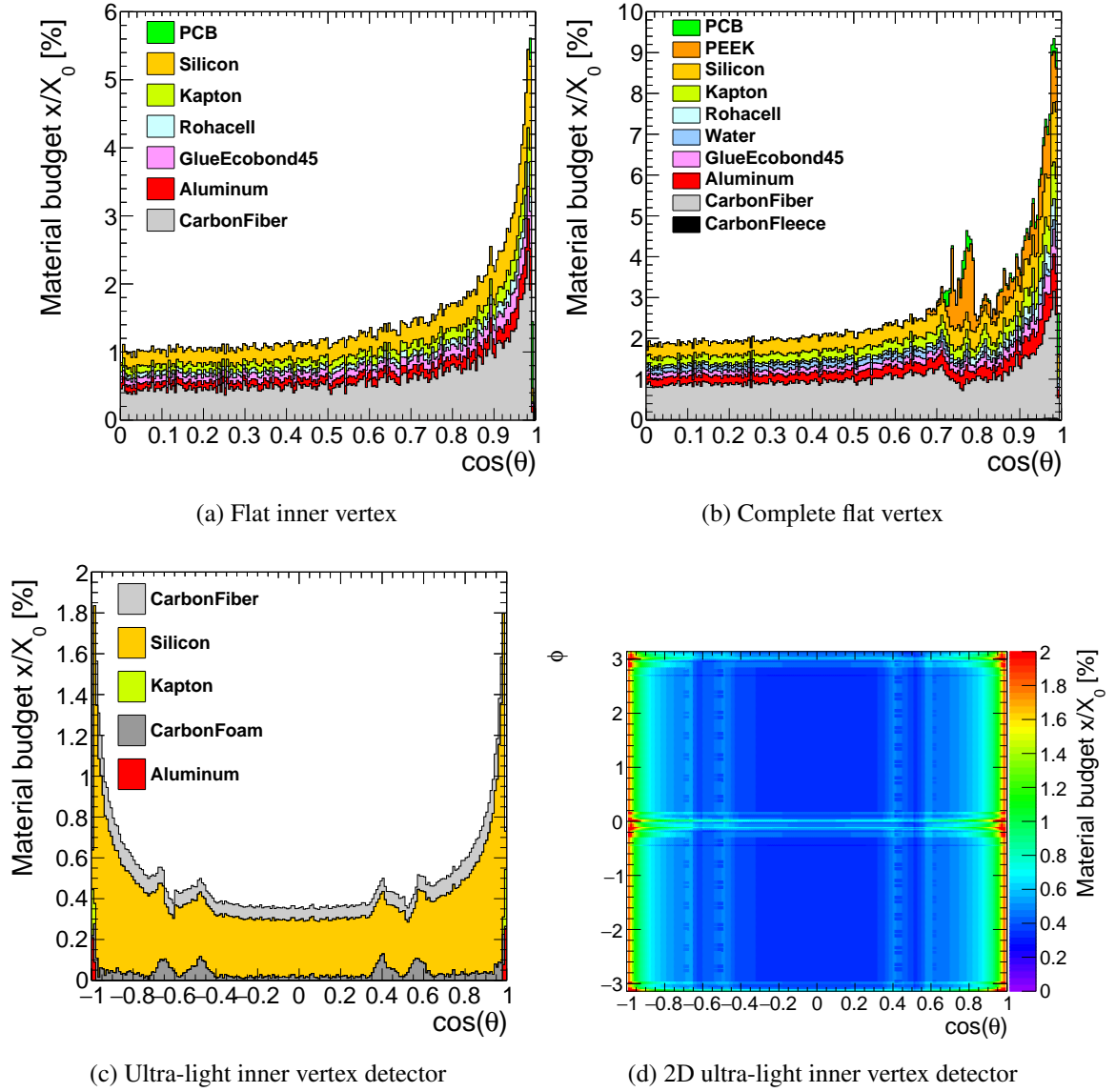


Fig. 23: Material budget for the vertex detector. On the top row for the flat inner vertex (a) and complete vertex detector (b). On the bottom row for the curved inner vertex detector (c) and two-dimensional distribution (d).

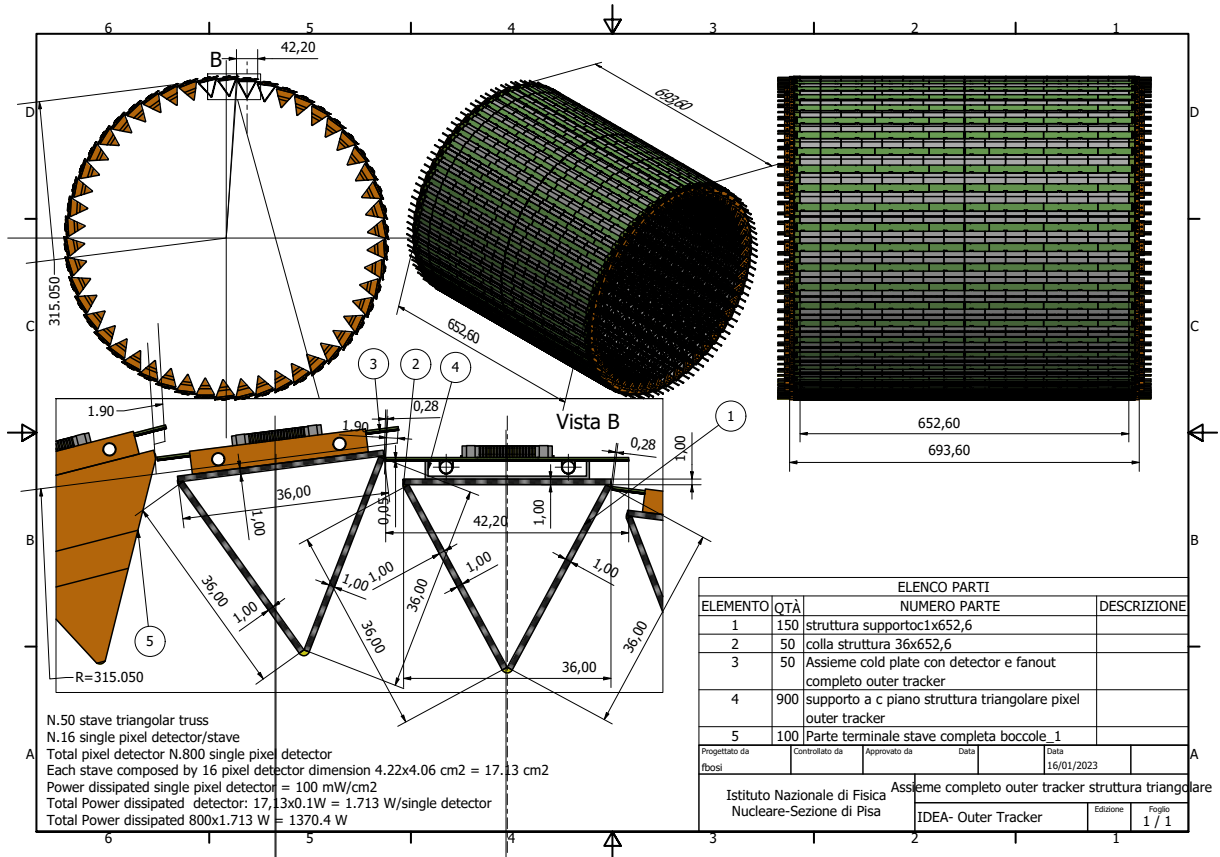
tire stave length and is put on top of the modules. It is terminated at the end of both sides of the stave by a hybrid circuit. Three disks per side, located at $z = \pm 29.25, \pm 62$ and ± 93 cm, complete the outer vertex tracker. The inner disk is located inside the barrel. Each disk comprises four front and backward petals, made of modules of the same type as those of the barrels, as shown in Fig. 24b. The support structure of each disk is made of a sandwich of thin carbon fibre walls (each of 0.3 mm thickness) interleaved with Rohacell (5.4 mm thick).

The material budget of the full vertex detector is shown in Fig. 23b.

3.5 Luminosity Calorimeter

The luminosity calorimeter is composed of two cylindrical devices, placed at about 1.1 meter away from the IP, centred around the outgoing beam directions. The calorimeter is composed of a multilayered

(a) Outer vertex barrel



(b) Disk 1

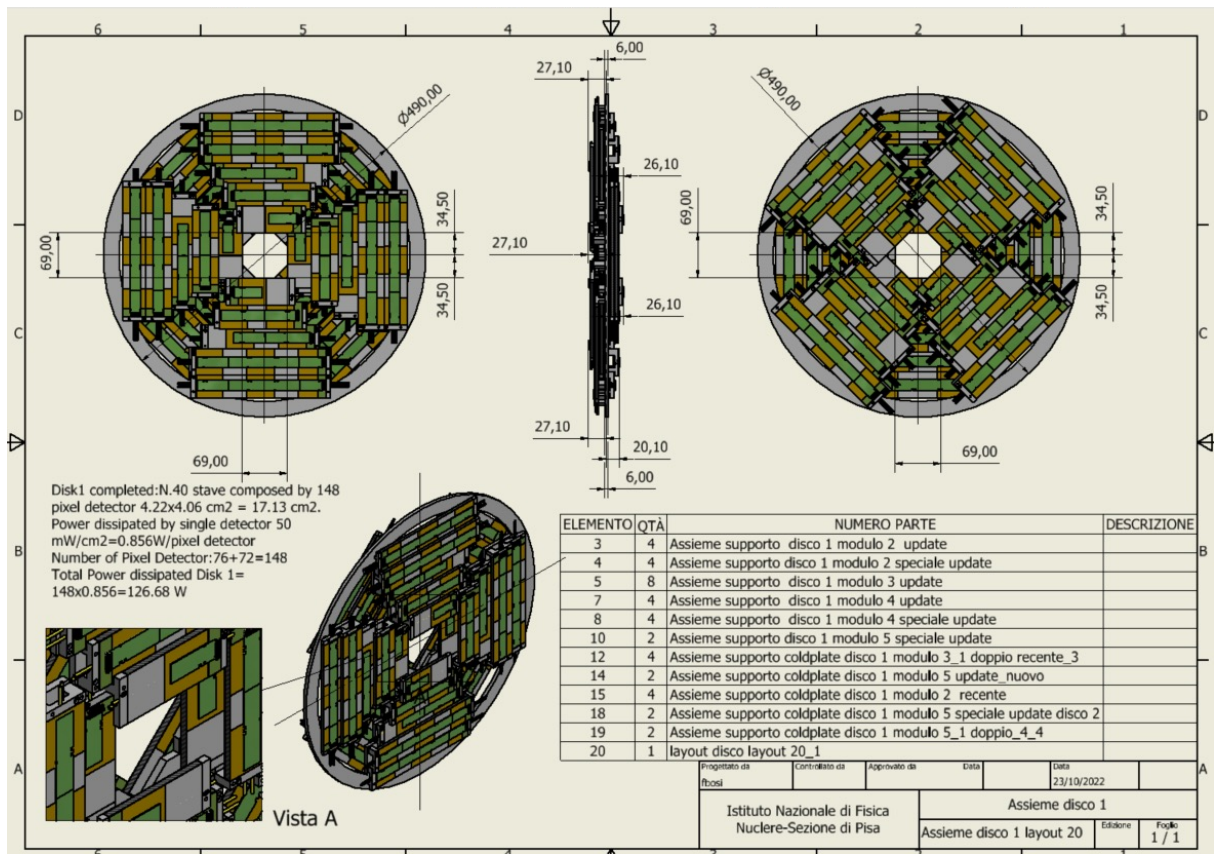


Fig. 24: Details of the outer vertex barrel (a) and first disk (b).

active structure, in which 26 passive tungsten circular disks, each of 3.5 mm thickness, are interleaved with 25 silicon pad detectors, in a 1 mm housing.

The physical dimensions of each calorimeter, shown in Fig. 25, span a sensitive radial coverage between 54 and 115 mm from the beamline. A 30 mm uninstrumented region at the outer circumference is reserved for services (front-end electronics, cables, and cooling), as well as for the physical structures (likely including precision dowels and bolts) needed for the assembly of the Si-W sandwich.

The front face of the calorimeter (the first tungsten disk) is located at 1074 mm from the interaction point.

The total weight of the calorimeter is about 65 kg per each side.

In order to measure the luminosity with an accuracy of the order of 10^{-4} the calorimeter has a stringent requirement on the knowledge of its boundaries. in particular:

- its inner radius needs to be defined with a precision of $\pm 1.5 \mu\text{m}$.
- its outer radius needs to be defined with a precision of $\pm 3.5 \mu\text{m}$.
- the relative positioning of the two sides needs to be known with a precision of $\pm 110 \mu\text{m}$.

The expected budget is estimated of the order of 130 W per calorimeter side, to be removed by cooling. For the required geometric precision, the temperature needs to be controlled to within a tolerance of 1°C .

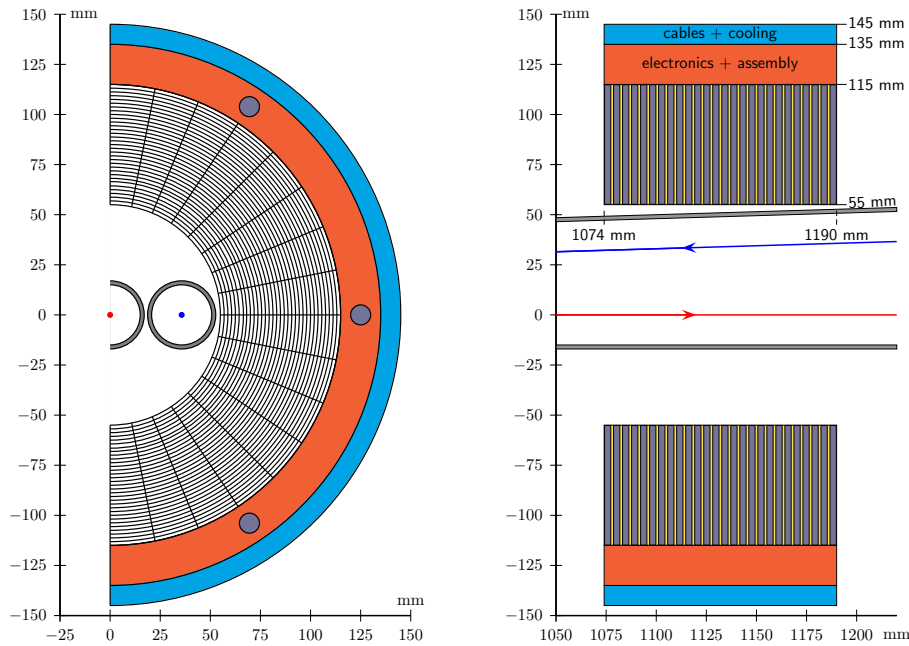


Fig. 25: Front view (left) and top view (right) of the luminosity calorimeter, centred around the outgoing beam direction (shown as a red arrow). A possible segmentation of the Si pads is seen in the front view. Surrounding the sensitive region are regions for front-end electronics (red), and for cables and cooling (blue). The top view shows the interleaved silicon-tungsten layer structure.

The tungsten disks and the silicon pads must be assembled as single-piece parts, in order to fulfill the requirements of the very accurate positioning: once assembled, the calorimeter is a rigid hollow cylinder. An example of the difficulty of the integration of the LumiCals with the MDI and the detector system is shown in Figs

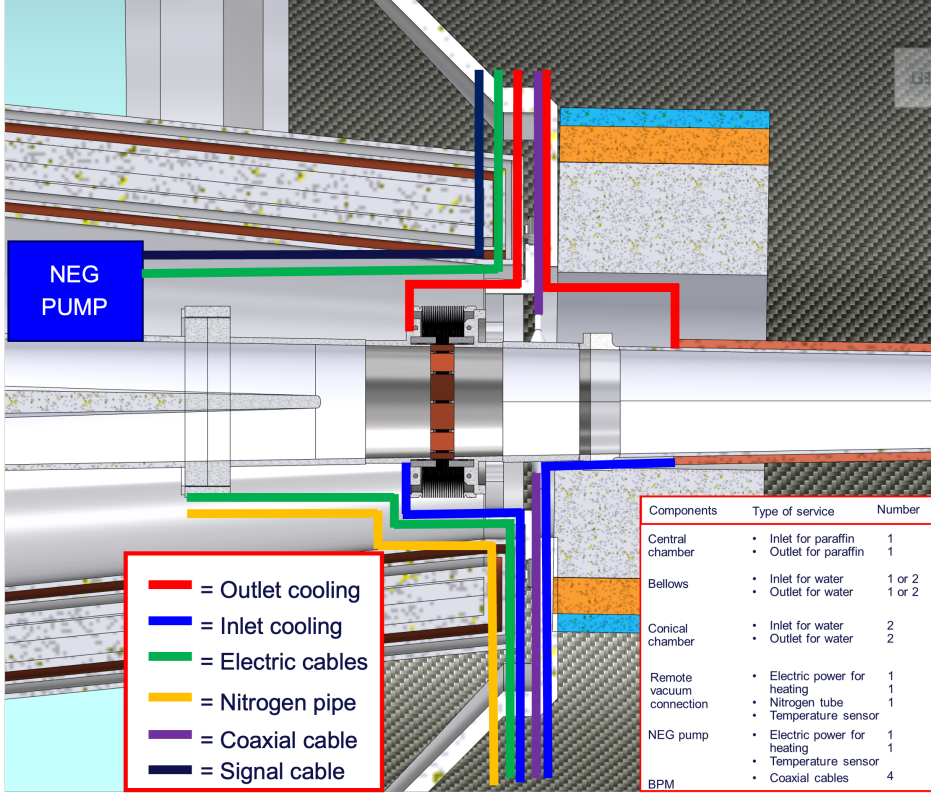


Fig. 26: Services integration of the luminosity calorimeter in the MDI region.

3.6 Optimisation of the beam pipe material budget

The minimisation of the material budget of the beampipe is of utmost importance to enhance physics performances. For this reason different configurations of the material and their thickness have been studied. This section describes the possible alternative solutions and their impact on the luminosity calorimeter and in the region of the tracking detectors up to $|\cos \theta| < 0.99$.

The current engineered design of the beam pipe takes into account a safety margin of 4 in the buckling resistance, and results in a material budget within the LumiCal acceptance ranging from approximately $0.07 X_0$ and $0.5 X_0$, as shown in Fig. 27. The maximum values of the material budget, originating from the AlBeMet cooling manifolds, are at a safe distance from the 50 mrad cone. Similarly, Fig. 28 reports the material budget of the beampipe as a function of $\cos(\theta)$. For each bin of θ , the material budget value is calculated as the average over ϕ in the range $[0, 2\pi]$. At normal incidence the total contribution is 0.68%, with the main contribution comes from the AlBeMet. The energy deposited in the Lumical by Bhabha scattered electrons of 45.6 GeV is shown in Fig. 29.

The potential use of a beryllium beam pipe has been investigated due to its higher radiation length $X_0^{\text{Be}} = 352, 80 \text{ mm}$ compared to AlBeMet $X_0^{\text{AlBeMet}} = 190, 66 \text{ mm}$. This change would improve both the material budget and the energy deposited in the LumiCal coming from the beam pipe. Figs. 30 and 31 present the same plots, but with each AlBeMet element replaced by beryllium. Within the LumiCal acceptance, the material budget ranges from approximately $0.03 X_0$ and $0.25 X_0$, nearly a factor of two improvement compared to AlBeMet. For large θ , the total contribution from the beam pipe is $0.51\% X/X_0$. The energy deposit coming from the beam pipe is further decreased just below the LumiCal acceptance, as shown in Fig. 32. However, compared to the AlBeMet case, the improvement is minimal.

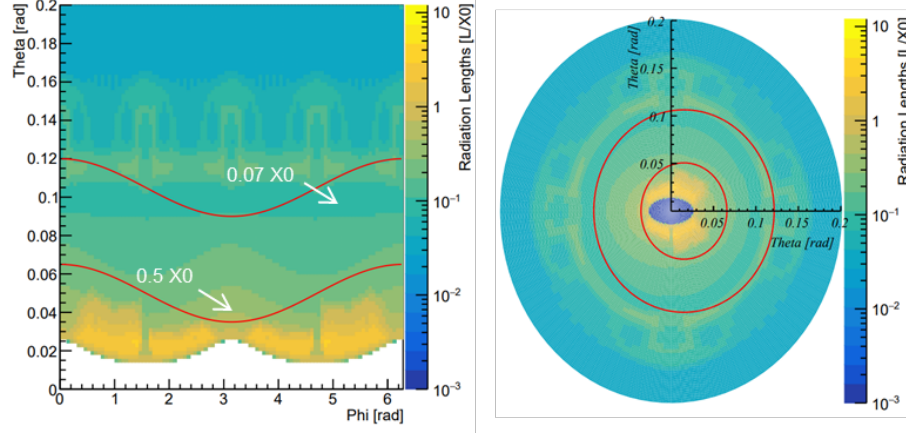


Fig. 27: Material budget of the engineered design of the beam pipe, shown in the region $\theta \in [0, 0.2]$ rad for $\phi \in [0, 2\pi]$. The red lines represent the Lumical acceptance, i.e. the 50 mrad and 105 mrad cones.

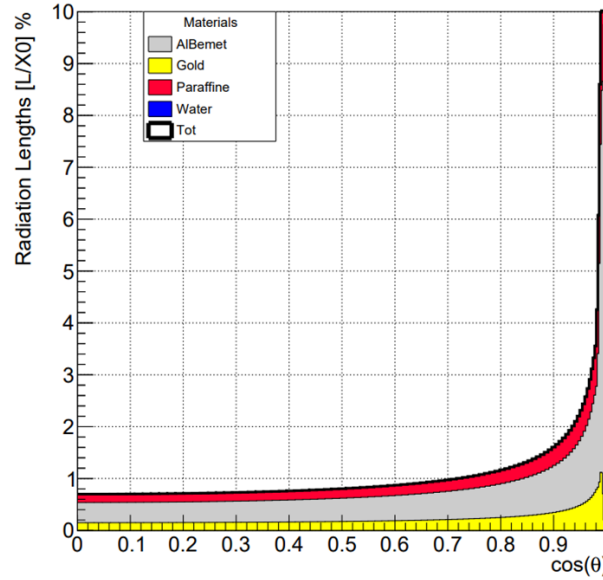


Fig. 28: Material budget of the beam pipe for $\theta \in [0, 2\pi]$ averaged over $\phi \in [0, 2\pi]$.

To further reduce the material budget, the possibility of using a thinner internal gold coating layer has been explored. Impedance studies have shown that the gold layer can be reduced up to $2 \mu\text{m}$ without affecting its impact on the impedance [26]. Figure 33 presents the material budget for the beam pipe design with a $2 \mu\text{m}$ thick gold layer instead of $5 \mu\text{m}$. Within the LumiCal acceptance the material budget remains unchanged, while the total contribution for high values of θ decreases to $\sim 0.59\% X/X_0$.

Assuming a beryllium pipe, the contribution further reduces to $\sim 0.42\% X/X_0$, as shown in Fig. 34.

Due to the relatively low ignition temperature of liquid paraffin, a preliminary study on the material budget for the case of water cooling for the central chamber has been considered, which would allow a safer operation environment. Two geometries are considered: the first one with the same cooling channels as for paraffin, and a second one with a channel for water flow of $600 \mu\text{m}$. The former causes an increase in the minimum value of the material budget. The total contribution for large θ rises to $\sim 0.79\% X/X_0$, while in the LumiCal acceptance no effect is expected, due to the lower polar angle.

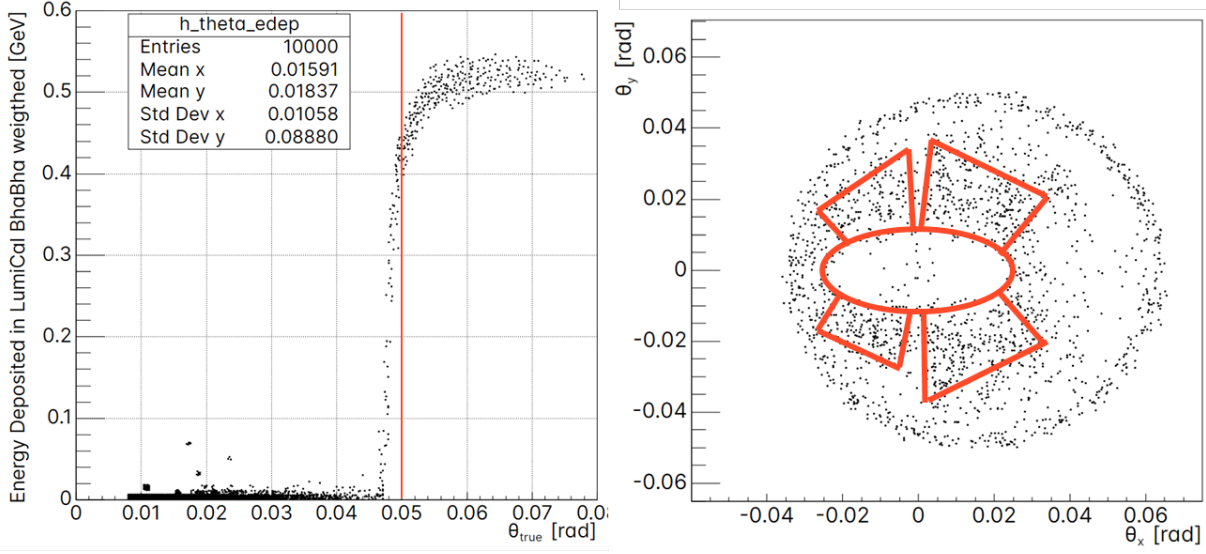


Fig. 29: Left: Energy deposit coming from the beam pipe from Bhabha electrons at the Z pole. The red line shows the 50 mrad acceptance angle. Right: Angular distribution of hits that generated the energy deposit in the Lumical.

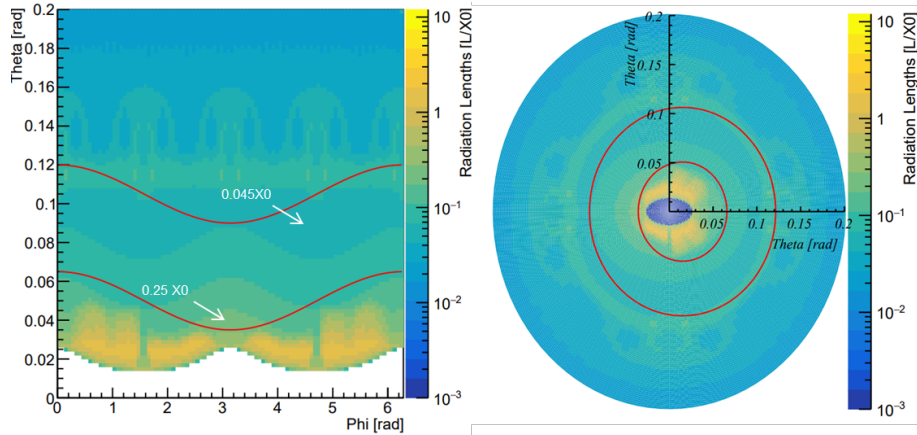


Fig. 30: Material budget of the current beam pipe design, with Beryllium instead of AlBeMet.

4 Integration of the Interaction Region

This section deals with the integration of the interaction region, namely the vacuum chambers and bellows, the vertex and LumiCal detectors, inside the IDEA detector with the support tube concept in Sec. 4.1. A preliminary alignment strategy is given in Sec. 4.2, followed by the overall detector maintenance and opening issues within the experimental cavern in Sec. 4.3.

4.1 Support tube

A support tube concept has been developed to ease the integration of the accelerator and detector components into a single rigid structure, as discussed originally in Ref. [1]. The support tube, shown in Fig. 5, is an empty lightweight cylindrical structure, and is designed to provide a cantilevered support for the pipe, support the LumiCal, and the outer vertex and disks. Its walls are made of a multiple layer structure, as described in Table 9.

The support tube is longitudinally split in two half-cylinders. At both ends, two rigid lightweight aluminium structures support the LumiCal and the vacuum tubes. Six aluminium ribs are fixed to the

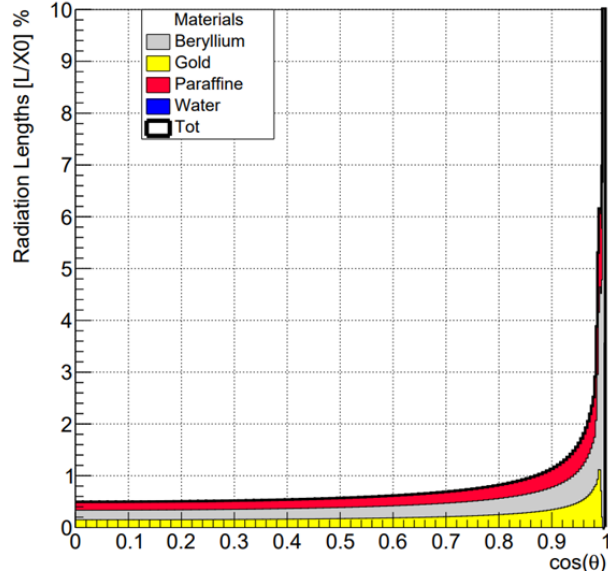


Fig. 31: Material budget of the current beam pipe design, with Beryllium instead of AlBeMet for $\theta \in [0, 2\pi]$.

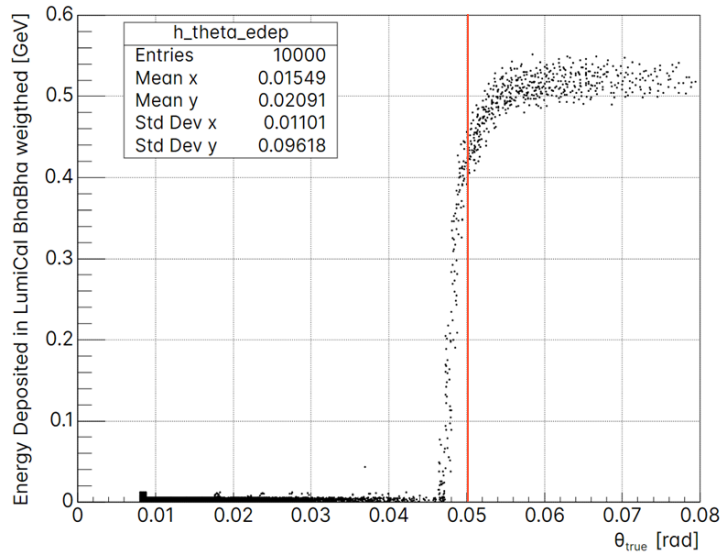


Fig. 32: Energy deposit of Bhabha scattered electrons coming from the beam pipe in Beryllium just below the LumiCal acceptance (red line).

inside of the tube to support the outer vertex and the disks.

The insertion of the support tube in the detector is foreseen either with a few sleds or with longitudinal rails fixed to its external surface. A possible option could then be to slide these sleds (rails) inside hollow carbon fibre rails, permanently fixed on the inside wall of the tracker to guarantee the structural rigidity while inserting the support tube. The corresponding calculations and simulations are beyond the scope of this feasibility study.

A structural analysis has been performed to calculate the stress and displacement of each part of the support tube, taking into account the estimated weights of detector elements, including services material with suitable safety margins, as in Table 10, considering a double fixed ends case as constraint configuration. The result shows that the structural resistance is safely respected.

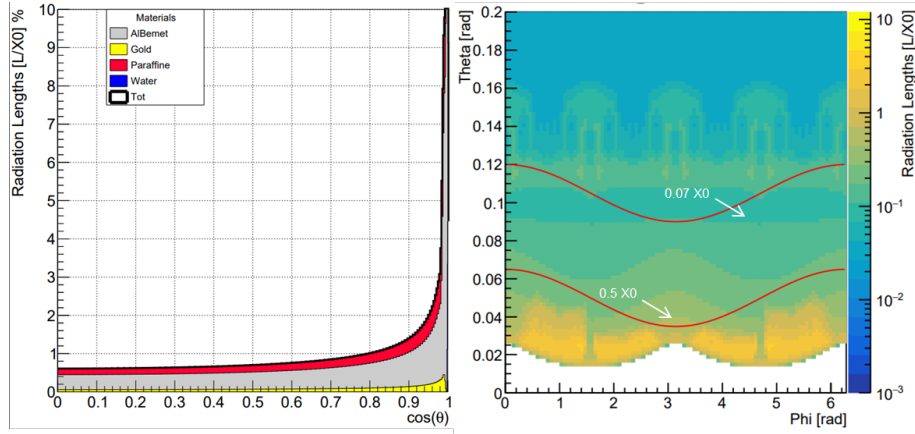


Fig. 33: Material budget of the current beam pipe design, with a Gold layer of $2\ \mu\text{m}$ instead of $5\ \mu\text{m}$.

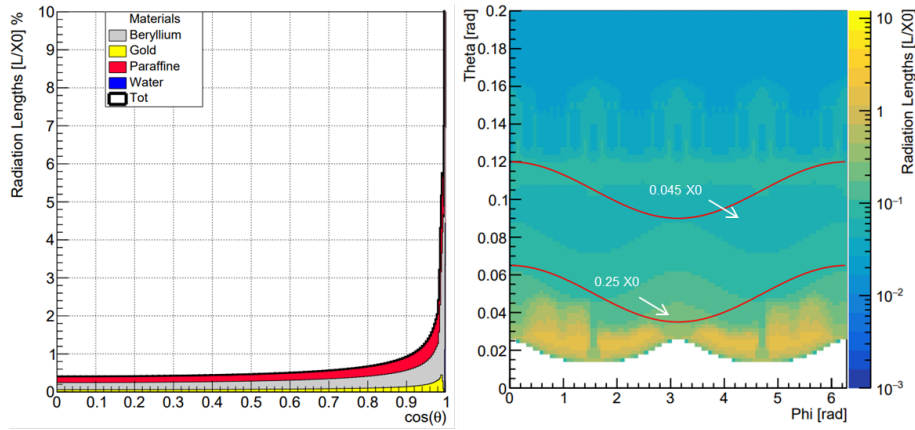


Fig. 34: Material budget of the current beam pipe design, with a Gold layer of $2\ \mu\text{m}$ and Beryllium instead of AlBeMet.

Table 9: Composition of the multiple layers structure of the support tube.

Thickness [mm]	Material	Orientation
1	Epoxy carbon woven (230 MPa)	45/-45/45/-45
4	Honeycomb	0
1	Epoxy carbon woven (230 MPa)	-45/45/-45/45

The results of the analysis are summarized in Table 11, they show the small stress and displacement values.

4.2 Alignment strategy

Since the MDI's design and requirements are extremely demanding, no existing system can be easily adapted to it. The alignment and monitoring system proposed will be composed of three main subsystems, as described in [27]: a deformation monitoring system, a short distance measuring system and a long-distance measuring system.

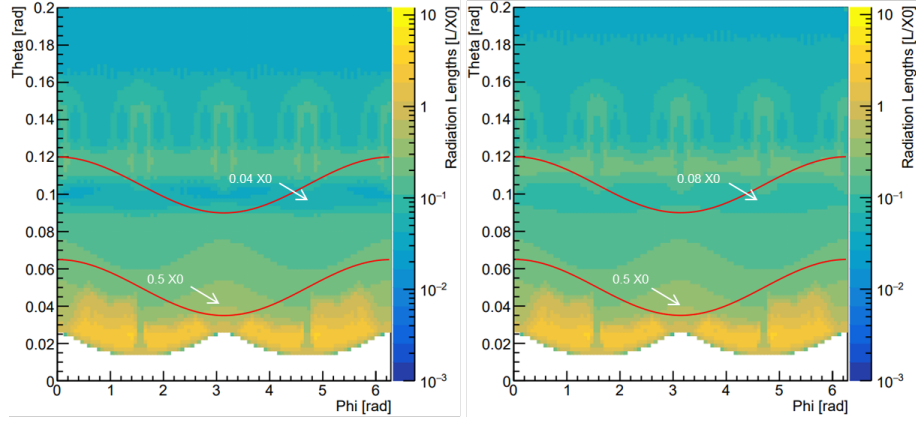


Fig. 35: Material budget of the current beam pipe design, with water cooling of the central chamber instead of paraffin. Left: $\varnothing 600 \mu\text{m}$ cylinder geometry. Right: 1 mm channels as for paraffin.

Table 10: Loads on the support tube taken in account for the structural resistance analysis. The weight of the disks, middle and outer vertex, a safety margin of 3 has been considered.

Component	Value [kg]
Vacuum Chamber	51
LumiCal	2×70
Disks	6×10
Middle vertex	7
Outer vertex	15

Table 11: Structural analysis of the support tube, results of the maximum stress and maximum displacement.

Support tube	Maximum stress [MPa]	Maximum displacement [μm]
Aluminium flanges	2.70	13
Aluminium ribs	0.2	26
Honeycomb	0.02	28
Carbon fiber	0.60	28

Alignment requirements

All the alignment requirements discussed below are expressed with a 1σ uncertainty. On the accelerator side, the alignment and monitoring of the final focusing quadrupoles must achieve a measurement uncertainty on the order of $30 \mu\text{m}$ relative to the ideal beamline. Beam Position Monitors (BPMs) need to be aligned and monitored with a measurement uncertainty on the order of $20 \mu\text{m}$ relative to the magnetic axes of the associated quadrupoles. The solenoids must be installed and monitored with a measurement uncertainty on the order of $100 \mu\text{m}$ relative to the magnetic axis of the detector solenoid.

On the detector side, the LumiCals must be monitored with a measurement uncertainty on the order of $50 \mu\text{m}$ relative to the ideal beamline and the Interaction Point (IP), with an additional constraint of $100 \mu\text{m}$ for the longitudinal position of the two LumiCals. The inner tracker and vertex detector must be installed and monitored with measurement uncertainties on the order of $50 \mu\text{m}$ and $20 \mu\text{m}$, respectively, relative to the IP and the LumiCals, to achieve sub-micron precision using the detector measurements for fine alignment monitoring.

It is important to emphasize that continuous monitoring is required in addition to the initial align-

ment. These values may still evolve.

The deformation monitoring system

The core challenge of aligning the MDI lies in the very limited space available, the difficult conditions, and the lack of direct access for measurements. A system capable of monitoring the shape of the screening solenoid's support could therefore provide a solid basis for other measurements, offering a precisely known shape (a cylinder) that can be used as a reference, as described in [28]. This deformation monitoring system uses In-Line Multiplexed and Distributed Frequency Scanning Interferometry (IMD-FSI) to monitor sections of optical fibers firmly installed on the inner surface of the screening solenoid support. These seemingly normal fibers are divided into sections by introducing a change in the refractive index along the optical path. This change in refractive index can be achieved through splicing or laser printing, for example. Each of these sections can then be measured simultaneously and independently using FSI. The fibers will deform along with the screening solenoid support to which they are securely attached, resulting in contractions or expansions in the localized fiber sections depending on the deformation. The deformation can then be calculated through a least-squares adjustment. Once the deformation is known, the shape and reference positions can also be determined.

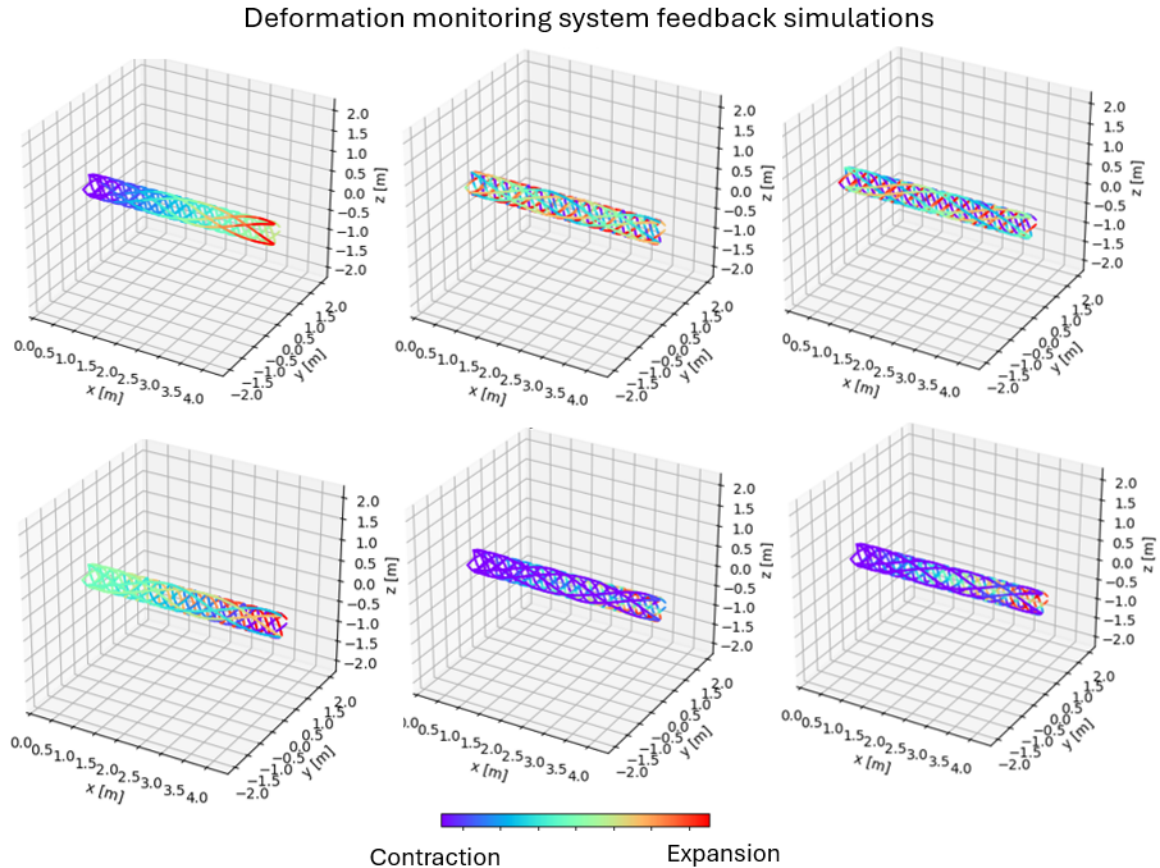


Fig. 36: Optical fiber layout in the screening solenoid to measure its deformation. Deformations simulated on the tube from top left to bottom right: elongation, horizontal radial deformation, vertical radial deformation, torsion, horizontal radius deformation.

This system will occupy no more than 5 cm^3 within the assembly and will require an interface with the endcap of QC1. Prototype testing has begun. Proof of concept has been established for the measurement thanks to prototypes and advanced testing is ongoing for the final validation (mathematical

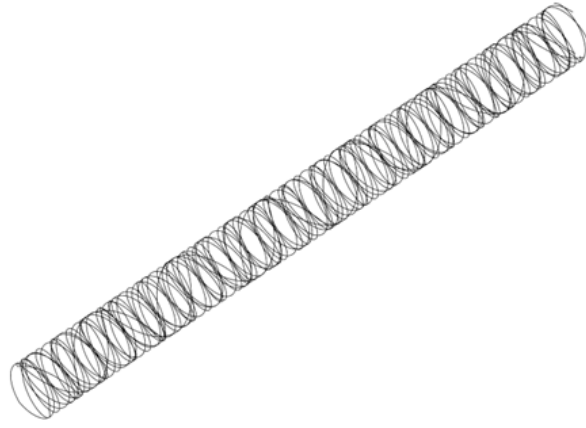


Fig. 37: First proposition for fiber placement inside the screening solenoid support.

determination of a deformation measurement). In addition, refinements on the technology are ongoing: testing rad-hard fibers, laser printing and ways to fix the fibers to the support tube.

The short distance measuring system

At the end of each fiber used in the deformation monitoring system, a mirror is installed to redirect the laser beam toward the center of the assembly, targeting the final focusing quadrupoles, the BPMs, LumiCals, and any other components that require monitoring. This subsystem is very similar to the FSI heads installed on the Low Beta quadrupoles in the HL-LHC MDI, as described in [29]. These distance measurements will monitor the position of the inner components relative to the cylinder. A similar system could also be implemented to measure the relative alignment between two components in greater detail if required, such as between a quadrupole and a BPM. This system is known and already used at CERN. The only modification required is miniaturization.

The long-distance measuring system

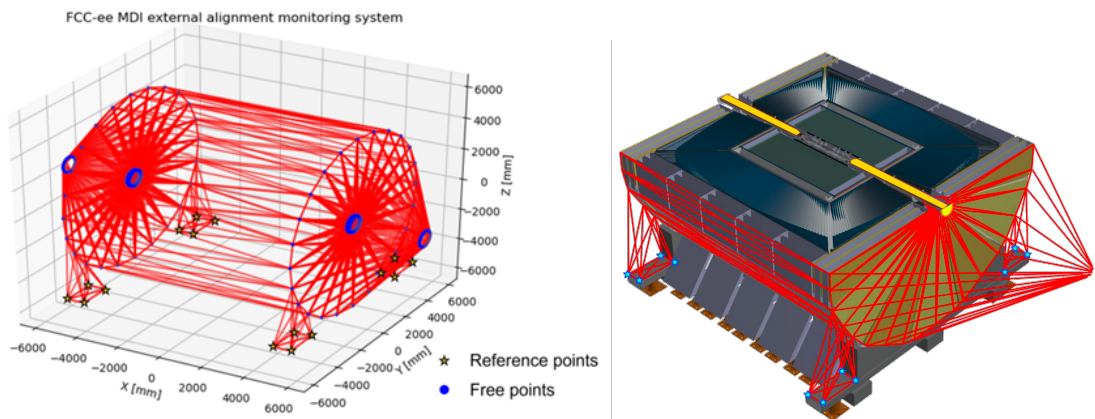


Fig. 38: Proposition for a distance measurement network around the detector. Red lines show the distance measurements, blue points points placed on the detector, and the stars reference points on the detector feet.

Finally, to ensure the alignment of both sides of the MDI, a long-range alignment system is installed. This subsystem, shown in Figure 38, is also based on FSI but uses a different optical setup to

enable longer-distance measurements. A dense network of such measurements around the detector provides a continuous link between the endcaps of the QC1 on each side of the MDI, which serves as the reference surface for the cylinder monitored by the deformation system. Reference points are placed on the feet of the detector, easy to access for a technician or a robot, to be used to link to the cavern survey network and the rest of the accelerator.

The alignment and monitoring of the vertex detector will be performed using a combination of short and long-range distance measurements with FSI technology. A network of distance measurements will link the positions of the vertex detector, the LumiCals, and the beam pipe, providing all the necessary information to refine the alignment using the detector measurements themselves. This system's final design is currently being studied, testing is ongoing.

Initial alignment and installation of the alignment and monitoring system

First, it is important to note that no adjustment system has been implemented in the current plan. This possibility is explored in more detail in the next section. The installation phase will be crucial, as the QC1 assembly will remain inside the detector for its entire lifetime, with no access possible for maintenance, adjustments, or repairs. The alignment of the components must be as precise as possible to their designed positions in the CAD models. Laser trackers or even CMM (Coordinate Measuring Machines), if feasible, could be used to monitor this process. Once a cryostat (QC1 or QC2) is assembled, a series of tests should be performed to validate the installation of the internal components under all conditions (cryogenic, vacuum, etc.) while monitoring the alignment. The proximity of the assembly lab would allow for possible adjustments. To conduct these alignment tests, a method like the SSW (Single Stretched Wire method) used in SuperKEKB, described in [30], could be applied to individual cryostats (such as QC1) and then to multiple cryostats in a row (e.g., QC1 and QC2). This measurement will serve two purposes:

- Check alignment under all conditions: The assembly's alignment must be verified under all conditions it will encounter in the machine (warm, cold, under vacuum, with magnets on and off) to detect any potential displacement or deformation. If the alignment cannot be maintained throughout these steps, components may need to be intentionally misaligned so that they align correctly during operational conditions.
- Calibrate the alignment monitoring system: This measurement bench will be the last opportunity to partially crosscheck the alignment with other systems. It will also establish a perfect reference position that can be used later.

Once every cryostat is aligned and checked, another SSW measurement could be performed after the entire MDI is assembled, as it was performed in SuperKEKB. It is important to note that simultaneously checking the alignment of both the magnet and the BPM would be highly convenient, as the relative alignment between the quadrupole and the BPM is extremely valuable.

Further alignment considerations

Due to the complexity, density, and limited accessibility of the MDI, any misalignment of its internal components could be highly problematic, potentially incurring significant time and cost to repair, as it would require disassembling the entire MDI, including the cryostat. Implementing an adjustment system beneath the final focusing quadrupoles, enabling displacement even when fully assembled, would be highly beneficial. Key parameters to consider include movement speed and precision, displacement range (accounting for necessary rotations and translations), operation under cold and vacuum conditions, and the feasibility of adjustments during machine operation.

The QC1 endcap will be monitored from both sides using long-range FSI devices mounted on the detector structure. The alignment system can also be utilized to install, align, and monitor surrounding

subdetectors, similar to its role with the vertex detector. This approach offers several advantages: it aids in subdetector initialization, ensures relative alignment between multiple subdetectors, aligns the accelerator with the subdetectors, and provides information on the IP position relative to the subdetectors. Additionally, it enhances the MDI network by improving overall alignment accuracy.

4.3 Global detector maintenance and opening

Any design of a high-energy detector shall include, since the beginning, considerations on its accessibility for assembly, maintenance and repair tasks. This section focuses on the constraints imposed by the detector's external environment, specifically the geometry of the experiment cavern and the layout of the machine elements, with particular attention to the final focus quadrupoles (FFQs) and their supporting structures.

Cavern vs detector size

In the baseline design, four interaction points (IP) are foreseen at FCC-ee. Two of them will be dedicated to general purpose detectors and hosted inside large caverns (Fig. 40) and the others two to other detectors hosted inside smaller caverns (Fig. 41). They are all located at a distance from ground between 180 and 250 m and connected to surface by an 18 m diameter shaft, ending directly onto the cavern vault, as shown in Fig. 39. The choice of the cavern dimensions has been driven by the size of the FCC-hh detectors,

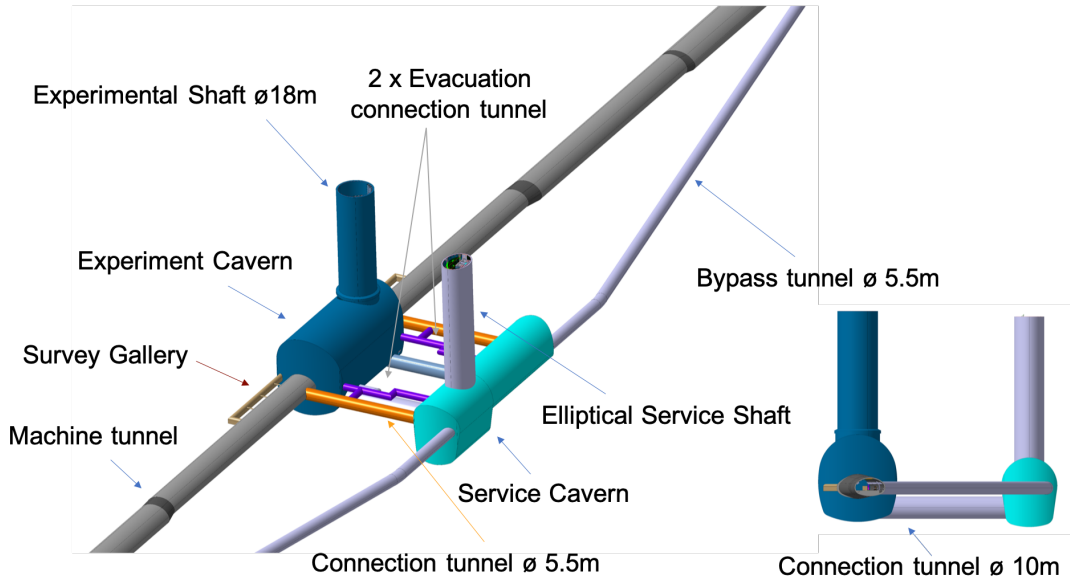


Fig. 39: Cavern infrastructure

that are much larger and heavier than the FCC-ee ones. However, this poses the problem of the beam height inside the experiment cavern, as the baseline height of 12 m from cavern floor is excessive for both the FCC-ee detector and machine elements, as the mechanical stability of the FFQs and the whole detector would become critical. The beam height has been consequently reduced to 9 m inside the small experiment caverns and it shall be raised to the same level in the large caverns by adding a temporary flooring structure that will be then dismantled when the FCC-ee physics program will be over.

A general purpose detector for FCC-ee would have a diameter of about 12 m and the same length. The largest object that has to pass through the cavern shaft is the detector magnet cryostat, approximately 7 m in diameter and length (or smaller, in some detector proposals, where the hadronic calorimeter is external to the detector solenoid). To get access to the internal sub-detectors, the two endcaps at the extremities have to be opened by a distance at least equal to the length of the longest internal sub-

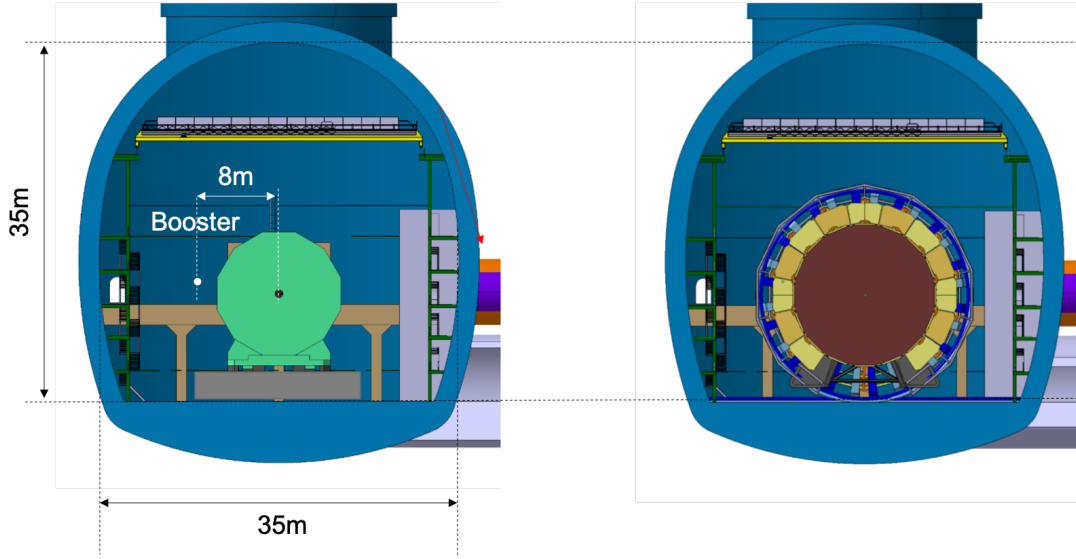


Fig. 40: An FCC-ee detector (left) and the FCC-hh reference detector (right) in a large cavern of 35 m \times 35 m cross section.

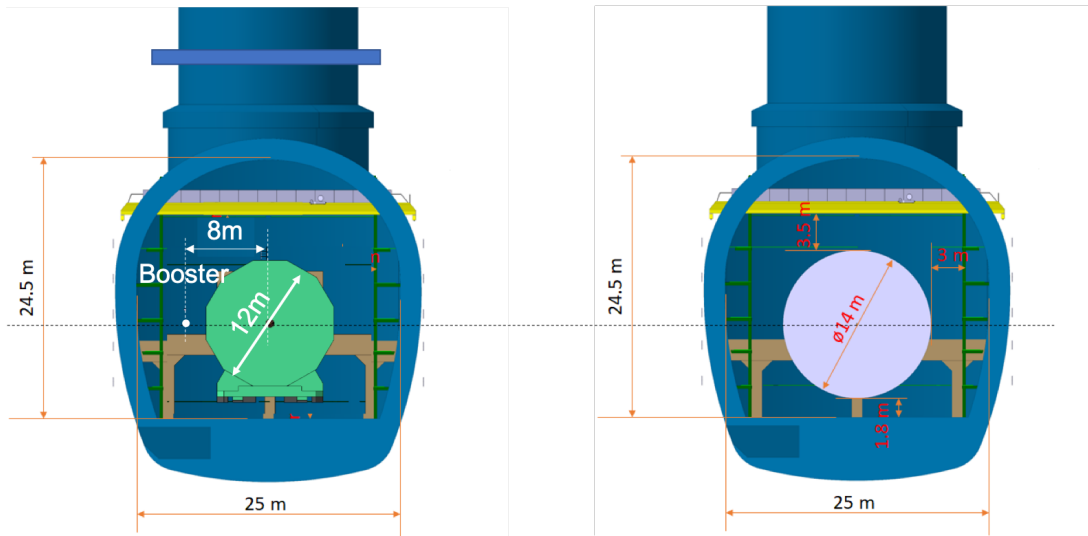


Fig. 41: An FCC-ee detector (left) and the FCC-hh reference detector (right) in a small cavern of 24.5 m \times 25 m cross section.

detector (i.e. about 5 meters, in almost all the detector proposals). Adding some margin, we can consider that an overall longitudinal stroke of the detector endcaps of 7 meters is good enough for getting access to the inside of the detector, including during the assembly operations at the time of its construction.

Periodic (or exceptional) detector maintenance requires, in general, access to the internal sub-systems, known as ‘opening the detector’. The design of the MDI region must carefully anticipate the intertwined requirements from the civil engineering, the machine, and the detector. Three opening scenarios, with their own advantages and drawbacks, have been examined.

1. In a first scenario, the two endcap calorimeters are moved along the z axis to disengage them from the barrel, as displayed in the left panel of Fig. 42, by a couple metres if only access to the central tracker is needed and by up to 7 m if the tube supporting the LumiCal, the vertex detector, and the central vacuum chamber requires extraction (and re-insertion). The mechanical stability of the

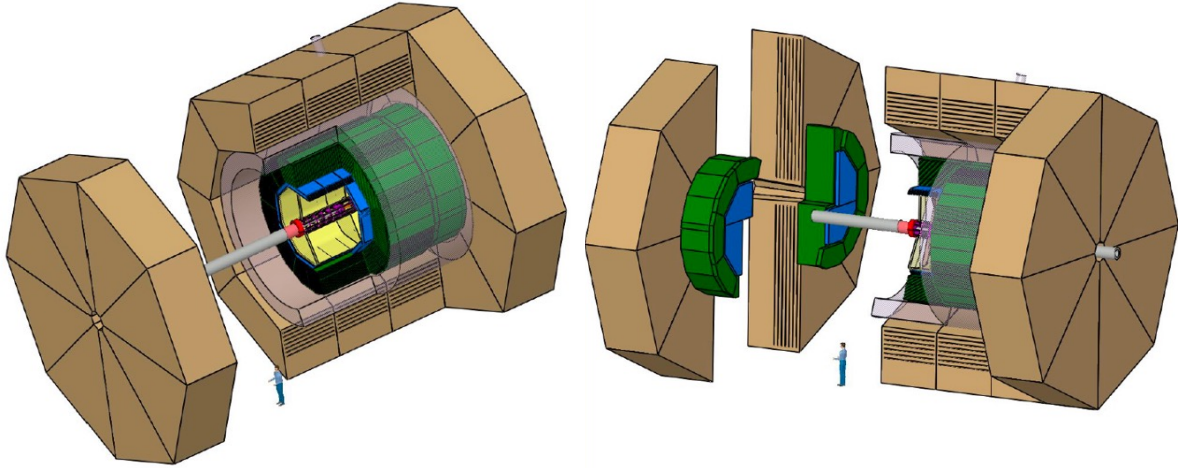


Fig. 42: Longitudinal (left) and short longitudinal plus transversal endcap (right) detector opening

final focus quadrupoles requires rigid supports, as close as possible to the detector boundaries. These supports, if fixed, would make the longitudinal opening of the detector endcaps impossible. Removable supports would then need to be designed to allow safe removal of the FFQs, and a quick re-installation and alignment following the access to the inner detectors. In this scenario, in addition to the re-alignment issue, the beam-pipe vacuum is broken. As the removal of the FFQs from inside the detector would first require the removal of other machine elements just behind them, this scenario can be envisaged only for medium or long machine shutdowns (several weeks or months), as done with the BELLE II detector at SuperKEKB.

2. A second option involves vertically splitting the detector endcaps, allowing opening without removing the FFQs. In this scenario, the two split endcaps are first moved longitudinally for about 2 m and then moved from the beamline in the transverse direction, as shown in the right panel of Fig. 42. The FFQs could stay cold, with the beam pipe under vacuum. This scenario could be very effective in the case of a quick access. The only constraint from the machine side is to keep all the services needed by the FFQs (supports, vacuum, cryogenics, powering) in the shadow of the FFQs, i.e., inside the detector forward acceptance cone. The main drawback is the serious impact on the detector acceptance, as splitting the endcaps creates a dead zone in the vertical plane and may imply a complete recalibration of the calorimeter angular acceptance determination.
3. A third, currently preferred, possibility consists of moving the complete detector along the x axis, away from the beamline, as shown in Fig. 43. As in the first scenario, this requires a disconnection of the internal FFQs from the rest of the machine, but allows them to be kept inside the detector. The FFQs can then be easily removed without touching any other machine element, before proceeding to a longitudinal opening of the endcaps without any obstacle. The detector integrity is preserved and, although the beam vacuum is broken and a re-alignment of the FFQs is needed, relatively short access periods (few weeks) can be envisioned. As the FCC-ee detectors have a diameter of typically 12 m, this scenario requires enough transverse free space on one side of the detector, which is currently not available in the two small experiment caverns. Another location for the balconies (in green on Fig. 41, may have to be found in these caverns, e.g., by placing all of them on the other side of the detector, and a small additional alcove (typically 25 m long and a few metres deep) might also be needed, depending on the exact transverse size of the detector. Designing the small caverns so that their axis can be transversely displaced from the beamline by a few metres, if compatible with the size of the specialised FCC-hh detectors, would alleviate the need for such an alcove.

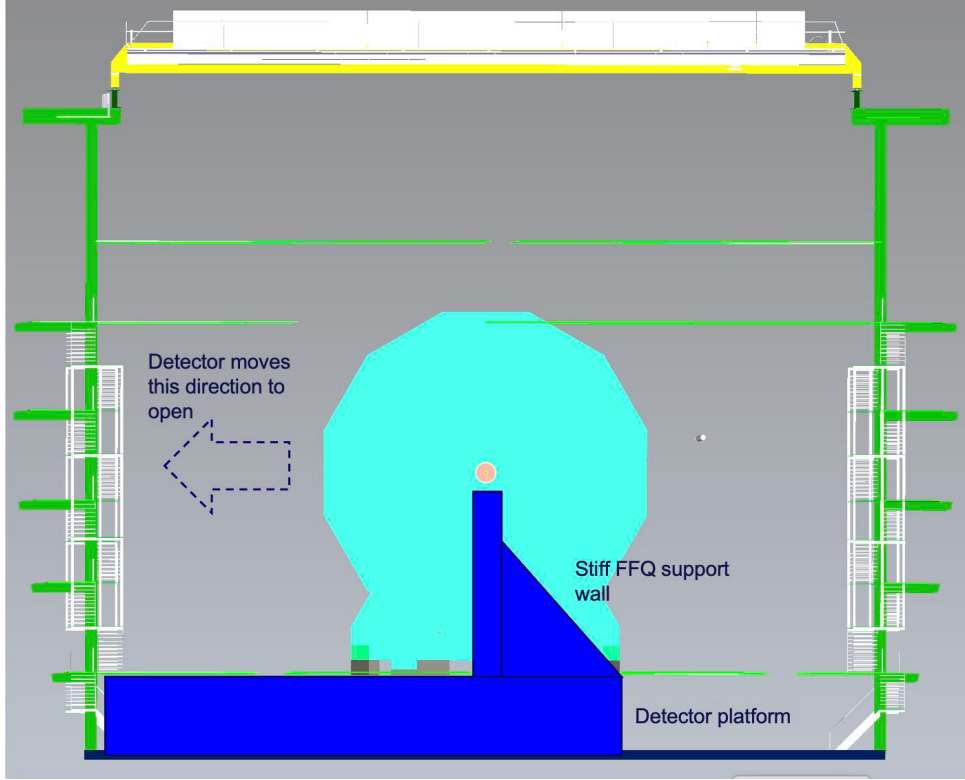


Fig. 43: Study for detector moving to garage position inside large cavern

Technical mitigation solutions for the drawbacks of these three scenarios will be investigated in detail during the next phase of the study.

5 Simulation of the vertex detector and machine elements

To perform simulations on the detector performance and background estimation, the turnkey software framework Key4hep [31] is used. The geometry of the detectors and the MDI region is described using DD4hep [32] format. Full simulations are performed using the Geant4 [33] based tool ddsim. The event data model used for the exchange among the different framework components is EDM4hep [34].

5.1 Geometry description of the MDI region in Key4hep

For the CDR studies, a parametric model of the beam pipe in the detector region was developed based on native shapes available in DD4hep. The current version of this model features the double layered AlBeMet central chamber with the paraffine cooling and the gold coating, and a conical chamber to reproduce the beam pipe separation region, and is shown in the left side of Fig. 44. In order to have a more accurate description of the beam pipe, the engineered CAD models described in Sec. 3.1 can be directly imported in DD4hep. The comparison of the two models is shown in Fig. 44. A major upgrade is represented by the beam pipe separation region, which is now congruent to the low-impedance design and the cooling manifolds. Also Tungsten Synchrotron Radiation (SR) masks located 2.1 m upstream the IP are included in this model. CAD models for other beam pipe elements, such as bellows, shielding and supports, will be added in the next phase of the study.

The experiment solenoidal magnetic field of the 2 T, the screening and compensating anti-solenoids are imported in the simulations via a field map, as shown in Fig. 45, which also takes into account the fringe effects.

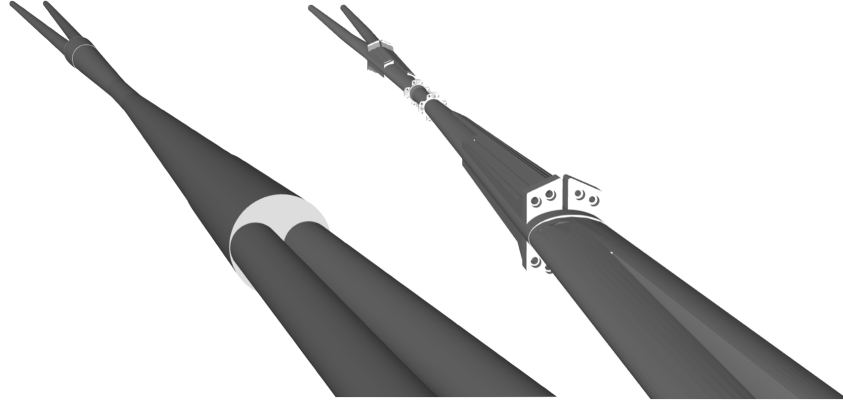


Fig. 44: Shape based (left) and CAD (right) models of the IR beam pipe in the simulation framework, with focus on the beam pipe separation region.

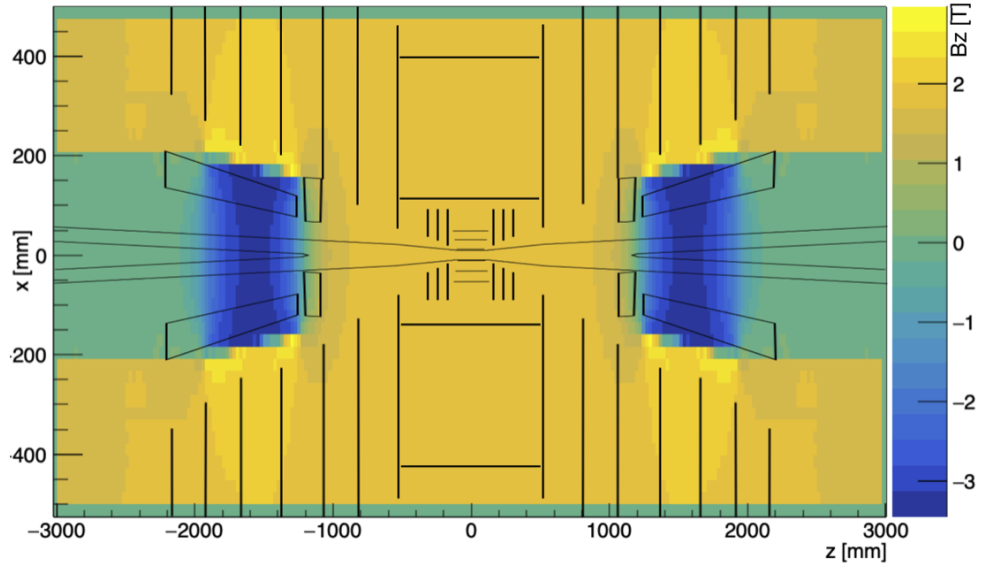


Fig. 45: Map of the magnetic fields in the MDI region used in the Key4hep simulations.

Figure 46 shows the other MDI elements present in the Key4hep model. The Final Focus Quadrupoles (FFQs) are represented by a simple model composed of equivalent material, and their magnetic field is defined according to the latest optics in MAD-X [35]. A detailed description of the FCC-ee LumiCal is also included. Cryostats for the anti-solenoids have been integrated into the model as 2 cm thick hollow cylinders.

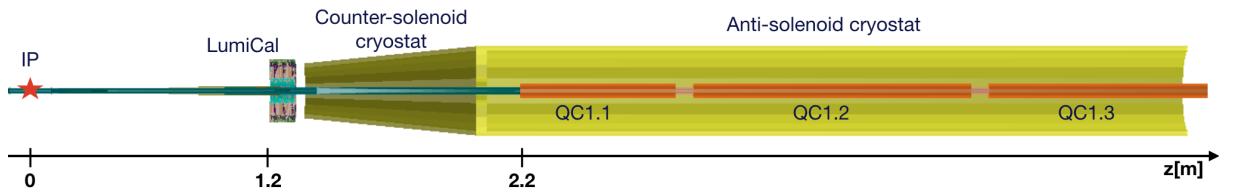


Fig. 46: LumiCal, final focus quadrupoles and cryostats for the antisolenoids as in the DD4hep geometry description.

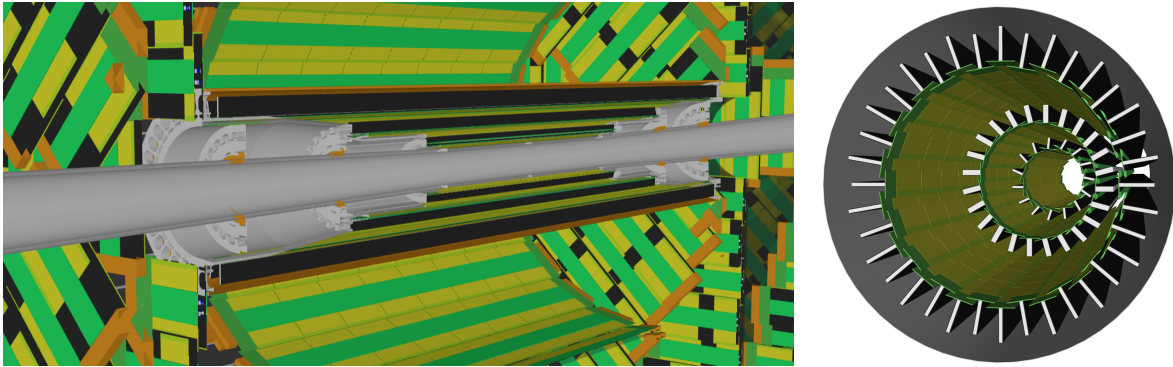
5.2 Baseline vertex detector simulation model

The IDEA vertex detector was previously implemented in native Geant4 enabling full simulation of the detector [36,37], but is now ported/re-implemented in Key4hep. The implementation of the silicon-based vertexing and tracking detector of IDEA in DD4hep has started in 2022 and now features an accurate representation of the engineered IDEA vertex detector discussed in Sec.3.4.

The vertex detector is assembled using two newly written builders hosted in k4geo³.

The staves in the vertex detector are made up of silicon sensors, support structures and readout elements, all described by simple rectangular cuboids. The silicon sensors consist of sensitive and insensitive elements to describe the sensors and their passive periphery. The insensitive volumes have an associated material (i.e. silicon), but do not generate hits. Both the dual ARCADIA sensors in the vertex inner barrel and the ATLASPix3 quad modules in the vertex outer barrel and disks have an accurate periphery description. The readout flexes and ladder supports are implemented by one box for each layer of material.

In the vertex inner barrel, the support structure is described by boxes of carbon fibre and Rohacell, with a reduced density (66% of nominal) to account for the lightweight mode of construction. Outside of the inner vertex is a 200 μm thick carbon fibre wall to steer the airflow of the outermost layer. The resulting geometry is shown in Fig. 47a. The conical support of the vertex inner barrel and the cooling cones are imported from a CAD file directly using the DD4hep package DDCAD [32]. The conical support can be seen in Fig. 47b closing off the vertex inner barrel. They are both, however, not yet considered in the material budget estimation, but will contribute mostly outside acceptance.



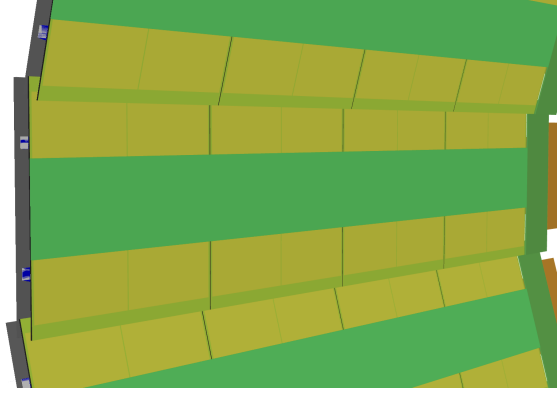
(a) Longitudinal sectional view of inner vertex with conical support. (b) Without conical support and cooling cones

Fig. 47: IDEA vertex inner barrel geometry in Key4hep.

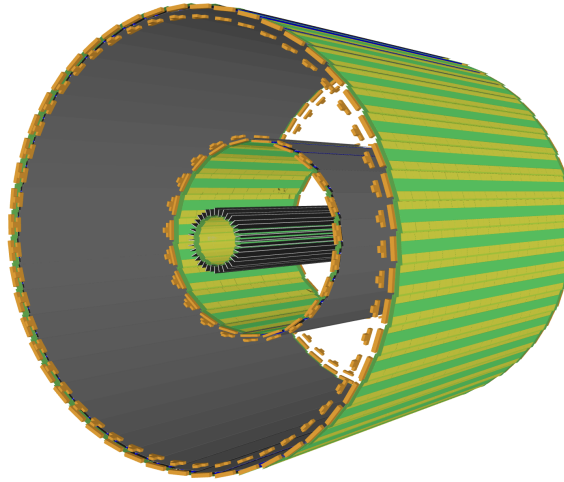
For the vertex outer barrel, the material budget contribution of the light-weight truss structure giving structural integrity to the staves is taken into account by a proxy layer of carbon fibre. The thickness of this layer is 500 and 480 μm for the middle and the outer tracker respectively. The geometry description also contains placeholder structures to represent the cooling pipes that go along the stave and the contained water, which can be seen in blue in Fig. 48, together with the truss structure proxy just outside of the stave. Parts of the cold plate and the hybrid circuit at the end of the staves are not yet implemented however.

The vertex disks have the most complex geometry. Staves similar to the vertex outer barrel make up eight petals in ϕ . Also here cooling pipes are added and the flex and support structures are placed below the silicon sensors. The global disk support structures made of Rohacell and carbon fibre are approximated by proxy cylindrical volumes with thicknesses of ≈ 2.5 mm for each disk layer (6 mm in

³<https://github.com/key4hep/k4geo>



(a) Close-up of middle vertex barrel, sectional view at $z = 0$



(b) Complete outer vertex barrel with inner vertex inside

Fig. 48: IDEA vertex outer barrel geometry in Key4hep.

CAD design, but with holes). The vertex disk geometry can be seen in Fig. 49.

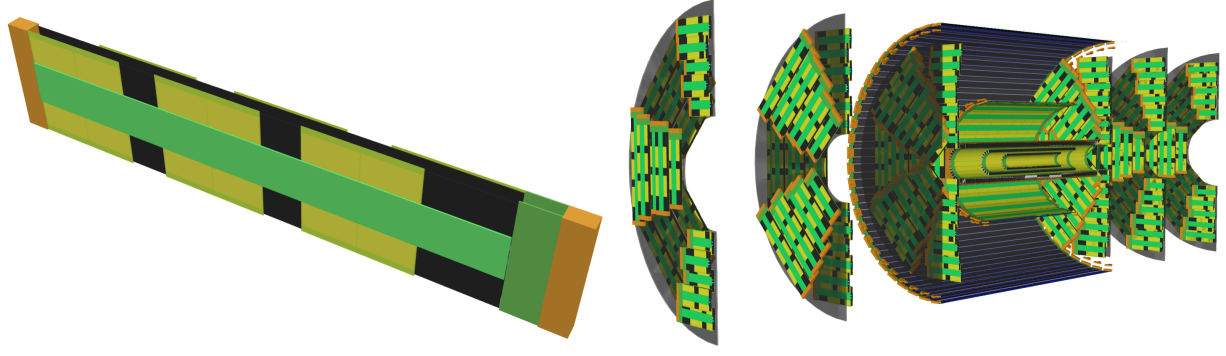
The off-detector services going from the staves and disks out of the detector are not designed yet and therefore also not included yet in the vertex detector description in Key4hep.

Fig. 50 shows the locations of the sensitive elements of the complete IDEA vertex detector in $z-r$ and $x-y$. ALLEGRO currently foresees the same vertex detector design as IDEA.

6 Beam-induced backgrounds

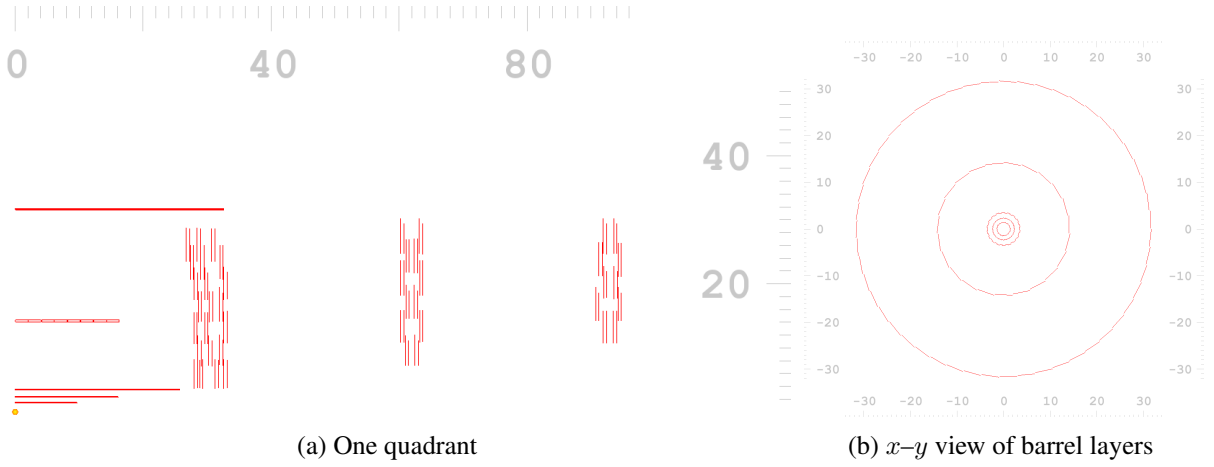
The beam-induced backgrounds in the detectors and IR machine elements, such as the FFQs, arise from two categories of sources: those generated by processes involving only a single beam, and those generated by the beam interactions at each IP, known as luminosity backgrounds.

This section describes the sources and the effects on both the detector and on the machine elements of the IR. Most of the backgrounds have been studied for the Z peak mode of operation, which has the largest intensity.



(a) One stave with three ATLASPix3 modules on both sides (b) Longitudinal sectional view of disks integrated into complete vertex system

Fig. 49: IDEA disks geometry in Key4hep.



(a) One quadrant

(b) x - y view of barrel layers

Fig. 50: Layout of IDEA vertex detector in Key4hep. Units at the sides are in millimeters.

6.1 Synchrotron Radiation backgrounds

Synchrotron radiation is emitted by relativistic charged particles as they are accelerated. To manage this radiation, the lattice design upstream of the Interaction Point (IP) features weak dipoles and a long straight section where a synchrotron radiation collimation system, utilizing tungsten-based collimators and masks, has been specifically designed and optimized. This system effectively manages the heat load and prevents photons from reaching the central chamber.

Besides, synchrotron radiation emitted by the combination of the detector solenoid and anti-solenoid produces numerous photons directed toward the next bent section downstream of the IP. This area requires careful attention since other sources, such as beamstrahlung, also converge at the same location.

In the 45.6 GeV energy mode, the highest beam current generates a significant amount of relatively low-energy photons, making the power deposited a crucial parameter to assess the cooling requirements for the beam pipe. Synchrotron radiation from the beam core, represented in blue in Fig. 51, delivers less than a Watt of power deposition in the detector beam pipe, at Z, and close to zero at tt, with most of the radiation from upstream of the IP contained in the SR collimation or propagating through the central chamber.

A more precise power deposition, presented in Fig. 51b, demonstrates that the mask effectively

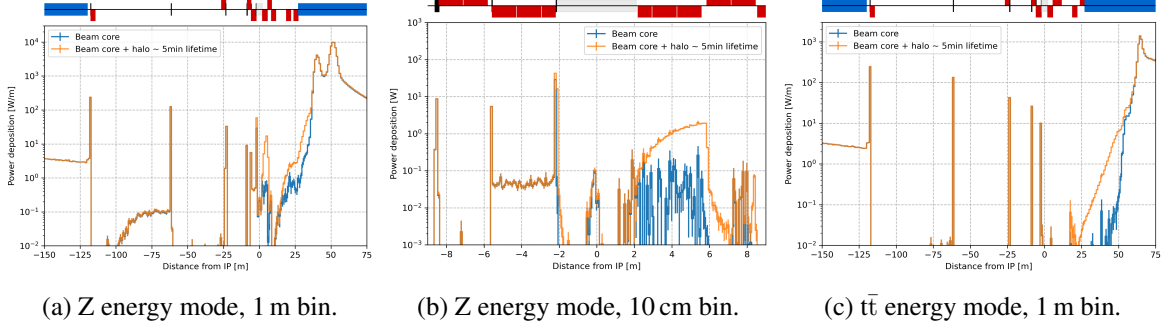


Fig. 51: Synchrotron radiation power deposition including collimators and masks.

intercepts radiation that would otherwise impact the central chamber. Synchrotron radiation from the beam tails mainly increases the power deposition beyond 2 m from the IP. The power deposition by synchrotron radiation around the IP is estimated to be smaller than the beam heat load coming from the wakefields. Further studies will include X-ray reflection, recently implemented as a standard process in GEANT4 [38], into the model considered.

While the beamline incoming to the IP does not feature significant bending, the outgoing one is strongly bent to accommodate the 15 mrad half-crossing angle. This implies a much higher production of synchrotron radiation downstream of the IP, amounting to more than 60 kW already within the first 250 m [39]. Even though it does not represent a concern for the experiment, it contributes significantly to the radiation levels in the tunnel around the IP. Photon stoppers in CuCrZr are installed along the beamline as in the arcs to avoid direct impact of the synchrotron radiation photons on the vacuum chamber and reduce the radiation levels. The Monte Carlo code FLUKA [40–42] is used to compute the power deposition into the photon stoppers from the synchrotron radiation and the resulting total ionising dose (TID) in the tunnel, for the two operation modes at pole and $t\bar{t}$ threshold.

6.2 Beam halo losses

During operation, a variety of processes such as space-charge effects, interaction with residual gas, intra-beam scattering, Touschek scattering, laser-beam inverse Compton scattering for intensity control, magnet misalignment, and magnetic field errors can lead to the population of the beam halo, potentially leading to beam losses. In high-intensity machines, such as the FCC-ee, beam halo losses must be safely disposed to avoid damage to sensitive equipment and keep the background level in the detectors below tolerable levels. For these reasons, a beam halo collimation system is being designed and optimized [43–49]. Multi-particle tracking studies have been performed to evaluate the effectiveness of the halo collimation system in suppressing beam halo losses on sensitive machine equipment and in the interaction regions (IRs). The first focus was on the FCC-ee Z operation mode, as it is the most challenging from the collimation point of view given the highest stored beam energy of 17.5 MJ. The studies have been performed using the Xsuite-BDSIM simulation tool [50–53], which combines particle tracking in the FCC-ee magnetic lattice, performed with Xsuite [54], and full Monte Carlo particle-matter interaction simulations in the collimators, performed with BDSIM based on GEANT4 [33, 55–58]. In these studies, a number of macroparticles, typically 5×10^6 , are tracked through the full FCC-ee nonlinear lattice for 500 machine turns, including the effects of synchrotron radiation (SR), RF cavities and magnetic lattice tapering. For simulation performance, only a beam halo slice impacting directly on one of the primary beam halo collimators is simulated, with a maximum impact parameter (i.e., the transverse depth into the collimator jaw) of 1 μm . The initial mechanism causing the loss is not simulated – as in LHC studies [59]. The beam loss positions are recorded, and their distribution along the longitudinal coordinate s is binned in 10 cm intervals to produce loss maps showing the beam loss distribution along the collider ring. The loss map for the FCC-ee positron beam (B1) for the region spanning from -700 m

upstream of IPD to IPD is reported in Fig. 52 for horizontal betatron halo collimation losses. The power load values are assessed assuming a lifetime drop to 5 min, corresponding to 58.3 kW of loss power. This is assumed as a design specification that the halo collimation system should be able to handle. The interaction point IPD, the farthest from the collimation insertion located in PF, is highlighted because it is the most exposed to beam halo losses.

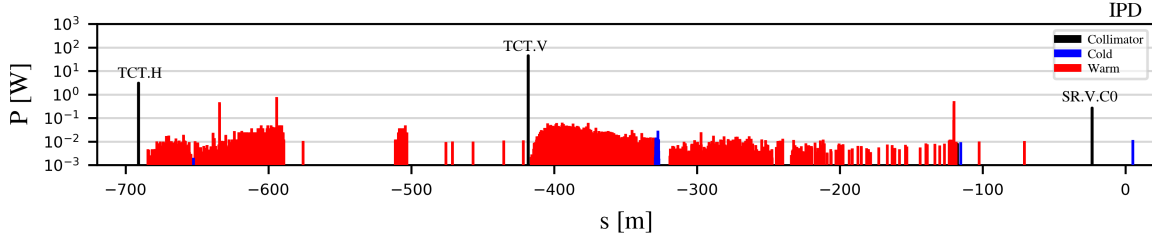


Fig. 52: Power load distribution loss map for beam halo losses of the FCC-ee positron beam, illustrating horizontal betatron losses in the region spanning from -700 m upstream of IPD to IPD. Power loads are evaluated assuming a beam lifetime drop to 5 min. The beam circulates from left to right.

The loss map in Fig. 52 shows that the majority of the beam halo losses in the MDI are intercepted by the tertiary local protection collimators (TCTs), which are placed at -690 m (TCT.H) and -420 m (TCT.V) from each of the interaction points. Their location has been selected such that the phase-advance is optimal (multiple of π) to protect the aperture bottlenecks at the FFQs and the SR collimators, which are primarily designed to reduce the photon background from SR emission rather than absorb beam losses. A small fraction of losses is observed on the elements downstream of the TCTs, with approximately $O(100 \text{ mW})$ on the SR collimators and around $O(10 \text{ mW})$ on other downstream components. The background contribution from particle showers arising from the interaction of beam halo particles with the TCTs and SR collimators remains to be evaluated. Lastly, it is worth to mention that the collimation performance can be further enhanced by angularly aligning the collimator jaws to the beam divergence at the collimator locations [46, 47]. The larger the beam divergence, the higher is the obtained performance gain.

6.3 Beam gas scattering

The interactions between the beam and the residual gas in the vacuum chamber can lead to a degradation of the beam quality. The beam lifetime and the luminosity may be reduced, the beam emittance may increase, and distinct beam loss distributions can be produced, potentially leading to unwanted beam-gas-induced backgrounds in the experimental interaction regions (IRs). The interactions the beam particles undergo depend on the beam particle type and on the residual gas atom/molecule considered. In the FCC-ee, the beam particles are multi-GeV electrons and positrons. Therefore, the lifetime reduction and beam quality degradation due to beam-gas interactions are primarily caused by inelastic interactions, specifically bremsstrahlung interactions. While elastic interactions like single Coulomb scattering also occur, their effect on the beam is minimal at the FCC-ee beam energies compared to that of bremsstrahlung. Dedicated vacuum studies provided the residual gas pressure profile in the FCC-ee Z. The assumed gas species are hydrogen H_2 , carbon monoxide CO and carbon dioxide CO_2 , with composition 85% H_2 , 10% CO and 5% CO_2 (the typical gas composition measured in light sources). To simulate the interaction of the beam with the residual gas, 10000 beam-gas scattering centers are included in the tracking [60], performed with the Xsuite-BDSIM simulation setup introduced in Sec. 6.2, and 10×10^6 primary particles are tracked for 17×10^6 equivalent turns in the full FCC-ee Z nonlinear lattice with SR, RF cavities and magnet tapering enabled.

The loss map in Fig. 53 shows the power load distribution from beam-gas losses, normalized to

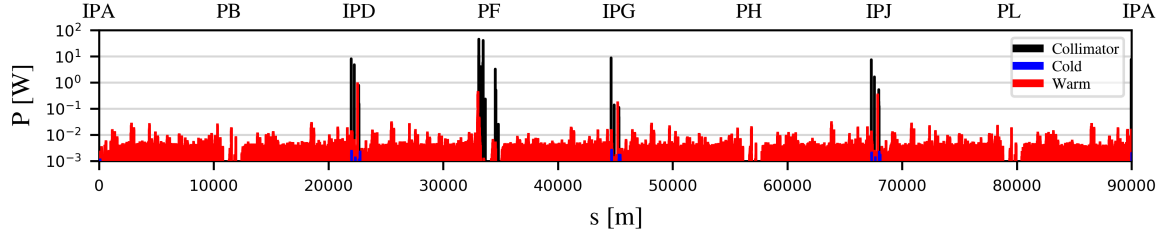


Fig. 53: Power load distribution loss map for beam-gas beam losses of the FCC-ee positron beam. The beam circulates from left to right. The power loads are evaluated considering a 5 h lifetime resulting from the expected pressure after 1 h of beam conditioning at full nominal current of 1.27 A.

a beam-gas lifetime of 5 h that results from the expected pressure after 1 h of beam conditioning at full nominal current of 1.27 A. This pessimistic scenario represents the start of FCC-ee operation, and the pressure is expected to condition down by a factor of up to 100 over time. Consequently, beam-gas interactions are unlikely to significantly affect the lifetime of the FCC-ee, which is primarily determined by Bhabha scattering at the IPs. Even in this pessimistic scenario, low power loads (<0.1 W) are expected on most components, with the highest loads recorded on the halo collimators (10-100 W) and SR collimators (1 W). Such power load levels are not a concern. Only minimal power loads are found in the MDI region, as shown more evidently in the IPD loss map in Fig. 54. Therefore, the background contribution from beam-gas beam losses is presently not expected to be an issue. Nevertheless, the background contribution from particle showers arising from the interaction of beam-gas scattered particles with the TCTs and SR collimators might not be negligible and should be studied in the future.

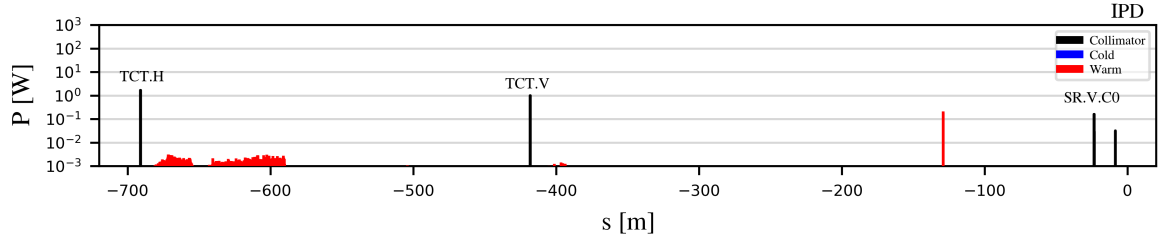


Fig. 54: Power load distribution loss map for beam-gas beam losses of the FCC-ee positron beam, illustrating beam-gas beam losses in the region spanning from -700 m upstream of IPD to IPD. The beam circulates from left to right. The power loads are evaluated considering a 5 h lifetime resulting from the expected pressure after 1 h of beam conditioning at full nominal current of 1.27 A.

6.4 Thermal photons

Even a perfectly evacuated beam pipe remains "filled" with photons from black body radiation which can be relevant as source of backgrounds and reduction of beam lifetime as first pointed out by V. Telnov in 1987 [61]. The photon density from black-body radiation is

$$\rho_{\gamma} = 8\pi \left(\frac{kT}{hc} \right)^3 \underbrace{\int_0^{\infty} \frac{x^2}{e^x - 1} dx}_{= 2.404} \quad (1)$$

where T is the absolute temperature, and k, h, c the Boltzmann, Planck constants and the speed of light. For a beam pipe at room temperature (23°C), we get a photon density of $\rho_{\gamma} = 5.3 \times 10^{14} \text{m}^{-3}$ which

is an order of magnitude higher than the typical residual gas molecular densities ρ_m , considered in this chapter for beam gas estimates.

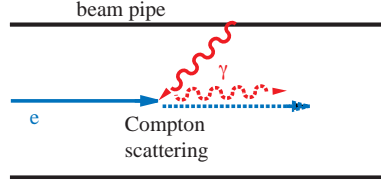


Fig. 55: Schematic view of the inverse Compton scattering with thermal photons. A high energy beam particle collides and loses energy to a low energy photon radiated from the beam pipe by black body radiation.

The lifetime from thermal photon scattering is

$$\tau_t = \frac{1}{\underbrace{\rho_\gamma c \sigma_C}_{\sim 26 h}} \frac{1}{f_{\text{loss}}} \quad (2)$$

where ρ_γ is the photon density, σ_C the Compton cross section (at high energy ~ 0.665 barn) and f_{loss} the fraction of the e^\pm lost after collision. At the high-energies relevant for FCC, the scattering angles are small compared to the beam divergence. Beam particles are get lost, if the energy loss in the scattering process exceeds the energy acceptance of the machine. Depending on lattice and collimation details, particles with an energy loss of some percent produced around the ring can get lost locally in low beta insertions similar to the off-momentum backgrounds from beam-gas scattering in the experiments. Numerical values calculated using the program described in [62] are given in Tab. 12. We can see that thermal photon scattering at room temperature becomes only relevant for electron beam energies above 10 GeV.

Table 12: Thermal photon scattering. Single beam lifetime from loss by thermal photon scattering for different beam energies E_b , at room temperature and for an energy acceptance of 2%.

E_b in GeV	τ_t in hours
10	9000
45.6	144
80	83
120	64
182.5	54

6.5 Fast Instability

Previous studies on collective effects in FCC-ee have shown that the resistive wall impedance in the FCC-ee can lead to fast rise-time instabilities, where the amplitude of the betatron oscillation of the beam grows exponentially with time, leading to fast beam loss within a few turns across the ring. A feedback system is under development to avoid the raising of this instability by damping the amplitude, however the failure scenarios of this feedback system need to be explored. The fast instability scenario assumes the failure of the feedback system which lead to a coherent oscillation of the beam. The amplitude of the oscillations will growth exponentially with time, with a characteristic time called rise time τ .

The value of the rise time is strongly dependent on the impedance model, the most recent simulations estimate a rise time between 3 and 10 turns. The collimation system must protect the machine/detectors even in the worst case scenario of a rise time of 3 turns.

To ensure the performance of the collimation system, simulations of the feedback system failure scenarios have been performed, producing beam loss distributions along the ring and across turns also called lossmaps.

The simulations have been conducted using the simulation package Xsuite in combination with the scattering routines in the BDSIM library, which provides an interface between Xsuite and GEANT4, to simulate losses along the ring. The tracking of the particle through the ring optics is performed using XSuite while the interaction of the beam within collimators and masks placed along the ring is studied using BDSIM.

The instability is generated ‘artificially’ through eight synchronized dipole kickers, one per arc. This setup allows to reproduce a smooth exponential growth of the betatron oscillation amplitude, either in the vertical or horizontal plane. The model does not include impedance model as well as single-bunch and multi-bunch interactions, which are performed within the collective effects group and produce the estimate for the rise time.

The kicker strengths are defined such as:

$$k = \frac{A_0}{\sigma_{x,y}} \cos(2\pi Q_{x,y}t) e^{\frac{t}{\tau}}, \quad (3)$$

where A_0 is an arbitrary chosen amplitude, $\sigma_{x,y}$ is the local beam size, $Q_{x,y}$ is the tune, and τ is the rise time of the instability. The value of A_0 is chosen to have an initial kick small enough to ensure a stable orbit for many turns before observing losses, the value of A_0 does not influence the typical time characteristics of the phenomena but only its starting point in time. In reality, the instability arises from the machine noise and the exact moment in which the instability starts in space and time cannot be predicted. The location of the kickers is calculated such that they are uniformly distributed in phase advance between 90° and 180° , this configuration leads to a more realistic representation in which the amplitude smoothly grows within one turn. Two main scenarios are studied, to better identify the limits of the collimation system for this scenario: a rise time of 3 turns (representing the worst case) and 6 turns. Since the instability can start at any location in the ring, the dependence on the phase advance was also analyzed. A total of 4 different phase advances between the first kicker and the primary collimator (TCP) have also been studied (0° , 30° , 60° , 90°).

Being the Z-mode the most critical scenario, with a stored beam energy of 17.5 MJ, for each configuration, 5×10^5 45.6 GeV primary electrons are simulated. The statistic has been chosen such that one particle hitting a collimator represent the estimate damage limit of 10% of one bunch. Synchrotron Radiation model, Radio Frequency cavity and magnet tapering are enable and a detailed aperture model as well as all the collimation systems are included in the simulation. To verify the performance of the model, the average centroid of the beam at the primary collimator is fitted with the expected amplitude growth, as shown in Fig. 56. To avoid the dependence on the phase, the normalized amplitude has been considered. The expected amplitude growth is estimated as:

$$A_{x,y}(\sigma) = \frac{\sqrt{2J_{x,y}\beta_{x,y}}}{\sigma_{x,y}}, \quad (4)$$

where $J_{x,y}$ is the beam action, β is the value of the beta function and σ is beam size; all the quantities are evaluated at the location of the primary collimator. The simulated beam is tracked until it is totally lost.

The instability induces the beam to oscillate coherently until the collimator apertures are reached, then it is entirely lost within a few turns. At the Z mode, this results in the release of 17.5 MJ on collimators over a few turns.

Figures 57 show the integrated lossmaps over all turns for both horizontal and vertical instability, in the specific configuration of $\tau = 3, 6$ turns and $\Delta\mu = 0$. Both cases show losses of the order of MJ at the collimation insertion as well as at the other IPs, due to the fact that the entire beam is lost within

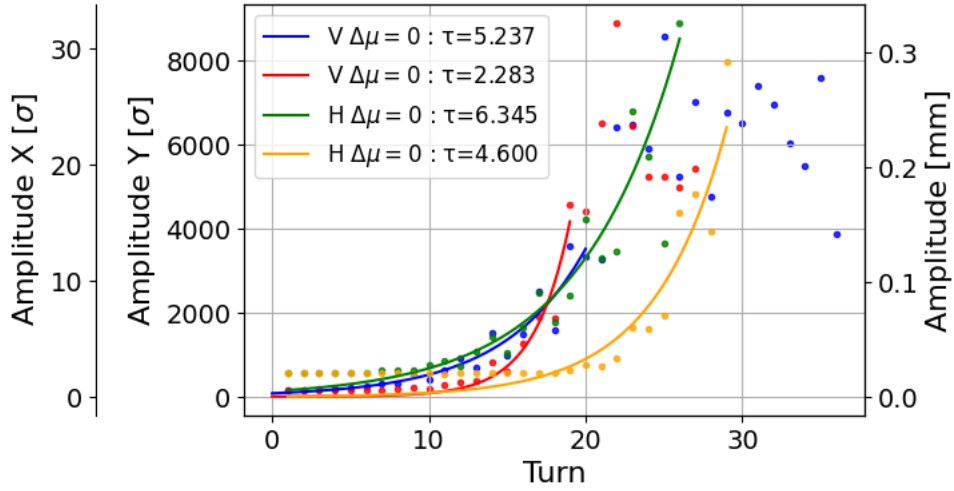


Fig. 56: Fit of the average centroid of the beam with the expected amplitude growth for a vertical or horizontal instability in the configurations $\tau = 3, 6$ and $\Delta\mu = 0$.

few turns. It is clear that the primary collimators are not absorbing most of the energy lost and since primary losses on tertiary collimator are observed the hierarchy is not always respected, therefore the collimation system is not efficient in this very fast scenario. The tertiary collimators efficiently protect SR collimators; to protect the detectors from possible particle showers, absorbers should be foreseen.

The integrated lossmaps don't give information about the time distribution of the losses, hence lossmaps for each turn have been produced and analyzed. Figures 58 show the fractions of energy lost on different type of collimators across turns, for different configuration.

The figures also show a turn in which, including losses in the aperture, up to 50% of the beam is lost. The time pattern of the losses is different in the two planes and for different rise time. An higher value of τ lead to a slower growth, therefore the losses are more spread in time. The vertical case shows losses more spread in time with respect to the horizontal case in the same setup, this is due to the fact that the beam reaches the dynamic aperture, around 30σ , before reaching the collimator aperture at 65σ causing a blow up. Also due to the small vertical emittance the first losses is usually already at MJ order, while most of the configuration with an horizontal instability present detectable losses before the peak loss turn. The rapid escalation of this effect put constrain in counter measures, in particular it's not efficient to relate on beam loss monitor since there could be no evidence of losses coming from this instability before a loss of the order of MJ. It is needed to introduce other mitigation system and detection system to observe this effect before any damage occurs.

To avoid the vertical blow up of the beam, the collimator apertures could be tighten up to the DA, however the current values of the β optics function would lead to apertures of fraction of millimeters and this would worsen the impedance estimate and therefore the fast instability itself. Preliminary results show that tightening the vertical collimators lead to losses focused more on primary collimators; an aperture of 35σ improves the collimation system performance, but does not prevent from the vertical blow up.

The instability shows also a dependence on the phase advance, for instance Fig. 59 shows the losses in the primary collimator across turns for an horizontal instability with $\tau = 6$ for the four different phase advances. The configuration $\Delta\mu = 0^\circ$ show that there could be cases in which the first loss in the collimator is already of the order of fraction of MJ.

Energy deposition studies are ongoing to assess the impact of this losses on the collimators. The vertical instability should represent the most dangerous case since the impact spot size are expected to

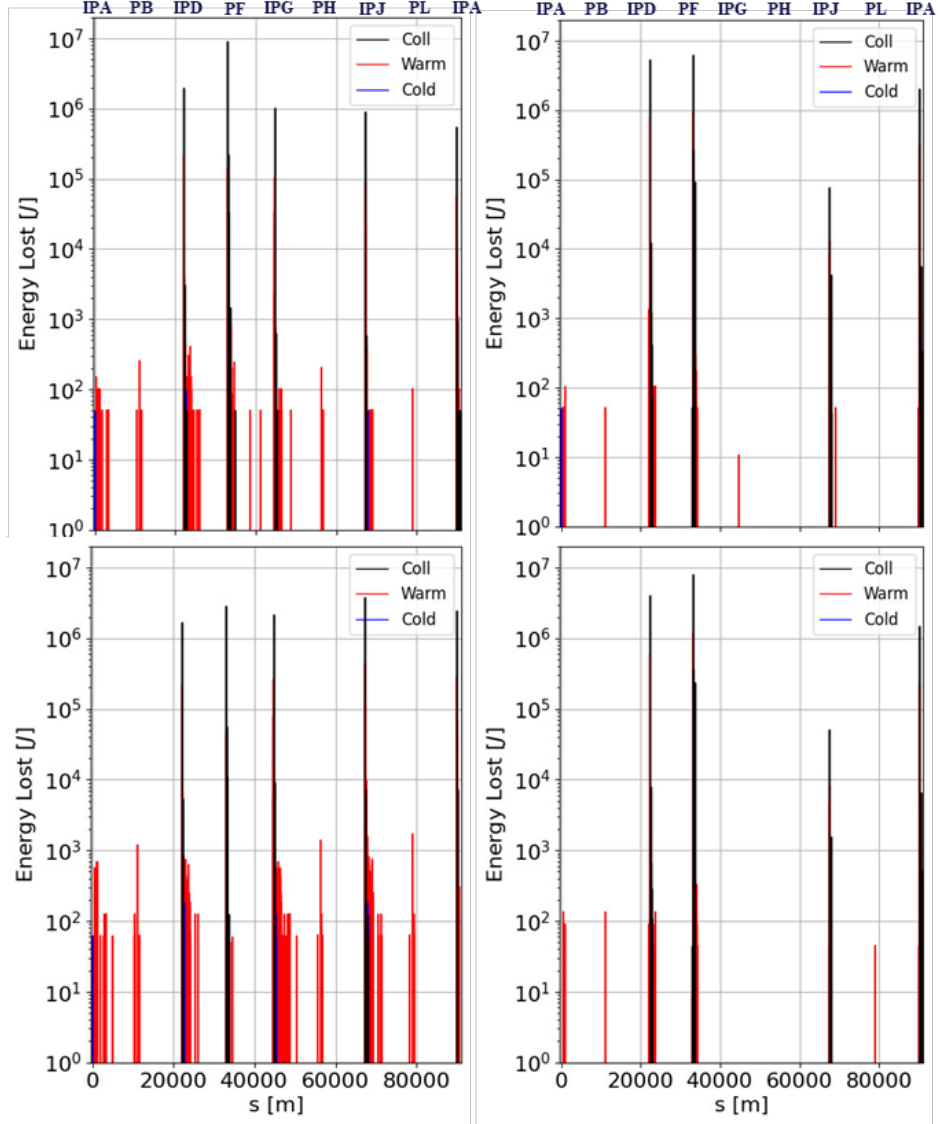


Fig. 57: Integrated lossmaps over all turns for for a vertical (right) or horizontal (left) instability in the configurations $\tau = 3$ (top) and $\tau = 6$ (bottom) $\Delta\mu = 0$.

be small, although the blow up lead to more broad impact distribution.

Finally, losses in the aperture are not negligible: 25% of the losses are spread across apertures for the horizontal instability, and 20% for the vertical instability.

6.6 Injection backgrounds

FCC-ee utilises a top-up injection system to maintain high luminosity by continuously replenishing beam particles in the main rings. This process, while essential, introduces injection backgrounds that can affect detector performance. Particles can be injected off-axis or off-momentum.

In the first case, with the off-axis scheme, the injected particles initially have large betatron oscillation amplitudes, causing them to deviate from the ideal orbit. As they stabilise, particles with excessive oscillations may collide with accelerator components, generating secondary particles that may contribute to losses and background in detectors. In addition, the injected beam can produce SR that has been simulated with BDSIM for the V22 lattice [63] both at the Z pole and $t\bar{t}$ energies.

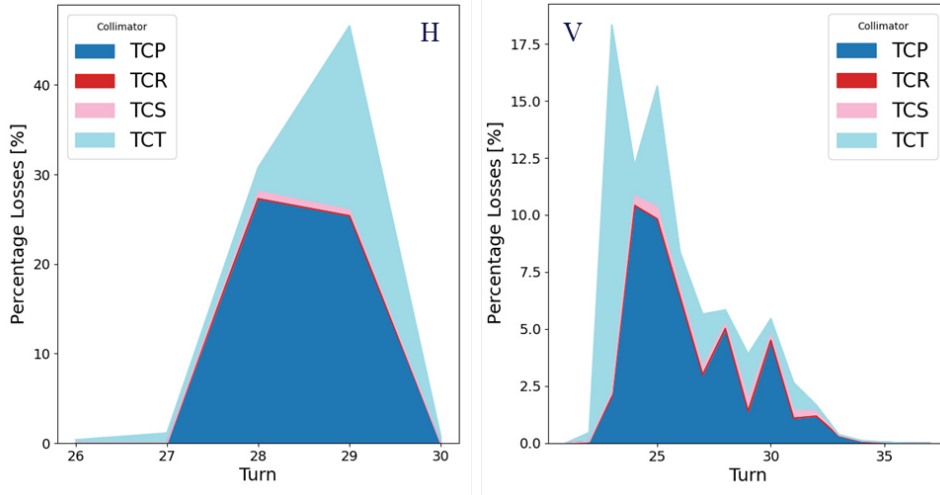


Fig. 58: Fractions of energy lost on different type of collimators across turns for an horizontal instability with $\tau = 3$ (right) and a vertical instability with $\tau = 6$ (left) both with $\Delta\mu = 0^\circ$.

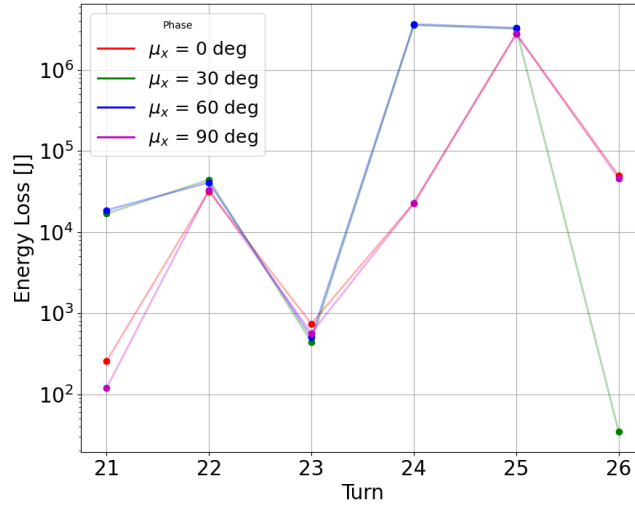


Fig. 59: Comparison of losses in primary collimator across turns for an horizontal instability with $\tau = 6$ for the four different phase advances.

In off-momentum injection, the injected particles are injected at a slightly different energy. This has potentially advantages : the energy offsets get damped faster than betatron offsets (by a factor of two when working with the standard damping partition $J_{x,y,e} = 1, 1, 2$). In the straight sections around the experiments where the dispersion is well corrected, the off-energy particles circulate on the same orbit as the stable beams.

With the settings presented in Ref. [63] the power deposited around the IR is about 10 W , whereas the region between 20 and 80 m beyond the IP the power deposited ranges between 100 and 1000 W. These power depositions are considered not sustainable and it is believed that the off-momentum scheme will be able to deliver smaller SR power depositions.

The injection scheme design is in progress and will be studied using the same tool as for the fast instability.

6.7 Radiative Bhabha events

During bunch crossings beam particles can lose energy via the Radiative Bhabha process:

$$e^+e^- \rightarrow e^+e^-\gamma \quad (5)$$

where the photon can be emitted either in the initial or final state. This can cause particles to exit the lattice acceptance already at the first quadrupoles. Radiative Bhabha events are produced with the generator BBBrem [64], and GuineaPig++ [65] is used to account for smearing and beam-beam effects. The off-energy particles are then tracked through the beam pipe to analyze power deposition on the downstream magnetic elements using FLUKA [40–42]. This is particularly important for the superconducting final focus quadrupoles, which risk to quench or be damaged by the cumulative radiation load. Studying the power deposition in their coils allows to assess the need of an internal shielding and, if necessary, dimension it.

This study has been done for two working points, namely the Z-pole and the $t\bar{t}$ threshold and for different optics lattices, V22, V23 and V24. An important parameter for the generation is the cutoff on the transferred momentum t between the interacting particles

$$t = \left(\frac{\hbar c}{d} \right)^2 \quad (6)$$

where d is the distance between the particles. Due to bunch dimensions and density effects, the interaction range is not infinite, and this may lead to an overestimate of the total Radiative Bhabha cross section (as was also observed in LEP [64]). We therefore apply a cut on t assuming as a critical distance the vertical bunch size $d_0 = \sigma_y$. The effect can be seen in Table 13, showing a reduction of the total cross section of about a factor 2 when considering this cutoff.

Table 13: Total cross section for the Radiative Bhabha process at FCCee, calculated for two lattices (V22 and V23), two working points (Z and $t\bar{t}$ (T)) and with/without the cutoff on the transferred momentum.

$E_0[GeV]$	Lattice	Cutoff		σ_{RB} [mbarn]		Luminosity/IP	
				$\delta > 3\%$	$\delta > 50\%$	$[cm^{-2}s^{-1}]$	$[ab^{-1}yr^{-1}]$
45.6 (Z)	v530 (V22)	—	—	226.4	32.9	1.82×10^{36}	20.9
		$1\sigma_y$	33.7 nm	112.1	18.2		
182.5 (T)	v530 (V22)	—	—	251.3	37.0	1.24×10^{34}	0.14
		$1\sigma_y$	69.0 nm	118.5	19.2		
45.6 (Z)	v572 (V23)	—	—	226.4	32.9	1.41×10^{36}	16.2
		$1\sigma_y$	36.5 nm	112.7	18.3		
182.5 (T)	v572 (V23)	—	—	251.3	37.0	1.38×10^{34}	0.16
		$1\sigma_y$	49.0 nm	115.4	18.7		

Another important parameter that can be set is the minimum energy of the emitted photon, or in other words the minimum energy lost by the particle. From preliminary tracking we have observed that particles produced with an energy offset $\delta > 50\%$ are mainly lost in the final focus quadrupoles region, while lowering this threshold to $\delta > 3\%$ the losses were distributed along the downstream arc. Table 13 shows the total cross section considering these thresholds.

6.8 Beamstrahlung

Due to the intense beam-beam during collision, the particles will emit synchrotron radiation in the electromagnetic field of the opposing beam. This process is known as beamstrahlung (BS). A detailed description and characterization of the beamstrahlung radiation at FCC-ee can be found in [6]. The generator used to study this process is GuineaPig++ [65].

Figure 60 shows the photon flux per unit of bandwidth at the four FCC-ee working points for lattice v530, and Table 14 reports the total power and the mean photon energy of this radiation. It can be observed that the power carried by this radiation is of the order of few hundreds of KW, with maximum value at the Z-pole where we have the highest beam currents.

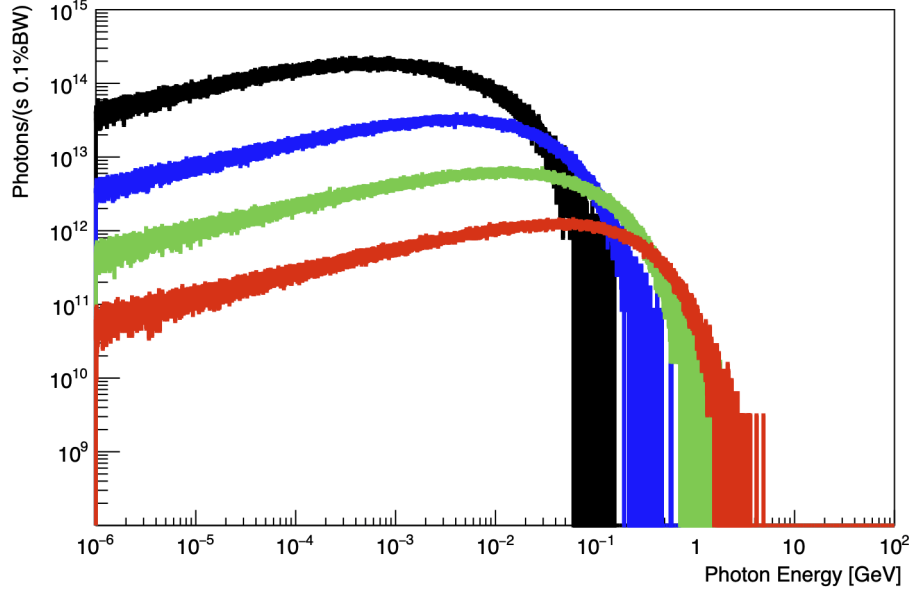


Fig. 60: Flux of the BS radiation as a function of their energy, emitted for the four FCC-ee working points, 45.6 GeV (black), 80.0 GeV (blue), 120.0 GeV (green), and 182.5 GeV (red).

	Tot Power [kW]	$\langle E_\gamma \rangle$ [MeV]
Z	370	1.7
WW	236	7.2
ZH	147	22.9
T	77	62.3

Table 14: Total power and mean photon energy for BS radiation at the four FCC-ee working points (lattice v530)

The aperture of the emission cone is very narrow, as it is inversely proportional to the energy of the emitting particles. Therefore, BS causes two high-power photon beams to exit each IP directed as the outgoing beams. Fig. 61 shows the path of the BS radiation with respect to the downstream beam pipe. The power carried by these photon beams must be disposed of in dedicated dumps located 500 m downstream [6], where they are led through extraction lines detaching from the beamline. FLUKA [40–42] is used to estimate the total power absorption and the power deposition profiles that the dump must withstand, as well as the radiation levels in its proximity. These results have served as basis to start with the conceptual design of the beam dump core and dimension its shielding.

The characteristics of the BS radiation are strongly related to the beam-beam effects, therefore on the beam parameters during collision. Figure 62 shows the total power emitted as a function of the relative offset between the colliding bunches. It can be seen that the power can increase up to a factor 2 due to the vertical offset. Such effect needs to be taken into account for the design of the photon beam bump, and it is under investigation the possibility to exploit this radiation for beam diagnostics. Also the effect of other non-ideal collisions (e.g. waist shift, dispersion, ...) is under study.

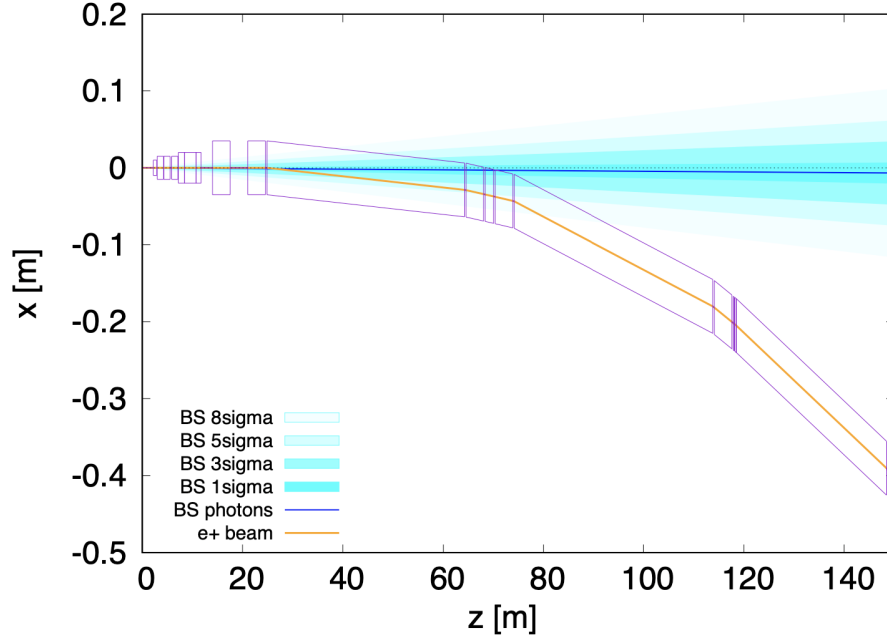


Fig. 61: BS photons path on the x-z plane with respect to the downstream vacuum chamber for the Z-pole c.o.m. energy.

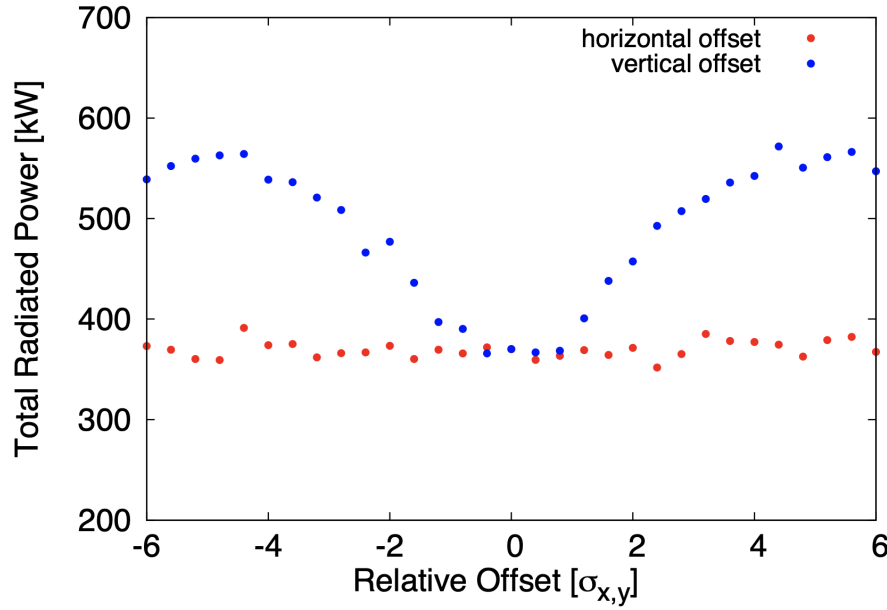


Fig. 62: Total power radiated via BS as a function of the relative horizontal (red) and vertical (blue) offset between the bunches.

Beamsstrahlung monitoring system

There is an interest in monitoring the ultra-intense Beamsstrahlung photon flux transported by the dedicated extraction lines to the dumps. The most relevant parameters are the photon profile position and intensity. This would provide a way for a ultra-precise IP tuning in the 200 nm beam to beam separation range.

6.9 Incoherent pairs creation

Incoherent Pairs Creation (IPC) is a main source of luminosity backgrounds at FCC-ee [66]. It consists in secondary e^-e^+ pairs produced via the interaction of the beamstrahlung photons with real or virtual photons during bunch crossing. Figure 63 shows the diagrams for the possible channels involved in the IPC. This process has been simulated using the generator GuineaPig++ [65], considering two Gaussian beams with the nominal beam parameters and applying no cuts on the produced particles minimum energy.

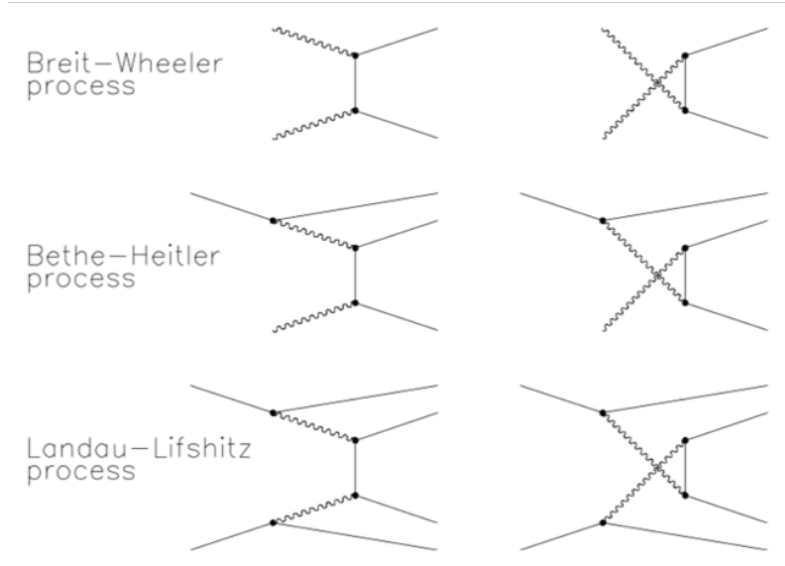


Fig. 63: Possible channels for the Incoherent Pairs Creation.

Figure 64 shows the production kinematics of these particles for the Z and $t\bar{t}$ working points at FCC-ee in the detector reference frame. The high p_T peak at $\theta = 0.015$ mrad corresponds to particles going in the downstream beam pipe. The different families in θ that can be observed at lower p_T are due to the focusing/defocusing effect caused by the beams on the particles (e.g. an electron produced in the direction of the downstream positron beam will experience a focusing effect).

The acceptance of the vertex detector (VXD) is also shown on Fig. 64 in red, considering $\theta > 140$ mrad and $p_T > 4$ MeV (for a 2T detector field and 13mm of first layer barrel inner radius). Only a small fraction of the total particles produced is inside this area. Due to the different production kinematics, this area is more populated at higher energy working points.

Table 15 shows the average number of pairs produced per bunch crossing at the four FCC-ee working points considering the beam parameters for lattice V22. These values slightly vary with different iterations of the optics. While the number of particles produced increases at higher center of mass energies, for the estimate of background induced in the detectors also the bunch crossing rate is relevant. As the bunch spacing is only 30 ns at the Z-pole, this is the most critical point to study for this background assessment. The induced occupancy per bunch crossing increases with the beam energy, due to the cross-section increase with energy [65], and of the harder p_T spectrum of the particles produced inside the detector acceptance. However, since the bunch spacing at higher energies is larger, the impact of the IPC is smaller than at the Z-pole.

The incoherent pair-production beam background drives the occupancy in the vertex detector. A first study in 2022 [67], using the CLD detector concept and old lattice with 30 ns average bunch crossing, led to 1300 e^+e^- pairs per bunch crossing at the Z pole. Given the $25 \times 25 \mu\text{m}^2$ pixel size and assuming a safety factor of 3 and a very conservative cluster size of 5 per hit, this leads to a maximal occupancy of 70×10^{-6} in the first vertex barrel layer. Expressed as a total hit rate, this is about 370 MHz/cm². A

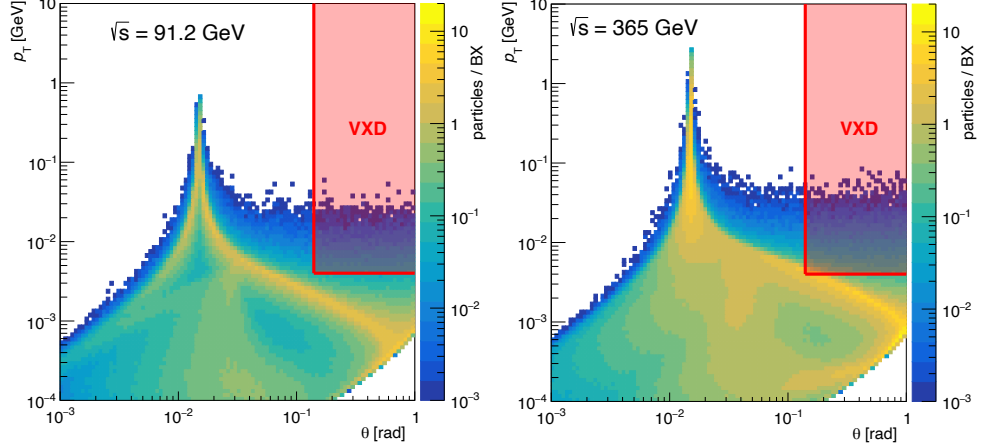


Fig. 64: Number of IPC particles produced for each FCC-ee bunch crossing, as a function of their transverse momentum and polar angle, for the Z (left) and $t\bar{t}$ (right) working points. The area limited by the red lines represents the acceptance of the vertex detector.

Parameter	Units	Z	WW	ZH	$t\bar{t}$
beam energy	GeV	45.6	80.0	120.0	182.5
horizontal emittance ϵ_x	nm rad	0.71	2.16	0.64	1.49
vertical emittance ϵ_y	pm rad	1.42	4.32	1.29	2.98
horizontal IP β_x	m	0.1	0.2	0.3	1
vertical IP β_y	mm	0.8	1	1	1.6
horizontal IP beam size σ_x^*	μm	8.46	20.78	13.86	38.60
vertical IP beam size σ_y^*	nm	33.7	65.7	35.9	69.0
bunch length σ_z (SR/BS)	mm	4.38/15.4	3.55/8.01	3.34/6.0	2.00/2.74
bunch population N_e	10^{11}	2.43	2.91	2.04	2.37
bunches/beam n_b		10000	880	248	40
IPC per Bunch Crossing		1300	1800	2700	3300
Bunch Spacing	ns	30	345	1225	7598

Table 15: Pairs produced per bunch crossing at the four FCC-ee beam energies for the V22 optics.

newer study using the V23 FCC-ee lattice (pre-mid-term report) and the IDEA vertex detector resulted in an occupancy of up to 20×10^{-6} in the first vertex detector layer, with the same safety factor and cluster size, and this equals a total hit rate of up to 170 MHz/cm^2 . Assuming a more realistic average cluster size of 1.5–2.5, a hit rate requirement of around 100 MHz/cm^2 for FCC-ee vertex detectors is derived.

In the IDEA drift chamber, where the pairs created by several successive bunch crossings need to be integrated during the cell drift time (400 ns), the hit occupancy is about 7% without any cut on the deposited energy (Simhit in GEANT). It is expected that this represents an upper limit, since the digitization electronics will eventually apply such cut and will be able to detect clusters of hits rather than single hits alone.

Incoherent pairs may also reach larger radii and their effects have been studied for the ALLEGRO liquid Argon electromagnetic calorimeter. The average energy deposition per cell due to a minimum ionizing particle (MIP) has been calculated for each layer using 20 GeV muons. The results are shown in Fig. 65. A fraction of these values can be used as a threshold for background suppression.

Preliminary occupancy estimates from IPC for the ALLEGRO ECal barrel and endcaps are shown in Fig. 66, averaged over 1000 bunch crossings. The blue line represents the occupancy without any cuts,

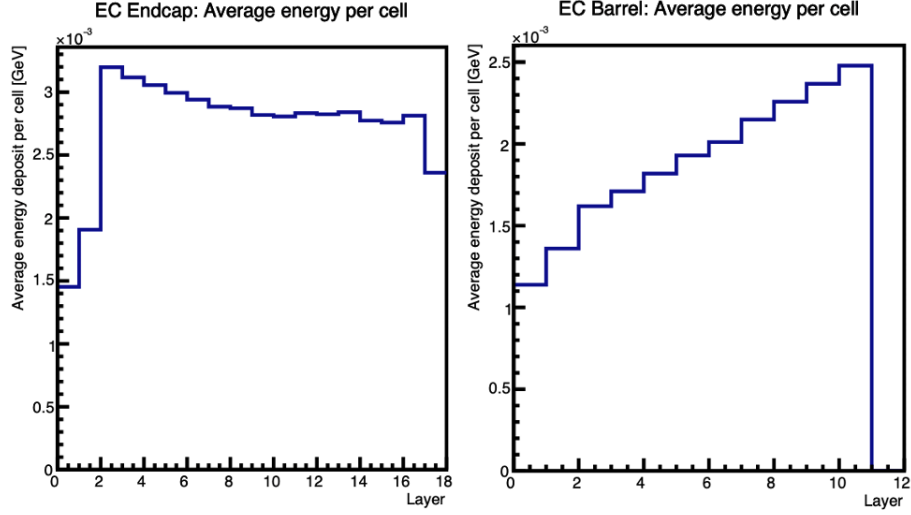


Fig. 65: Average energy deposition per cell per layer from a MIP (left: ECal endcaps; right: ECal barrel).

while the red and the green lines include a cut for energy deposition per cell lower than 20% and 30% respectively of the average MIP energy deposition shown in Fig. 65.

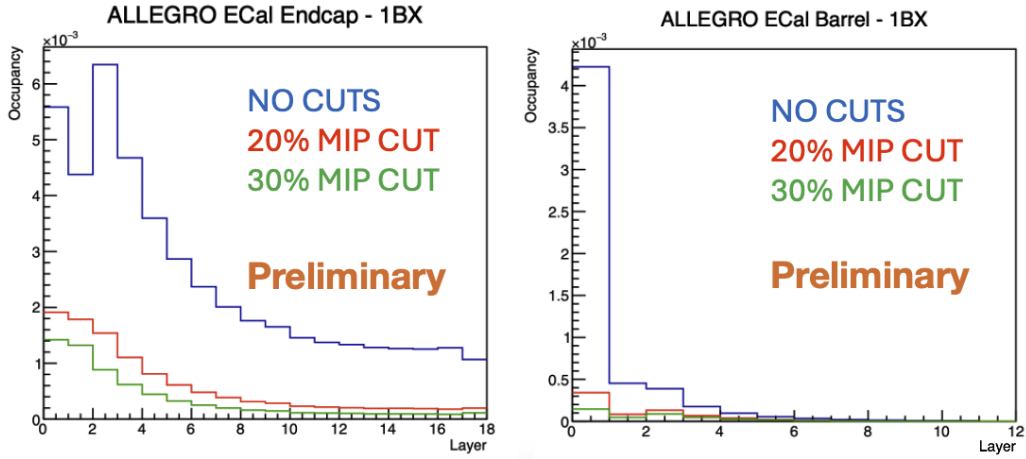


Fig. 66: Occupancy per bunch crossing for each layer of ECal endcaps (left) and barrel (right), using different cuts on the energy deposition per cell.

The effect of applying a cut is very effective in mitigating the occupancy, in particular in the innermost layers. Table 16 shows the average occupancy in the two subsystems. It is important to notice that these values do not account for pileup effects, and that at the Z-pole the bunches are separated of only about 20 ns.

	No Cuts	$E_{\text{dep}}^{\text{IPC}} > 20\% \langle E_{\text{dep}}^{\text{MIP}} \rangle$	$E_{\text{dep}}^{\text{IPC}} > 30\% \langle E_{\text{dep}}^{\text{MIP}} \rangle$
Endcaps	0.1% ~ 0.6%	0.02% ~ 0.2%	0.01% ~ 0.15%
Barrel	< 0.45%	< 0.03%	< 0.01%

Table 16: Average occupancy per bunch crossing, using different cuts on the energy deposition per cell.

7 Radiation levels and energy deposition

This section provides an overview of the ongoing studies on the energy deposition and the radiation levels in the interaction region and in the tunnel.

7.1 Final focus quadrupoles energy deposition

Ensuring proper operation of the final focus quadrupoles is a priority in a particle collider. Superconductive magnet quenches due to instantaneous power deposition and component deterioration from dose build-up must be avoided. Radiation showers triggered by the losses of radiative Bhabha electrons and positrons represent the main source exposing the final focus. In order to assess the impact of radiative Bhabha on QC1 and QC2, particles generated with BBBrem and GuineaPig++ have been injected into FLUKA to quantify power deposition and annual TID in the superconductive coils. A simplified geometry representative of the beamline from the central chamber to the final focus quadrupoles has been used. This includes a water-cooled stainless steel beam pipe (a 1.4-mm thick layer of water between two 0.8-mm thick layers of steel) and an outer layer of 0.2 mm of vacuum which separates it from the quadrupoles. The latter are made of four different layers, alternating 2-mm-thick aluminum and 4-mm-thick coil materials, for a total thickness of 1.2 cm. The equivalent material of the coils contains aluminum, NbTi alloy and copper, and it has a density of 5.09 g/cm³. This study has been performed for two operation modes, Z pole and $t\bar{t}$, considering the optics V24 and simulating only the particles generated with a cutoff in t of $1\sigma_y$ and a cutoff in energy of 50% (see subsection 6.7). The FLUKA model of the IR integrates a 3D magnetic field map including the fields of the detector, compensation and screening solenoids. This ensures that the off-momentum particles are properly transported in the geometry.

Table 17: Total power deposition in QC1 and QC2 due to radiative Bhabha electrons during stable collisions at Z pole, simulated with FLUKA for optics V24

Power at Z pole [mW]	QC1R1	QC1R2	QC1R3	QC2R1	QC2R2
Al layer 1	11	111	253	42	5
Coil layer 1	32	294	601	116	11
Al layer 2	6	53	105	23	2
Coil layer 2	15	135	263	64	5
Total	64	593	1222	245	23

Table 18: Total power deposition in QC1 and QC2 due to radiative Bhabha electrons during stable collisions at $t\bar{t}$, simulated with FLUKA for optics V24

Power at $t\bar{t}$ [mW]	QC1R1	QC1R2	QC1R3	QC2R1	QC2R2
Al layer 1	0.03	0.41	1.43	2.21	0.61
Coil layer 1	0.10	1.39	4.55	5.17	1.76
Al layer 2	0.02	0.26	0.84	0.91	0.35
Coil layer 2	0.06	0.74	2.34	2.29	0.95
Total	0.21	2.80	9.16	10.58	3.67

Tables 17 and 18 report the power absorbed by the different layers of each quadrupole segment during stable collisions. The magnet QC1 is more exposed than QC2, with a maximum power deposition of 1.2 W in QC1R3 at Z pole. The power deposition is much lower at $t\bar{t}$, since the luminosity is two orders of magnitude lower than at Z pole. Although these values are not concerning in themselves, the

asymmetric loss pattern on the FFQs given by the asymmetric beam-beam effects causes all the losses to be concentrated on one side of the beam pipe, i.e. the internal one. This concentration of losses determines high gradients in the distribution of energy deposition and, therefore, high local peak values of power density and TID. These peak values are shown in Fig. 67. The plot shows that the most critical case is found at Z pole for QC1, where the annual dose (computed assuming 10^7 s as the operational year) reaches up to 27 MGy/y and the power density peaks at around 14 mW/cm^3 . These values are regarded as too high, both from the point of view of quenching and radiation damage, indicating that an internal shielding layer must be integrated in the magnet design.

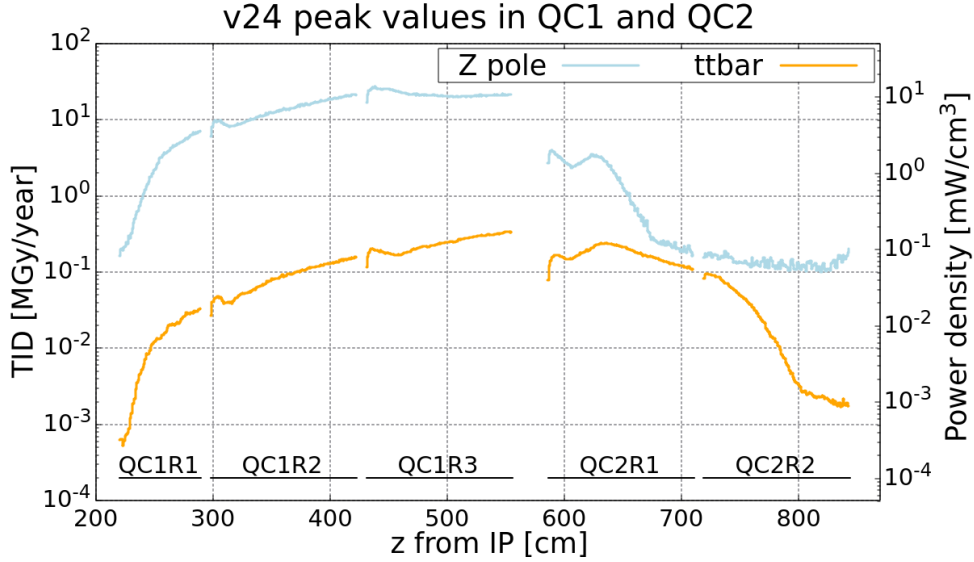


Fig. 67: Peak values of annual dose and power density deposition in QC1 and QC2 caused by radiative Bhabha electrons, simulated with FLUKA for optics V24.

Table 19: Total power deposition in QC1 layers due to radiative Bhabha electrons during stable collisions at Z pole with 2 mm tungsten shielding, simulated with FLUKA for optics V24

Power at Z pole [mW]	QC1R1	QC1R2	QC1R3
W shielding	84	587	1037
Al layer 1	4	27	48
Coil layer 1	11	74	131
Al layer 2	2	15	26
Coil layer 2	6	42	76
Total (magnet)	23	158	281

Having to add a shielding to suppress radiation showers from GeV-scale electrons inside the final focus magnets places a significant burden on the design, requiring an increase of the magnet aperture in an area with tight space constraints. In order to achieve the best shielding efficiency over short distances, the choice of a high-density material such as tungsten (W) appears natural. Fortunately, thanks to the small angles at which the electrons hit the vacuum chamber, the effective thickness of a shielding layer placed around the beam pipe as seen by the incoming radiation showers is much larger than its radial thickness (by more than a factor of 10). A study on the thickness of a conceptual shielding made of a W layer interposed between the vacuum chamber and the quadrupoles has been carried out with FLUKA for the most critical scenario (i.e., QC1 at Z pole). In the study, the radial thickness of the shielding has

been set to 0.2 cm. The power absorbed by the coils and the tungsten shieldings during stable collisions at Z pole with the extra shielding are listed in Table 19, to be compared with the corresponding numbers in Table 17. The results show that the power in the coils drops dramatically already with just 2 mm of W, decreasing by a factor of a few with respect to the case without shielding.

The results are even more promising when looking at the peak values of TID and power density in QC1 (Fig. 68). The 0.2 cm thick shielding reduces the peak values by nearly a factor of 10, bringing the maximum value of annual dose down to 3 MGy/y and the power density to around 1.6 mW/cm³. These values are compatible with the design limit adopted at the LHC, i.e., 30 MGy for the full lifetime of the magnet coils and 10–20 mW/cm³ for the quench threshold, even including some design margin. The exact amount of margin to be considered in these calculations may still be debated, but it appears appropriate to include it in the design to account for possible uncertainties or additional radiation sources, like beam-gas scattering or incoherent pair creation, that are not expected to be dominant, but still need to be accurately studied. A cylindrical W layer of around 2 mm in radius can be considered as a reasonable compromise between machine protection and space constraints.

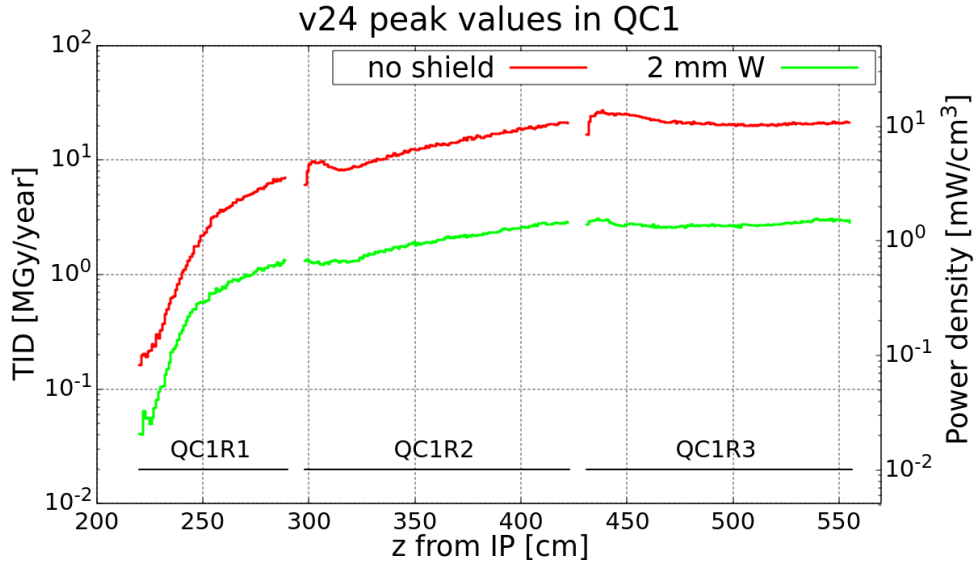


Fig. 68: Peak values of annual dose and power density deposition in QC1 caused by radiative Bhabha electrons with and without 2 mm tungsten shielding, simulated with FLUKA for optics V24.

7.2 Beamstrahlung dump

High intensity beamstrahlung (BS) radiation is expected to be generated at the interaction points as a result of the synchrotron radiation emitted during the collision in the electromagnetic field of the opposing beam. Dedicated devices are required to safely absorb the power carried by this beam, which can reach hundreds of kilowatts. One BS dump is required on each side of each interaction point; hence, a total of eight dumps are needed for the entire collider. One of the most efficient materials to absorb this type of radiation is lead. Moreover, in order to avoid thermal-stresses and unpredictable change of phase during operation, liquid lead, circulated in a close circuit has been chosen as the baseline (Fig. 69 and 70). Moreover, due to the strong dependence of the photon beam power to beam separation, a robust system capable of absorbing rapid power excursion is required. An ongoing research and development activity is active for the optimisation of this device, and a robust prototyping activity is envisaged in the pre-TDR phase. Collaboration between CERN and ENEA (Italy) is key in this development path. In addition, a robust shielding enclosure needs to be installed around the liquid lead system, so that activation of the cavern and limitations of personnel access to the area are avoided. An alternative design using gas-cooled

graphite discs is also being considered. Both design options are to be studied and prototyped in order to come up with a robust design for such device. Specifically, reduced-scale prototyping is planned to be carried out in 2027-2030, followed by a full scale prototype in year 2035, approximately.

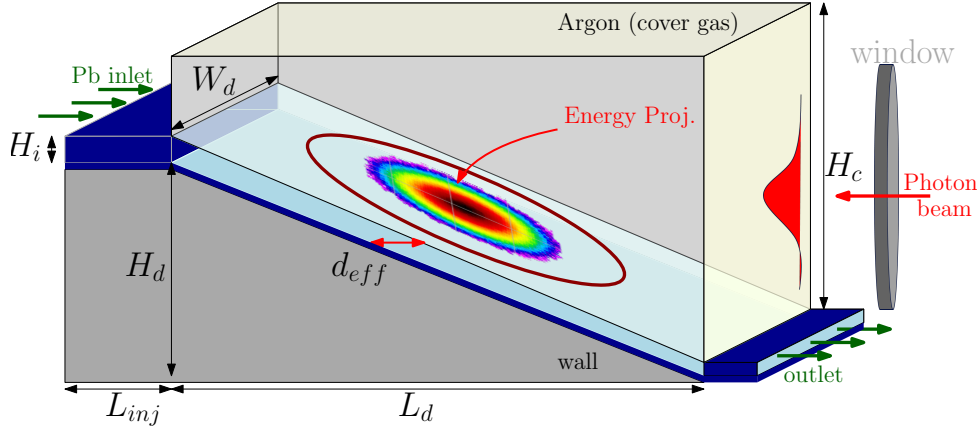


Fig. 69: Schematic of the FCC-ee Beamstrahlung dump.

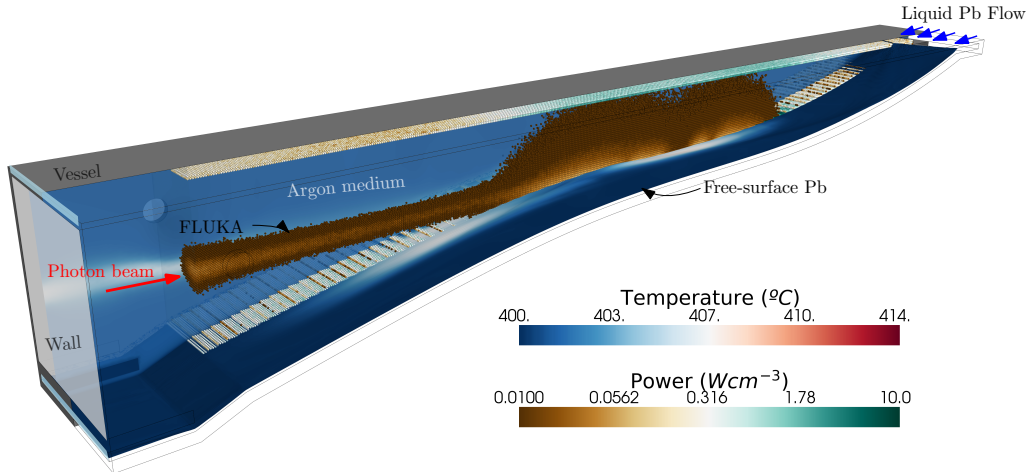


Fig. 70: Preliminary simulation of liquid-lead beamstrahlung dump.

7.3 Radiation levels within the tunnel

During the design phase, the study of environmental radiation levels in the tunnel is fundamental to estimate the radiation load to the distributed components, like cables or various electronics, and establish the need of shielding or radiation hardened components. The main radiation sources in the tunnel of FCC-ee experimental insertions are beamstrahlung radiation, radiative Bhabha and synchrotron radiation. Beamstrahlung photons contribute to tunnel radiation levels by generating radiation showers when interacting with the dedicated dump 500 m downstream of the IP. It is function of the dump shielding to contain these showers and limit the radiation leakage in its vicinity. A fraction of the off-momentum electrons produced in radiative Bhabha interactions at the IP are already lost in the magnetic elements within 150 m downstream. These losses generate radiation levels driven by luminosity around the experiment. The synchrotron radiation from the the outgoing beamline is the one significantly contributing to radiation levels in the experimental insertion, with more than 160 kW of SR power produced in the first

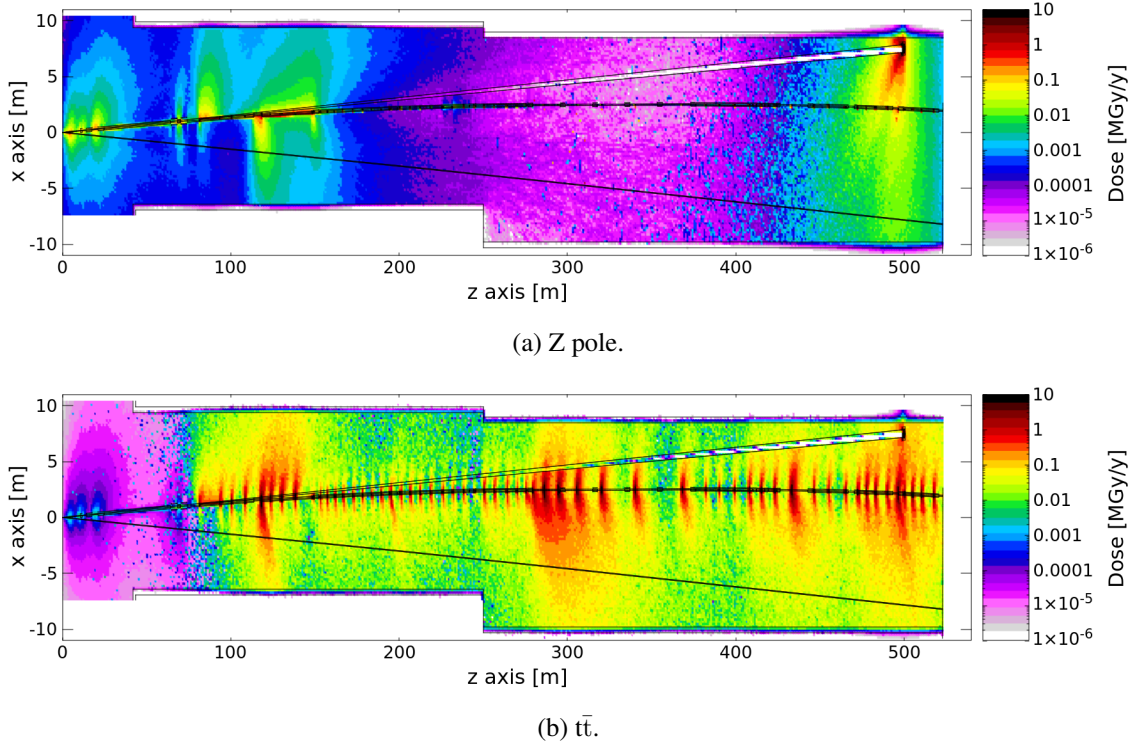


Fig. 71: Top view of annual TID at the beamline level (average for y in $[-20,20]$ cm) caused by beamstrahlung radiation, radiative Bhabha electrons and synchrotron radiation from the outgoing beam. Simulated with FLUKA for optics V22.

500 m downstream of the IP over the 1 kW produced by the incoming one. The tunnel radiation levels given by these three radiation sources have been simulated using FLUKA, for optics V22 and the two operation modes at Z pole and $t\bar{t}$ threshold.

A geometry representative of the right side of the IP has been modeled, including the concrete tunnel, the soil around, the outgoing beamline and the beamstrahlung extraction line with the dump. The model of the outgoing beamline consists of the copper beam pipe, with winglets hosting the synchrotron radiation absorbers in CuCrZr, and dipole and quadrupole magnets. The extraction line has been modeled as a conical copper chamber detaching from the beamline and a dummy model has been used for the beamstrahlung dump. This consists in a 20-cm-thick box in liquid lead ($\rho = 10.678 \text{ g/cm}^3$) surrounded by a two-layer shielding made of 5-cm thick iron and 20-cm thick concrete. A 2-cm-thick carbon fiber composite (CFC) window ($\rho=1.7 \text{ g/cm}^3$), which would preserve the vacuum, has been placed before it inside the extraction line. For what concerns the sources, beamstrahlung photons and radiative Bhabha electrons have been sampled from the distributions produced by the respective event generators mentioned in Section 6, while synchrotron radiation is generated run-time by FLUKA when transporting beam particles along the magnets.

The overall radiation levels in terms of annual TID from the IP ($z = 0$) up to ~ 520 m downstream are displayed in Fig. 71. These dose maps show that the radiation environments at the two operation modes are very different because dominated by different source terms. At Z pole, losses from radiative Bhabha dominate the dose levels up to 200 m downstream of the IP and radiation from the beamstrahlung dump dominates around 500 m. The vicinity of the beamstrahlung dump is the most exposed area at Z pole: the conceptual shielding tested in these preliminary simulations results in TID levels of several hundreds of kGy/y in the few metres around the dump and several tens of kGy/y on the closest beamline. Further optimization of the shielding will be performed, also based on radiation protection studies. Syn-

chrotron radiation does not completely affect the tunnel radiation levels: due to its soft spectrum, with critical energies ranging from 2.14 to 23.23 keV, 95% of its power is absorbed in the photon stoppers.

The picture looks the opposite at $\bar{t}\bar{t}$, where the environmental dose from synchrotron radiation is so dominant that it obscures the contributions from beamstrahlung and radiative Bhabha. Its harder spectra, given by the higher beam energy, features critical energies of the order of 1 MeV, leading to a reduction of the power fraction absorbed by the photon stoppers down to 67.8%. Dose hotspots of the order of 0.1–1 MGy/y are observed in correspondence of each SR absorber. In most cases, the iron yoke of the magnets partially shields these radiation showers, containing the hotspots in 1 m around the beamline. More spread hotspots are found where there is less material budget surrounding the absorbers, such as at drifts or at the magnets allowing the passage of the BS extraction line. This underlines that absorbers alone are not enough to suppress the radiation leakage in the tunnel, therefore additional shielding may be needed to mitigate the TID. Only in the close proximity of the IP the dose levels are determined by radiative Bhabha, but they are anyway 2 orders of magnitude lower than at Z pole because of the lower luminosity.

7.4 Radiation levels in the detector

The simulation of the radiation levels in the detector is fundamentally important for the design of the various subdetectors. The Monte Carlo code FLUKA has been used to estimate the TID and the 1-MeV-n-in-Si equivalent fluence in the IDEA detector from the main radiation sources at the Z pole operational mode, namely radiative Bhabha (RB) and incoherent pair creation (IPC). The results for other operational modes are currently not presented, but the radiation levels are expected to be lower due to the lower luminosities.

A representative geometry of the IDEA detector baseline has been modeled in FLUKA, including the vertex detector, the drift chamber, the solenoid, the dual-readout calorimeter, the μ Rwells and the iron yoke. The complex structure of the vertex detector has been simplified through equivalent layers made of equivalent materials condensing all of the main components. Similarly, the active Si pixels have been condensed into single Si layers. This simplification process has been done keeping the total mass and volume of the several parts unchanged. For what concerns the IR, the central chamber, the ellipto-conical chambers, the support and service cones, the support tube, the LumiCals and the final focus cryostats filled with liquid helium have been integrated as well. The magnetic fields from the detector, the compensation, and the screening solenoids are incorporated in the model through a 3D field map extending from -3 m to +3 m longitudinally and from -0.5 m to 0.5 m transversely.

The particle distributions resulting from RB and IPC are generated with BBBrem and GuineaPig++, as mentioned in the sections above. Electrons and positrons are then sampled from these distributions and transported in FLUKA to simulate the radiation showers, evaluating the annual dose and 1-MeV neutron equivalent fluences at the Z pole in the geometry described above. In order to save computing time, RB has been simulated only for one beam and the respective results have been mirrored with respect to the z axis to have an estimate for the other beam.

The 2D distribution of dose and fluence in the central part of the detector, covering the inner vertex and extending longitudinally up to the final focusing quadrupoles, is provided in Figs. 72 and 73. In the innermost layers of the vertex, an average TID of the level of tens of kGy/year and an average 1-MeV neutron equivalent fluence of up to a few 10^{12} cm⁻²/year are reached. Moreover, as shown in the figures, the IPC dominates the radiation levels in the vertex area and up to the LumiCal, while the RB losses become dominant in the forward direction at the position of the final focusing quadrupoles. The values of TID and 1-MeV neutron equivalent fluence have been computed for each layer of the vertex, as summarized in Figs 74 and 75. The results confirm that the inner vertex 1 layer is the most exposed to radiation, and that IPC dominates the radiation levels in the vertex, with a relatively larger share of dose and fluence from RB in the forward disks.

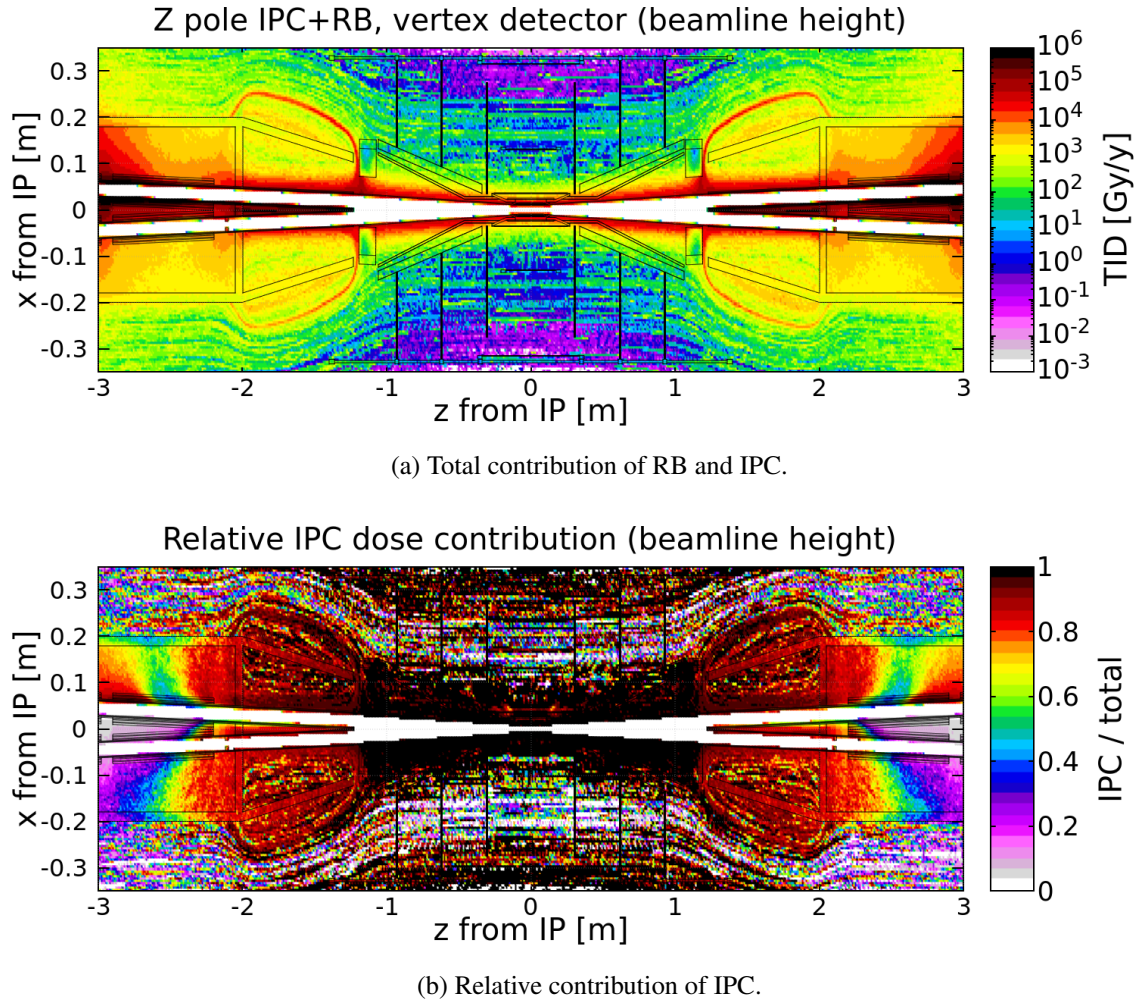
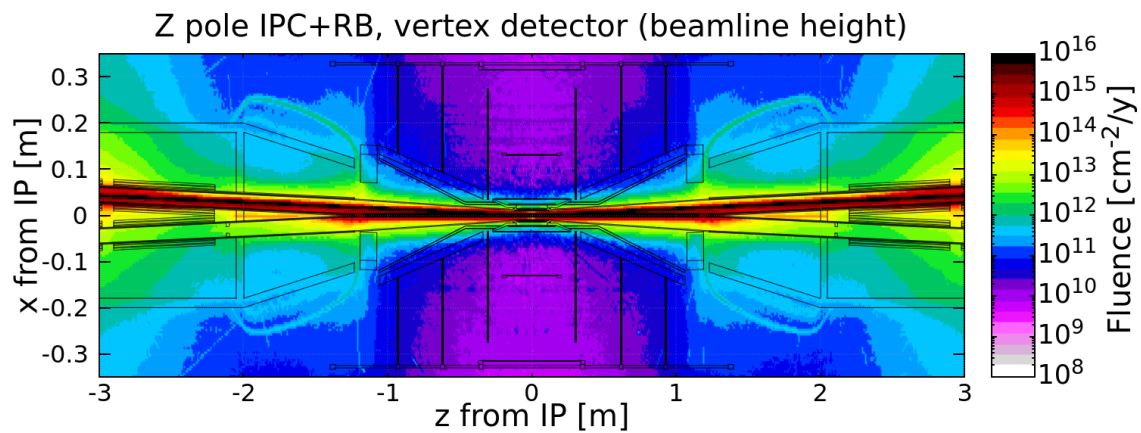


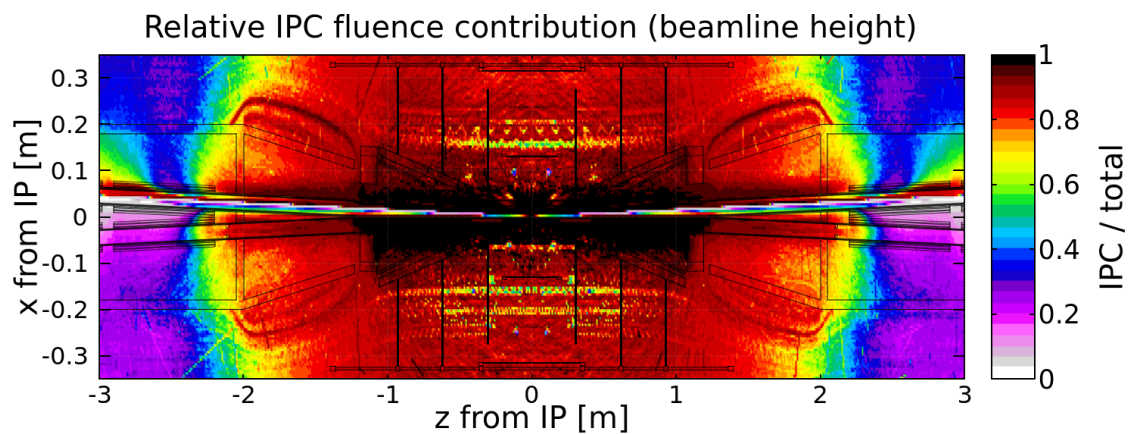
Fig. 72: TID levels at beamline height in IDEA IR from RB and IPC for 1 year of operation (10^7 s) at Z pole, simulated with FLUKA for optics v24.

Figures 76 and 77 show the transverse distribution of RB and IPC annual dose and 1-MeV neutron equivalent fluence in the LumiCal, along with their relative contribution, which confirms that IPC is the dominant source of radiation damage. Overall, the dose and fluence peaks in the LumiCal are comparable to the ones in the innermost vertex layers.

Similar studies have been performed for local beam-gas scattering at the Z-pole operational mode. A dedicated FLUKA simulation has been setup to sample bremsstrahlung interactions of the beam particles in the EM field of residual gas nuclei, starting from a gas pressure profile. The same realistic pressure profile used for beam-gas collimation studies (see Subsection 6.3) has been considered. The bremsstrahlung interaction is modeled by sampling the emission of a photon and then correcting the energy and the direction of the emitting particle, neglecting the recoil of the target nucleus. Most importantly, the interactions have been simulated in the limited s-range extending from -504.32 m to 5.58 m (where the origin is located at the IP). An analysis of the losses from these local beam-gas interactions showed that the scattered particles are partially collimated at the SR collimators and masks, and a significant fraction of them is lost within ± 6 m from the IP. These very preliminary results show that the most exposed subdetector is the first layer of the inner tracker, where peak values of ~ 3 kGy/year and $\sim 7 \times 10^{11} \text{ cm}^{-2}/\text{year}$ are found, therefore suggesting that it might not be a dominant contribution. However, there is evidence that the particles losses in the detector may also originate from outside the



(a) Total contribution of RB and IPC.



(b) Relative contribution of IPC.

Fig. 73: Fluence (1-MeV-n-in-Si equivalent) levels at beamline height in IDEA from RB and IPC for 1 year of operation (10^7 s) at Z pole, simulated with FLUKA for optics v24.

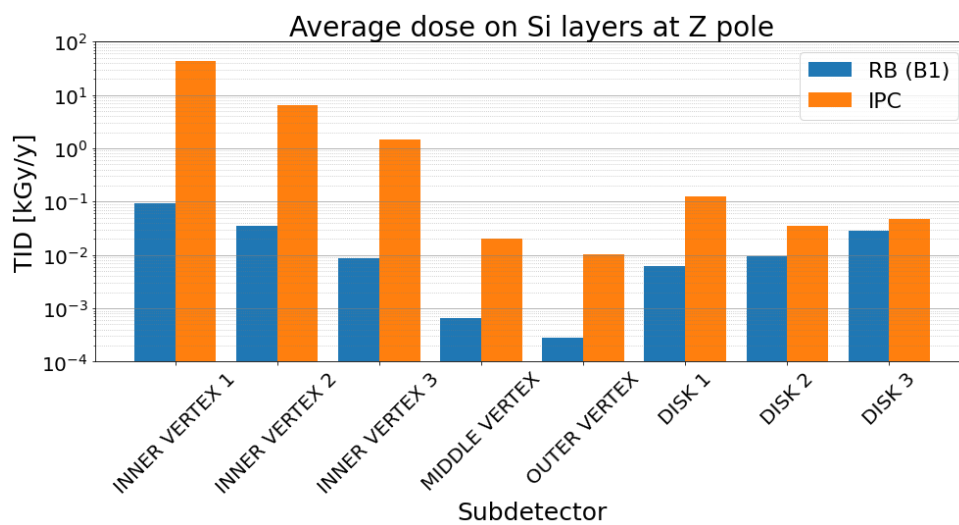


Fig. 74: Average TID values in vertex detector Si layers from RB and IPC for 1 year of operation (10^7 s) at Z pole, simulated with FLUKA for optics v24.

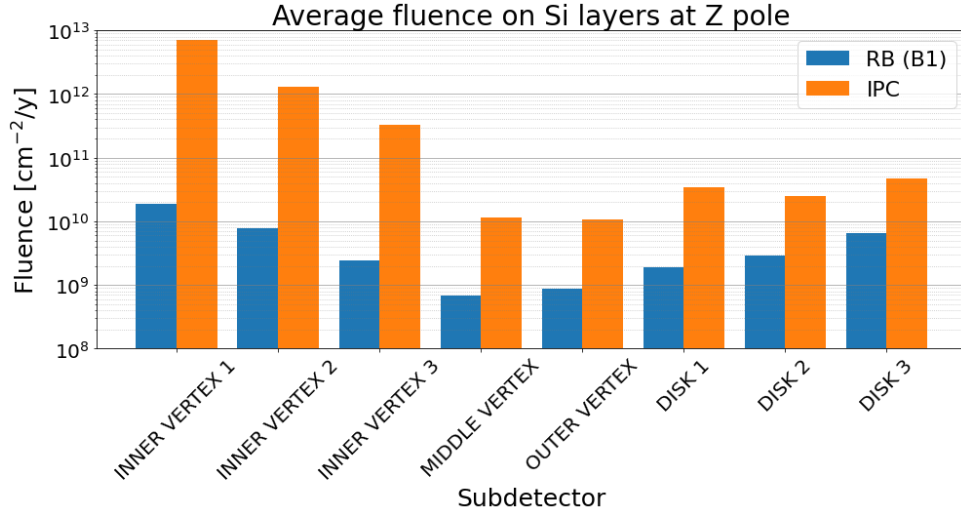


Fig. 75: Average fluence (1-MeV-n-in-Si equivalent) values in vertex detector Si layers from RB and IPC for 1 year of operation (10^7 s) at Z pole, simulated with FLUKA for optics v24.

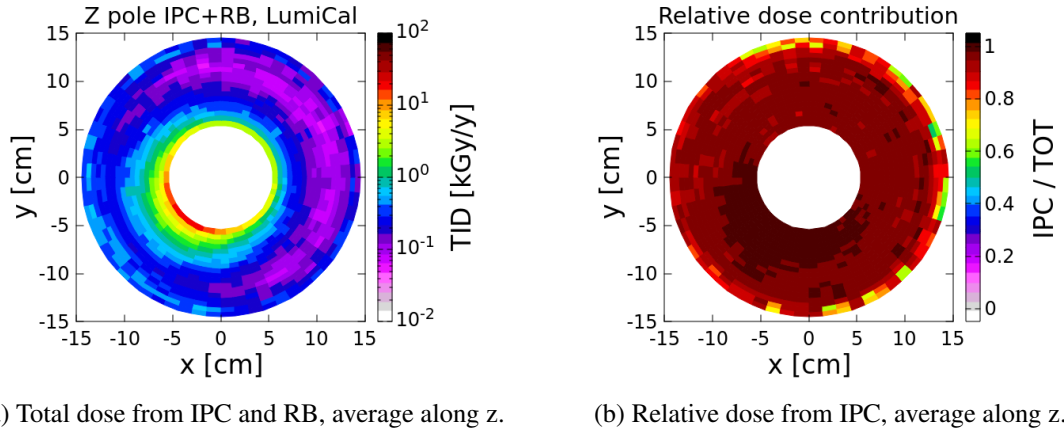
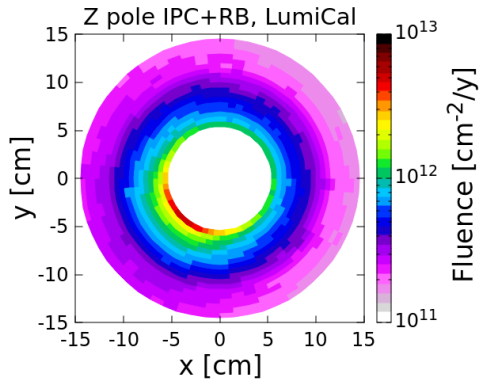
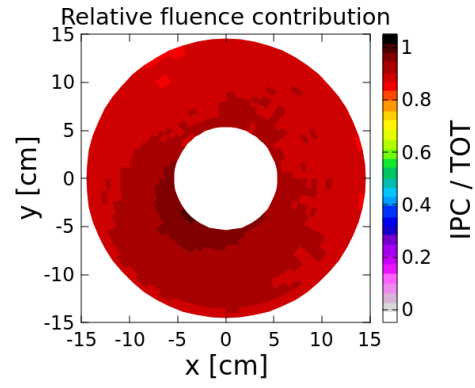


Fig. 76: Total and relative TID distribution on forward LumiCal from B1 RB and IPC for 1 year of operation (10^7 s) at Z pole, simulated with FLUKA for optics v24.

simulated s-range, building up from the arc of the collider (and not only from the IR). For this reason, the current results of detector radiation levels from beam-gas scattering may be underestimated, and must be regarded only as a very early and preliminary assessment.



(a) Total fluence from IPC and RB, average along z.



(b) Relative fluence from IPC, average along z.

Fig. 77: Total and relative fluence distributions on forward LumiCal from B1 RB and IPC for 1 year of operation (10^7 s) at Z pole, simulated with FLUKA for optics v24.

References

- [1] M. Boscolo, F. Palla, F. Bosi, F. Franesini, S. Lauciani, Mechanical model for the FCC-ee interaction region. *EPJ Tech. Instrum.* **10**, 16 (2023). <https://doi.org/10.1140/epjti/s40485-023-00103-7>
- [2] P. Raimondi, D.N. Shatilov, M. Zobov, Beam-Beam Issues for Colliding Schemes with Large Piwinski Angle and Crabbed Waist (2007). [arXiv:physics/0702033](https://arxiv.org/abs/physics/0702033)
- [3] FCC Feasibility Study Final Report; volume 2: Accelerators, technical infrastructure and safety (2025)
- [4] M. Boscolo, et al., Progress in the design of the future circular collider FCC-ee interaction region. *JACoW IPAC2024*, TUPC67 (2024). <https://doi.org/10.18429/JACoW-IPAC2024-TUPC67>
- [5] K. Oide, et al., Design of beam optics for the Future Circular Collider e^+e^- collider rings. *Phys. Rev. Accel. Beams* **19**, 111005 (2016). <https://doi.org/10.1103/PhysRevAccelBeams.19.111005>. [Addendum: *Phys.Rev.Accel.Beams* 20, 049901 (2017)]. [arXiv:1610.07170](https://arxiv.org/abs/1610.07170) [physics.acc-ph]
- [6] M. Boscolo, A. Ciarma, Characterization of the beamstrahlung radiation at the future high-energy circular collider. *Phys. Rev. Accel. Beams* **26**, 111002 (2023). <https://doi.org/10.1103/PhysRevAccelBeams.26.111002>. [arXiv:2307.15597](https://arxiv.org/abs/2307.15597) [hep-ex]
- [7] A. Frasca, et al., in *Proc. 15th International Particle Accelerator Conference (IPAC'24)* (JACoW Publishing, Geneva, Switzerland, 2024), no. 15 in IPAC'24 - 15th International Particle Accelerator Conference, pp. 1152–1155. <https://doi.org/10.18429/JACoW-IPAC2024-TUPC66>. URL <https://indico.jacow.org/event/63/contributions/3770>
- [8] K. Oide, M. Aiba, S. Aumon, M. Benedikt, A. Blondel, A. Bogomyagkov, M. Boscolo, H. Burkhardt, Y. Cai, A. Doblhammer, B. Haerer, B. Holzer, J.M. Jowett, I. Koop, M. Koratzinos, E. Levichev, L. Medina, K. Ohmi, Y. Papaphilippou, P. Piminov, D. Shatilov, S. Sinyatkin, M. Sullivan, J. Wenninger, U. Wienands, D. Zhou, F. Zimmermann, Design of beam optics for the future circular collider e^+e^- collider rings. *Phys. Rev. Accel. Beams* **19**, 111005 (2016). <https://doi.org/10.1103/PhysRevAccelBeams.19.111005>. URL <https://link.aps.org/doi/10.1103/PhysRevAccelBeams.19.111005>
- [9] Pantaleo Raimondi. Local chromatic correction, Arc and final focus. Presented at the FCC WEEK 2024 Workshop, San Francisco, USA (2024)
- [10] M. Koratzinos, K. Oide, in *12th International Particle Accelerator Conference* (2021). <https://doi.org/10.18429/JACoW-IPAC2021-THPAB012>
- [11] A. Ciarma, H. Burkhardt, M. Boscolo, P. Raimondi, Alternative solenoid compensation scheme for the FCC-ee interaction region. *JACoW IPAC2024*, TUPC68 (2024). <https://doi.org/10.18429/JACoW-IPAC2024-TUPC68>
- [12] A.T. et al., in *Proc. IPAC'24*
- [13] B. Parker, M. Anerella, J. Escallier, A. Ghosh, A. Jain, A. Marone, J. Muratore, P. Wanderer, BNL Direct Wind Superconducting Magnets. *IEEE Trans. Appl. Supercond.* **22**(3), 4101604 (2012). <https://doi.org/10.1109/TASC.2011.2175693>
- [14] N. Ohuchi, Y. Arimoto, K. Akai, K. Aoki, N. Higashi, K. Kanazawa, M. Kawai, T. Kawamoto, H. Koiso, Y. Kondou, M. Masuzawa, A. Morita, S. Nakamura, Y. Ohnishi, Y. Ohsawa, K. Oide, N. Okada, T. Oki, H. Sugimoto, M. Tawada, K. Tsuchiya, R. Ueki, X. Wang, H. Yamaoka, Z. Zong, B. Parker, M. Anerella, J. Escallier, A. Ghosh, H. Hocker, A. Jain, A. Marone, P. Wanderer, J. Di-Marco, J. Nogiec, M. Tartaglia, G. Velez, Superkekb beam final focus superconducting magnet system. *Nuclear Instruments and Methods in Physics Research Section A: Accelerators, Spectrometers, Detectors and Associated Equipment* **1021**, 165930 (2022). <https://doi.org/https://doi.org/10.1016/j.nima.2021.165930>. URL <https://www.sciencedirect.com/science/article/pii/S0168900221008949>

- [15] A. Novokhatski, E. Di Pasquale, F. Fransesini, J. Seeman, K. André, M. Boscolo, S. Lauciani, The design and electromagnetic analyses of the new elements in the FCC-ee IR vacuum chamber. *JACoW IPAC2024*, WEPR18 (2024). <https://doi.org/10.18429/JACoW-IPAC2024-WEPR18>
- [16] A. Novokhatski, M. Boscolo, F. Fransesini, S. Lauciani, L. Pellegrino, Estimated heat load and proposed cooling system in the FCC-ee interaction region. *JACoW IPAC2023*, MOPA092 (2023). <https://doi.org/10.1088/1742-6596/2687/2/022031>
- [17] A. Novokhatski, in *Proc. IPAC'23* (JACoW Publishing, Geneva, Switzerland, 2023), no. 14 in IPAC'23 - 14th International Particle Accelerator Conference, pp. 242–245. <https://doi.org/doi:10.18429/jacow-ipac2023-mopa092>. URL <https://indico.jacow.org/event/41/contributions/1316>
- [18] <https://www.ansys.com>
- [19] T. Brochard, P. Brumund, L. Goirand, J. Pasquaud, S. White, in *10th Mechanical Engineering Design of Synchrotron Radiation Equipment and Instrumentation* (2018), p. TUOPMA07. <https://doi.org/10.18429/JACoW-MEDSI2018-TUOPMA07>
- [20] F. Niccoli, C. Garion, C. Maletta, P. Chiggiato, Shape-memory alloy rings as tight couplers between ultrahigh-vacuum pipes: Design and experimental assessment. *Journal of Vacuum Science Technology A: Vacuum, Surfaces, and Films* **35** (2017). <https://doi.org/10.1116/1.4978044>
- [21] C.M.E.S.F.F.P.C. F. Niccoli, C. Garion, Beam-pipe coupling in particle accelerators by shape memory alloy rings. *Materials Design* **114**, 603–611 (2017). URL <https://doi.org/10.1016/j.matdes.2016.11.101>
- [22] Kyo Shibata. Vacuum system of SuperKEKB interaction region, Presented at the LCWS24 (2024)
- [23] M. Mager, Upgrade of the ALICE ITS in LS3. *PoS Vertex2019*, 040 (2019). <https://doi.org/10.22323/1.373.0040>
- [24] L. Pancheri, J. Olave, S. Panati, A. Rivetti, F. Cossio, M. Rolo, N. Demaria, P. Giubilato, D. Pantano, S. Mattiazzo, A 110 nm CMOS process for fully-depleted pixel sensors. *JINST* **14**, C06016 (2019). <https://doi.org/10.1088/1748-0221/14/06/C06016>
- [25] R. Zanzottera, et al., ATLASPIX3 Modules for Experiments at Electron-Positron Colliders. *PoS Pixel2022*, 086 (2023). <https://doi.org/10.22323/1.420.0086>
- [26] Alexander Novokhatski. Consideration on the gold coating in the IR vacuum chamber. https://indico.cern.ch/event/1430670/contributions/6026323/attachments/2892514/5070722/Novokhatski_MDI_IR_7_08_2024.pdf (2024)
- [27] L. Watrelot, FCC-ee Machine Detector Interface Alignment System Concepts. Concepts de systemes pour l'alignement de la MDI du FCC-ee. Ph.D. thesis, École doctorale Sciences des métiers de l'ingénieur (Paris) (2023). URL <https://cds.cern.ch/record/2894663>. Presented 19 Sep 2023
- [28] L. Watrelot, M. Sosin, S. Durand, Frequency scanning interferometry based deformation monitoring system for the alignment of the FCC-ee machine detector interface. *Measurement Science and Technology* **34**, 075006 (2023). <https://doi.org/10.1088/1361-6501/acc6e3>
- [29] H. Mainaud Durand, T. Dijoud, M. Duquenne, J.C. Gayde, F. Micolon, V. Rude, M. Sosin, Frequency Scanning Interferometry as New Solution for on-Line Monitoring Inside a Cryostat for the HL-LHC project p. WEPAF068 (2018). <https://doi.org/10.18429/JACoW-IPAC2018-WEPAF068>. URL <https://cds.cern.ch/record/2667534>
- [30] Y. Arimoto, J. DiMarco, K. Egawa, T. Kawamoto, M. Masuzawa, J. Nogiec, Y. Ohsawa, N. Ohuchi, R. Ueki, G. Velez, et al., Magnetic measurement with single stretched wire method on superkekb final focus quadrupoles. Tech. rep., Fermi National Accelerator Lab.(FNAL), Batavia, IL (United States) (2019)
- [31] G. Ganis, C. Helsens, V. Völkl, Key4hep, a framework for future HEP experiments and its use in FCC. *Eur. Phys. J. Plus* **137**(1), 149 (2022). <https://doi.org/10.1140/epjp/s13360-021->

- 02213-1. [arXiv:2111.09874](https://arxiv.org/abs/2111.09874) [hep-ex]
- [32] M. Frank, F. Gaede, C. Grefe, P. Mato, DD4hep: A Detector Description Toolkit for High Energy Physics Experiments. *J. Phys. Conf. Ser.* **513**, 022010 (2014). <https://doi.org/10.1088/1742-6596/513/2/022010>
 - [33] J. Allison, et al., Recent developments in geant4. *Nucl. Instrum. Methods. Phys. Res. B* **835**, 186–225 (2016). <https://doi.org/10.1016/j.nima.2016.06.125>
 - [34] F. Gaede, et al., EDM4hep - a common event data model for HEP experiments. *PoS ICHEP2022*, 1237 (2022). <https://doi.org/10.22323/1.414.1237>
 - [35] URL <http://mad.web.cern.ch/mad>. [Http://mad.web.cern.ch/mad](http://mad.web.cern.ch/mad)
 - [36] N. Alipour Tehrani, Simulation and tracking studies for a drift chamber at the FCC-ee experiment. Tech. rep., CERN, Geneva (2019). URL <https://cds.cern.ch/record/2670936>
 - [37] W. Elmetenawee, gianluigi chiarello, A. Corvaglia, F. Cuna, N.D. Filippis, E. Gorini, F. Grancagnolo, M. Maggi, A. Miccoli, M. Panareo, M. Primavera, G.F. Tassielli, A. Ventura. The tracking performance for the idea drift chamber (2022). URL <https://arxiv.org/abs/2211.12568>
 - [38] J.A. *et al.*, Recent developments in geant4. *Nuclear Instruments and Methods in Physics Research Section A: Accelerators, Spectrometers, Detectors and Associated Equipment* **835**, 186–225 (2016). <https://doi.org/https://doi.org/10.1016/j.nima.2016.06.125>. URL <https://www.sciencedirect.com/science/article/pii/S0168900216306957>
 - [39] M. Boscolo, H. Burkhardt, M. Sullivan, Machine detector interface studies: Layout and synchrotron radiation estimate in the future circular collider interaction region. *Physical Review Accelerators and Beams* **20** (2017). <https://doi.org/10.1103/PhysRevAccelBeams.20.011008>
 - [40] CERN. Fluka website. <https://fluka.cern>
 - [41] G. Battistoni, et al., Overview of the FLUKA code. *Ann. Nucl. Energy* **82**, 10 (2015). <https://doi.org/10.1016/j.anucene.2014.11.007>. URL <http://cds.cern.ch/record/2162467>
 - [42] C. Ahdida, et al., New Capabilities of the FLUKA Multi-Purpose Code. *Frontiers in Physics* **9** (2022). <https://doi.org/10.3389/fphy.2021.788253>
 - [43] M. Hofer, et al., in *Proc. IPAC’22* (Bangkok, Thailand, 2022), pp. 1722–1725. <https://doi.org/10.18429/JACoW-IPAC2022-WEPOST017>
 - [44] G. Broggi, First study of collimator design for the fcc-ee. Master’s thesis, Politecnico di Milano (2022)
 - [45] A. Abramov, et al., in *Proc. IPAC’23* (Venice, Italy, 2023), pp. 356–359. <https://doi.org/10.18429/JACoW-IPAC2023-MOPA128>
 - [46] G. Broggi, A. Abramov, R. Bruce, in *Proc. IPAC’23* (Venice, Italy, 2023), pp. 360–363. <https://doi.org/10.18429/JACoW-IPAC2023-MOPA129>
 - [47] G. Broggi, Tracking studies for the fcc-ee collimation system design. *Nuovo Cimento C* **47** (2024)
 - [48] G. Broggi, et al., in *Proc. IPAC’24* (Nashville, Tennessee, USA, 2024), pp. 1192–1195. <https://doi.org/10.18429/JACoW-IPAC2024-TUPC76>
 - [49] G. Broggi, Fcc-ee collimation. Presented at FCC Week 2024, San Francisco, California, USA, June 2024
 - [50] A. Abramov, et al., Collimation simulations for the fcc-ee. *JINST* **19**, T02004 (2024). <https://doi.org/10.1088/1748-0221/19/02/T02004>
 - [51] A. Abramov, et al., in *Proc. IPAC’22* (Bangkok, Thailand, 2022), pp. 1718–1721. <https://doi.org/10.18429/JACoW-IPAC2022-WEPOST016>
 - [52] F.V. der Veken, et al., in *Proc. HB’23* (Geneva, Switzerland, 2023), pp. 474–478. <https://doi.org/10.18429/JACoW-HB2023-THBP13>
 - [53] F.V. der Veken, Introducing xcoll: A streamlined approach to collimation and beam loss simulations

using xsuite. Presented at ICAP'24, Berlin, Germany, October 2024

- [54] G. Iadarola, et al., in *Proc. HB'23* (Geneva, Switzerland, 2023). <https://doi.org/10.18429/JACoW-HB2023-TUA2I1>
- [55] L. Nevay, et al., Bdsim: An accelerator tracking code with particle-matter interactions. *Comput. Phys. Commun.* **252**, 107200 (2020). <https://doi.org/10.1016/j.cpc.2020.107200>
- [56] L. Nevay, et al., in *Proc. ICFA Mini-Workshop on Tracking for Collimation* (CERN, Geneva, Switzerland, 2018), p. 45. <https://doi.org/10.23732/CYRCP-2018-002.45>
- [57] S. Agostinelli, et al., Geant4—a simulation toolkit. *Nucl. Instrum. Methods. Phys. Res. A* **506**, 250–303 (2003). [https://doi.org/10.1016/S0168-9002\(03\)01368-8](https://doi.org/10.1016/S0168-9002(03)01368-8)
- [58] J. Allison, et al., Geant4 developments and applications. *IEEE Trans. Nucl. Sci.* **53**, 270–278 (2006). <https://doi.org/10.1109/TNS.2006.869826>
- [59] R. Bruce, R.W. Assmann, V. Boccone, C. Bracco, M. Brugger, M. Cauchi, F. Cerutti, D. Deboy, A. Ferrari, L. Lari, A. Marsili, A. Mereghetti, D. Mirarchi, E. Quaranta, S. Redaelli, G. Robert-Demolaize, A. Rossi, B. Salvachua, E. Skordis, C. Tambasco, G. Valentino, T. Weiler, V. Vlachoudis, D. Wollmann, Simulations and measurements of beam loss patterns at the cern large hadron collider. *Phys. Rev. ST Accel. Beams* **17**, 081004 (2014). <https://doi.org/10.1103/PhysRevSTAB.17.081004>. URL <https://link.aps.org/doi/10.1103/PhysRevSTAB.17.081004>
- [60] G. Broggi, Beam-gas beam losses and mdi collimators. Presented at FCC Week 2024, San Francisco, CA, USA, June 2024
- [61] V.I. Telnov, Scattering of electrons on thermal radiation photons in electron - positron storage rings **A260**, 304 (1987). [https://doi.org/10.1016/0168-9002\(87\)90093-3](https://doi.org/10.1016/0168-9002(87)90093-3)
- [62] H. Burkhardt. Monte Carlo Simulation of Beam Particles and Thermal Photons (1993). *SL Note 93-73 (OP)*
- [63] Kevin André. Synchrotron radiation background due to off-axis, on-energy top up injection at 45.6 GeV. <https://indico.cern.ch/event/1237189/contributions/5218074/attachments/2578785/4447272/FCC-ee%20Optics%20Meeting%2023161.pdf> (2023)
- [64] R. Kleiss, H. Burkhardt, BBBREM: Monte Carlo simulation of radiative Bhabha scattering in the very forward direction. *Comput. Phys. Commun.* **81**, 372 (1994). [https://doi.org/10.1016/0010-4655\(94\)90085-X](https://doi.org/10.1016/0010-4655(94)90085-X). [arXiv:hep-ph/9401333](https://arxiv.org/abs/hep-ph/9401333)
- [65] D. Schulte, Beam-beam simulations with Guinea-Pig. *eConf C980914*, 127 (1998). URL <https://cds.cern.ch/record/382453>
- [66] C. Rimbault, P. Bambade, K. Mönig, D. Schulte, Incoherent pair generation in a beam-beam interaction simulation. *Phys. Rev. ST Accel. Beams* **9**, 034402 (2006). <https://doi.org/10.1103/PhysRevSTAB.9.034402>. URL <https://link.aps.org/doi/10.1103/PhysRevSTAB.9.034402>
- [67] A. Ciarma, M. Boscolo, G. Ganis, E. Perez, in *Proc. 65th ICFA Adv. Beam Dyn. Workshop High Luminosity Circular e+e- Colliders (eeFACT'22)* (JACoW Publishing, Geneva, Switzerland, 2022), no. 65 in ICFA Advanced Beam Dynamics Workshop on High Luminosity Circular e+e- Colliders, pp. 85–90. <https://doi.org/10.18429/JACoW-eeFACT2022-TUZAT0203>. URL <https://jacow.org/eeFact2022/papers/tuzat0203.pdf>